Karlsruhe Institute of Technology

Search for keV-Scale Sterile Neutrinos with KATRIN

Masterarbeit

vorgelegt am 13. Juli 2015 von

Anton Huber

An der Fakultät für Physik
Institut für Experimentelle Kernphysik

Erstgutachter:	Prof. Dr. Guido Drexlin Institut für Experimentelle Kernphysik, KIT
Zweitgutachter:	Prof. Dr. Ulrich Husemann Institut für Experimentelle Kernphysik, KIT
Betreuende Mitarbeiterin:	Dr. Susanne Mertens Institute for Nuclear and Particle Astrophysics, LBNL

Erklärung

Ich versichere hiermit wahrheitsgemäß, die Arbeit selbstständig verfasst und keine anderen als die angegebenen Quellen und Hilfsmittel benutzt, die wörtlich oder inhaltlich übernommenen Stellen als solche kenntlich gemacht und die Satzung des Karlsruher Instituts für Technologie (KIT) zur Sicherung guter wissenschaftlicher Praxis in der jeweils gültigen Fassung beachtet zu haben.

Anton Huber
Karlsruhe, den 13. Juli 2015

Zusammenfassung

Das KArlsruher TRItium Neutrino Experiment (KATRIN) das sich am Karlsruher Institut für Technologie (KIT) im Aufbau befindet, nutzt das β-Zerfallsspektrum von molekularem Tritium, um die effektive Masse des Elektron-Antineutrinos mit einer Sensitivität von 200 meV (90% C.L.) zu bestimmen. Dazu wird das Tritium β-Zerfallsspektrum nahe des Endpunktes mit hoher Präzision vermessen. Um die notwendige statistische Sensitivität zu erreichen, ist eine Tritiumquelle mit einer hohen Aktivität von $\lambda_\mathrm{d} \approx 10^{11}$ Zerfällen pro Sekunde notwendig.
Diese besonderen Quelleigenschaften können genutzt werden, um das KATIRN Experiment zu erweitern. Nach einer erfolgreichen Beendigung der Neutrinomassenbestimmung, kann mit KATRIN nach sterilen Neutrinos im keV-Massenbereich gesucht werden, welche geeignete Kandidaten für Dunkle Materie sind. Diese Arbeit beschäftigt sich mit der experimentelle Realisierbarkeit dieser Suche mit dem KATRIN Experiment.
Dazu wird eine Studie vorgestellt, die das Potential eines Tritium β-Zerfallsexperiment, vergleichbar dem KATRIN Experiment, für die Suche nach sterilen Neutrinos im keV-Massenbereich aufzeigt. Innerhalb der Studie wird klar, dass theoretische und experimentelle Unsicherheiten einen großen Einfluss auf die erreichbare Sensitivität haben.
Der Fokus dieser Arbeit liegt deshalb auf der Untersuchung einer solchen experimentellen Unsicherheit. Im Gegensatz zum normalen KATRIN Messbetrieb, muss bei der Suche nach sterilen Neutrinos im keV-Massenbereich, dass gesamte Tritium β-Zerfallsspektrum vermessen werden. Dazu wird das Verzögerungspotential des Hauptspektrometers auf null gesetzt. Folglich haben die Elektronen die von der Quelle zum Detektor transportiert werden, hohe Überschussenergien. Dies führt wiederum zu nicht-adiabatischen Transportbedingungen, welche die Transmissionseigenschaft des KATRIN Hauptspektrometers stark beeinträchtigen. Im Rahmen dieser Arbeit wird gezeigt, dass eine Erhöhung des Magnetfeldes in der Analysierebene des KATRIN Hauptspektrometers um einen Faktor 4 notwendig ist, um für Elektronen bis zu 20 keV Überschussenergie, einen vollständig adiabatischen Transport zu gewährleisten.
Eine weitere Herausforderung die aufkommt, wenn KATRIN genutzt wird um nach sterilen Neutrinos zu suchen, ist die hohe Signalrate am Detektor. Da KATRIN im normalen Messbetrieb das Spektrum in einem Bereich von wenigen eV unter dem Endpunkt ver-

misst, sind niedrige Elektronenraten von < 1 Hz zu erwarten. Wird jedoch das gesamte Spektrum vermessen, erhöht sich die Rate um 12 Größenordnung. Um dieses zu messen, ist ein neuartiger Detektor notwendig. Ein Prototyp dieses Detektors befindet sich derzeit in der Herstellung. Um diesen zu Untersuchen wird eine gut kalibrierte Elektronenquelle benötigt. Einer weiterer Fokus der Arbeit war daher die Inbetriebnahme einer neuen Elektronenkanone, die mit Hilfe eines Faraday Cup Detektors charakterisiert wurde.

Zusammenfassend wird in dieser Arbeit gezeigt, dass es möglich ist mit KATRIN einen großen Fortschritt auf der Suche nach sterilen Neutrinos im keV-Massenbereich zu machen und damit einen Beitrag zur Suche nach dunkler Materie zu leisten. Darüber hinaus legt sie einen Grundstein für viele weitere Arbeiten und Studien die sich mit der Erweiterung des KATRIN Experiments zur Suche nach sterilen Neutrinos im keV-Massenbereich befassen.

Introduction and Objectives

Experiments measuring solar and atmospheric as well as accelerator and reactor neutrinos have provided compelling evidence that neutrinos oscillate between different flavor eigenstates, which proves that neutrinos are not massless [SNO02], [Kam96], [Kam03]. The absolute mass scale however, is still unknown.
Cosmological observations limit the mass to $m_\nu < 0.23$ eV[1] [Pla14], while laboratory experiments provide a model-independent upper limit of $m_\nu < 2$ eV [Bon01]. The KATRIN experiment is a next-generation, large-scale β-decay experiment with the key goal to determine the effective neutrino mass with a sensitivity of 200 meV (90% C.L.). This is achieved by analyzing the shape of the tritium β-decay close to the endpoint, where the influence of the neutrino mass is maximal. To reach sufficient statistic in the region-of-interest after 3 years of measurement time, KATRIN will operate a source with unprecedented high luminosity of $\lambda_\mathrm{d} \approx 10^{11}$ decays per second.
This unprecedented source luminosity allows KATRIN to extend its physics reach to search for keV-scale sterile neutrinos. This work focuses on keV-scale sterile neutrinos, which would be an attractive candidate for dark matter.
Beside the three light active neutrinos, phenomenological works suggest the existence of additional neutrino mass eigenstates [Aba12]. These new mass eigenstates would predominantly be sterile, but could have a small admixture of active neutrinos. Very heavy sterile neutrinos are commonly postulated in a see-saw scenario to explain the tiny masses of the active neutrinos [Sch80]. Very light sterile neutrinos in the eV mass range are motivated by anomalies in reactor and short baseline experiments [Aba12]. Sterile neutrinos in the keV mass range are motivated as dark matter candidates [San11].
A suite of astrophysical and cosmological observations has revealed, that only 4.9% of the total energy of the universe is related to baryonic matter [Pla14]. The remaining contributions stem from dark energy (68.3%) and dark matter (26.8%). The Standard Model (SM), does not provide a suitable candidate, and therefore extensions to the SM are inevitable. Sterile neutrinos in the keV mass range, could account for a significant fraction of the dark matter in the universe.

[1]The correct unit for mass is eV/c^2. In this thesis however, $\bar{h}$ and c is set to unit.

In contrast to the normal KATRIN mode, which scans only a tiny fraction of the phase space, the entire tritium β-decay spectrum has to be recorded to search for keV-scale sterile neutrinos. To do so, the KATRIN main spectrometer has to be operated at zero or very low retarding potential. Electrons with energies well above the retarding potential (i.e. with high surplus energies) will lead to a systematic uncertainty due to their non-adiabatic transport through the main spectrometer. This work focuses on this experimental systematic uncertainty and proposes a solution based on the large volume air coil system.
Due to the high rates that have to be handled when KATRIN is operated at a very low retarding potential, a new detector system has to be build. To eliminate, or at least reduce systematic effects due to the new detector and read-out system, a well-calibrated electron source is of crucial importance. Another goal of this thesis was the commissioning and characterization of a new electron gun, and shows initial measurements with this device, based on a Faraday cup detector system.

This work is structured as follows: The first chapter gives an introduction to the history of neutrino and astroparticle physics, with the focus on dark matter and sterile neutrinos. Chapter 2 explains the 'normal' KATRIN measurement principle to determine the neutrino mass, and details an extended mode-of-operation, that would allow to search for sterile neutrinos in the keV mass range. In chapter 3, a corresponding study is presented, which calculates the statistical sensitivity that could be reached after a three year measurement using a KATRIN-like experiment. Furthermore, the influence of theoretical and experimental uncertainties on the sensitivity are discussed. Chapter 4 focuses on the adiabatic transport of high surplus energy electrons through the main spectrometer, when operated in the sterile neutrino search mode. Results of the high intensity e-gun characterization can be found in chapter 5.

This thesis is the first step toward a realization of an extension of the KATRIN spectrometer and detector section, that would allow to search for keV-scale sterile neutrinos, which discovery would be a major breakthrough in particle and astroparticle physics. The search for sterile neutrinos with a model-independent laboratory experiment would be a significant extension of the world-wide effort in this field. KATRIN is in the unique position to provide statistical sensitivity in the cosmological allowed parameter space. The implementation of this proposal is to make an impact on the field of dark matter physics and help to better understand one of the biggest mysteries of the universe.

Contents

1. Neutrino and Astroparticle Physics

While our understanding of the neutrino has changed essentially over the past decades, some of its fundamental properties such as its intrinsic nature and its mass are still unknown. Moreover, it remains an open question whether or not a right-handed partner of the known left-handed neutrino exists.

These properties are important keys to unraveling the most compelling mysteries of the universe: The determination of the neutrino mass would crucially impact our understanding of the origin of particle masses and the role of primordial neutrinos in the evolution of large scale structures in the universe. The discovery of right-handed neutrinos in the kilo electron-volt (keV) mass range could unlock the secret of the intrinsic nature of dark matter.

This chapter will give an introduction to the field of neutrino physics. The basic neutrino properties and the major experiments in the history of neutrino physics will be explained chronologically, and open questions will be pointed out. Secondly, the role of the sterile neutrino in the field of astroparticle and dark matter physics will be discussed.

1.1. History of Neutrino Physics

The history of neutrino physics started in 1903 when E. Rutherford and F. Soddy set up a theory about the decay of heavy nuclei. They proposed three different types of radioactive decays. While α- and γ-decays show a discrete spectrum, J. Chadwick measured in 1914 a continuous energy spectrum of the electrons emitted in β-decays [Cha14].

1914 - The β-Decay Problem

The final state of the β-decay was assumed to be a two body state, existing of the daughter nucleus and an electron. Simple kinematic calculations led to the assumption, that the emitted electron must be monoenergetic, yet a continuous spectrum was found. Another inconsistency that came with the β-decay, was the spin statistic problem. If the β-decay is defined as a two body decay

$$\beta^- - \text{decay:} \qquad \mathrm{n} \rightarrow \mathrm{p} + \mathrm{e}^- \tag{1.1}$$

$$\beta^+ - \text{decay:} \qquad \mathrm{p} \rightarrow \mathrm{n} + \mathrm{e}^+ \tag{1.2}$$

the spin of the initial state is always half-integer and on the final state either +1 or 0. Hence, the two body decay violates the spin conservation.

As a consequence of the two problems, W. Pauli proposed in his famous letter ("Meine Radioaktiven Damen und Herren") [Pau30] to H. Geiger, L. Meitner and other members of the nuclear physics community, a new particle - the neutrino[1].

1930 - Pauli's Idea

To solve the spin statistic problem, W. Pauli proposed a new spin $\frac{1}{2}$ particle [Pau30]. To explain the shape of the β-spectrum, it has to be massless, or at least with a very small mass.

The β-decay now became a three body decay

$$\beta^- - \text{decay:} \qquad \mathrm{n} \rightarrow \mathrm{p} + \mathrm{e}^- + \overline{\nu}_e \tag{1.3}$$

$$\beta^+ - \text{decay:} \qquad \mathrm{p} \rightarrow \mathrm{n} + \mathrm{e}^+ + \nu_e. \tag{1.4}$$

Since the decay is a quantum mechanical process, the released energy is statistically shared by the electron and the neutrino, which leads to a continuous electron energy spectrum.

1934 - Fermi's Formalism

E. Fermi was the first who formulated a theory to describe β-decays [Fer34]. He approximated the decay as an one-vertex decay, where all the four fermions directly interact at one specific point. The strength of the coupling is described by the Fermi constant G_F. The calculation of the β-spectrum is given by "Fermi's Golden Rule"

$$\Gamma = 2\pi \cdot G_F^2 \cdot |\langle f|M_{fi}|i\rangle|^2 \cdot \frac{dN}{dE}, \tag{1.5}$$

where G_F denotes the coupling constant and $|\langle f|M_{fi}|i\rangle|$ the transition matrix, composed of $\langle f|$ the wave function of the final states, $|i\rangle$ the wave function of the initial state and M_{fi} the transition probability. $\frac{dN}{dE}$ denotes the final state density.

With this theory, E. Fermi was the first who was able to reconstruct the continuous β-decay spectrum and therefore give a theoretical explanation for the existence of the neutrino.

In the following years, the weak interaction was formulated and finally combined with the electromagnetic to the electroweak interaction, which is still a state-of-the-art theory [Gla61],[Wei67],[Sal68]. The theory describes several interactions in which neutrinos are

[1] Originally, W. Pauli named the new particle neutron. But in 1932, J. Chadwick discovered a particle which seems to be the counterpart of the proton- the neutron, and therefore W. Pauli's particle got its today's name [Cha32].

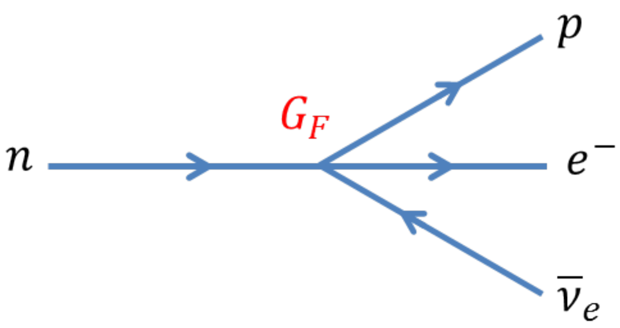

Figure 1.1.: A neutron decays in an one-vertex Fermi interaction to a proton, emitting an electron anti-neutrino and an electron. Because of the short range of the massive W boson, the Fermi one-vertex interaction is a good approximation for low energies.

emitted or absorbed, such as the inverse β-decay

$$\text{inverse } \beta^- - \text{decay}: \qquad \overline{\nu}_e + \mathrm{p} \rightarrow \mathrm{n} + \mathrm{e}^+ \tag{1.6}$$

$$\text{inverse } \beta^+ - \text{decay}: \qquad \nu_e + \mathrm{n} \rightarrow \mathrm{p} + \mathrm{e}^-. \tag{1.7}$$

The inverse β-decay allows to detect neutrinos and hence to prove the validity of electroweak interaction. However, the cross section of the inverse β-decay is very small (approximately 10^{-5} fb) [Zub12].

1956 - Project Poltergeist

In 1956, a team around C.L. Cowan and F. Reines, found first evidence of a direct neutrino measurement at the Savannah River Nuclear Power Plant in South Carolina, USA [Cow56b]. The experiment detected electron anti-neutrinos via inverse β-decay (equation 1.6). The thereby generated positron annihilates instantly to two monoenergetic photons with an energy of 511 keV (the exact mass of the positron). The neutron propagated through the water tank and lost energy due to scattering processes. After a few microseconds, the energy of the neutron was in the eV-range and it was captured by a ^{113}Cd nucleus, which was solved in the water. Subsequently, the excited ^{114}Cd nucleus decayed in an gamma decay and emitted from one to many photons

$$\mathrm{n} +^{113} \mathrm{Cd} \rightarrow^{114} \mathrm{Cd}^* \rightarrow^{114} \mathrm{Cd} + \gamma. \tag{1.8}$$

The detection method is summarized in figure 1.3.

The nearby nuclear reactor delivered high rates of electron anti-neutrinos, with a flux of up to $5 \cdot 10^{13}$ $\bar{\nu}_e/(\mathrm{s} \cdot \mathrm{cm}^2)$. The experimental setup contained of a tank with a fluid solution of $\mathrm{CdCl_2}$ surrounded by two fluid scintillators. The scintillator material generated flashes of light in response to gamma rays, which were then detected by photomultipliers. The photons coming from the positron annihilation and the neutron capture created a characteristic coincidence signal that allowed to identify the neutrino.

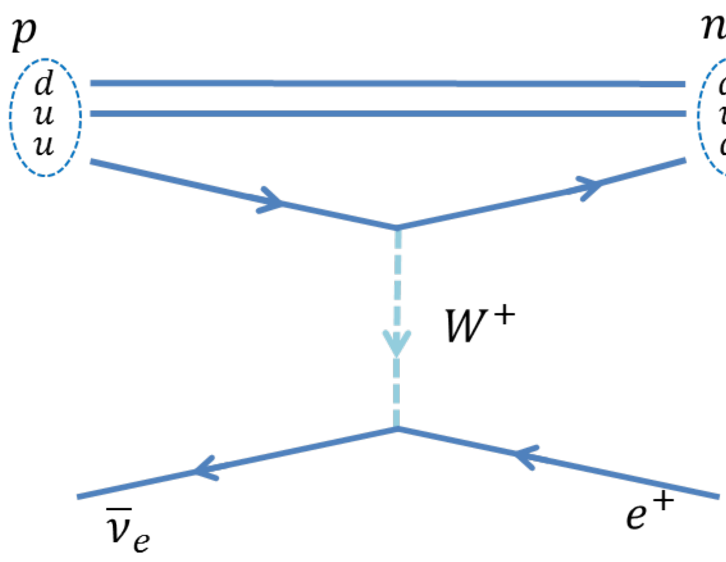

Figure 1.2.: The inverse β-decay on quark level, where an anti-neutrino gets absorbed and a positron is emitted. The interaction between the anti-neutrino and the up quark of the proton is mediated by exchanging a W^+ boson.

The measured cross section of

$$\overline{\sigma} = (11 \pm 2.6) \times 10^{-44}\ \mathrm{cm}^2 \tag{1.9}$$

is in good agreement with the electroweak theory of E. Fermi [Cow56a].

Discovery of ν_μ and ν_τ

In 1962, L.M. Lederman, M. Schwartz and J. Steinberger proved, that neutrinos coming from pion decays, are different from β-decay electrons. If ν_μ and ν_e were identical particles, then the decays

$$\nu_\mu + \mathrm{n} \rightarrow \mu^- + \mathrm{p} \tag{1.10}$$

$$\overline{\nu}_\mu + \mathrm{p} \rightarrow \mu^+ + \mathrm{n} \tag{1.11}$$

$$\nu_\mu + \mathrm{n} \rightarrow \mathrm{e}^- + \mathrm{p} \tag{1.12}$$

$$\overline{\nu}_\mu + \mathrm{p} \rightarrow \mathrm{e}^+ + \mathrm{n} \tag{1.13}$$

should be observed with the same rate. If $\nu_\mu \neq \nu_e$ was true, the decay modes 1.12 and 1.13 should not be observed at all.
The experiment was performed at the AGS-accelerator in Brookhaven Laboratory in Long Island, New York. By bombarding a beryllium target with a 15 GeV proton beam, pions and kaons were created, which subsequently decayed in muons and neutrinos via

$$\pi^+ \rightarrow \mu^+ + \nu_\mu \quad \text{and} \quad \pi^- \rightarrow \mu^- + \overline{\nu}_\mu \tag{1.14}$$

$$K^+ \rightarrow \mu^+ + \nu_\mu \quad \text{and} \quad K^- \rightarrow \mu^- + \overline{\nu}_\mu . \tag{1.15}$$

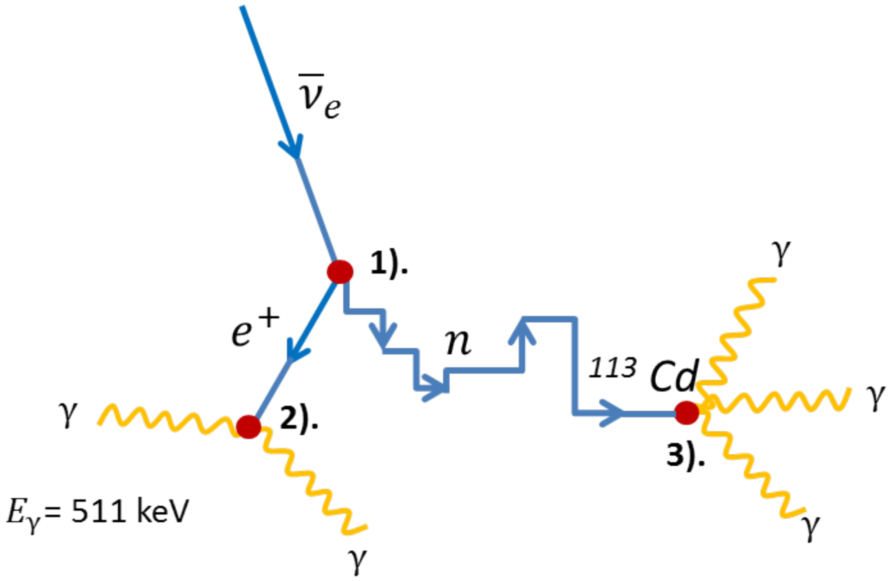

Figure 1.3.: An electron anti-neutrino decays in an inverse β-decay (point 1) to a positron and a neutron. The positron annihilates in two photons with an energy of 511 keV (point 2). A delayed gamma signal is coming from the neutron capture (point 3).

The muons and the remaining hadrons that did not decay, were shielded by an 13.5 m iron absober. The almost pure muon (anti-)neutrino beam was detected in a 10 t spark chamber. Electrons and muons were discriminated by their tracking properties: While electrons create electromagnetic showers, muons produce straight lines.

Overall, 29 muon events were observed [Dan62] and only 6 electron events, originating from the rare kaon-decay channel

$$K^+ \rightarrow \mathrm{e}^+ + \nu_e + \pi^0, \tag{1.16}$$

which gave clear evidence, that the neutrino has at least two different flavor.

After the observation of the τ-lepton in 1975 by M.L. Perl at the SLAC accelerator in Stanford [Per75], the tau neutrino was naturally expected to exist. However, its discovery took several years. In 2000, the DONUT experiment at the Fermi Lab in Chicago observed the decay channel

$$\nu_\tau + \mathrm{n} \rightarrow \tau^- + \mathrm{p}. \tag{1.17}$$

A ν_τ-beam was generated by the decay of D-mesons, coming from 800 GeV proton - wolfram collisions. The decay of equation 1.17 was observed with the help of emulsions plates. Because of the very short mean lifetime of τ-leptons of only $\tau = 3 \times 10^{-13}$ s, the expected τ-kink of a few mm, was difficult to detect. But four τ events were sufficient, to prove the existence of the last neutrino flavor, and complete the Standard Model with its three charged leptons (e, μ, τ) and its three neutrino counterparts (ν_e, ν_μ, ν_τ) [Kod01].

1.2. Neutrino Oscillation

The solution of the solar neutrino problem in 2001 by the SNO-Experiment [SNO02], was a milestone in neutrino physics. The experiment has shown that neutrinos oscillate between the three flavors of the Standard Model (SM), and therefore have to be massive. Consequently, the SM in which neutrinos were assumed to be massless, has to be extended.

The Solar Neutrino Problem

In the 1960's, R. Davies and J. Bahcall designed and build a neutrino experiment, which aimed to detect neutrinos coming from nuclear fusion in the sun [Dav94]. J. Bahcall worked at the forefront of developing the Standard Solar Model (SSM) [Bah05]. Based on J. Bahcall's SSM, the neutrino spectrum of the sun was predicted as it can be seen in figure 1.4.
The experiment took place in the Homestake Gold Mine in Lead, South Dakota. It consisted of an 100,000 Gallon (about 400 cubic meter) perchlorethylene tank. The neutrinos were captured by the chlorine nuclei due to an inverse β-decay

$$\nu_e +^{37} \mathrm{Cl} \rightarrow^{37} \mathrm{Ar} + \mathrm{e}^-, \tag{1.18}$$

with a Q-value of the capturing process of 0.814 MeV. Therefore, only three fusion processes were relevant for the Homestake experiment

$$^7\mathrm{Be} + \mathrm{e}^- \rightarrow \ ^7\mathrm{Li} + \nu_e \quad \mathrm{E}_\nu = 0.862 \text{ MeV} \tag{1.19}$$

$$^8\mathrm{B} \rightarrow \ ^7\mathrm{Be} + \mathrm{e}^- + \nu_e \quad \mathrm{E}_\nu \leq 14.6 \text{ MeV} \tag{1.20}$$

$$^3\mathrm{He} + \mathrm{p} \rightarrow \ ^4\mathrm{He} + \mathrm{e}^- + \nu_e \quad \mathrm{E}_\nu \leq 18.773 \text{ MeV}. \tag{1.21}$$

Every few weeks, R. Davis washed the ^{37}Ar atoms out of the tank, using Helium bubbles. In a separate tank, the ^{37}Ar atoms were counted by their decay via electron capture to excited ^{37}Cl* which sends out an Auger electron with an energy of 2.8 keV.
After 108 runs (1970 - 1995), Davis measured a rate of

$$R_{\mathrm{exp}} = 2.56 \pm 0.16 \text{ (stat.)} \pm 0.16 \text{ (syst.) SNU} \tag{1.22}$$

where SNU is the solar neutrino unit and relates to 1 ν_e capture per second with 10^{36} target nuclei [Bah01]. J. Bahcall's SSM however, predicted a rate of

$$R_{\mathrm{theo}} = 7.6^{+1.2}_{-1.1} \text{ (syst.) SNU} \tag{1.23}$$

which is approximately three times as much as the measured rate [Cle98].

In the following years, many experiments using different techniques confirmed the results from R. Davis' Homestake experiment (e.g. SAGE [SAG02], Gallex [GAL99] or

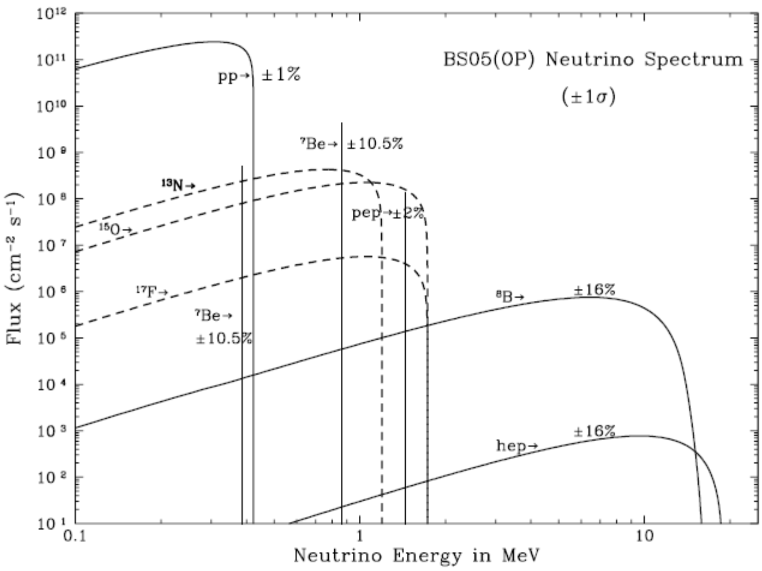

Figure 1.4.: Energy spectra from neutrinos coming from nuclear fusion in the sun (double logarithmic presentation). Discrete lines are coming from two body, continuous from three body decays. Figure from [Bah05].

Kamiokande [Kam96]).
Many approaches to explain the missing neutrinos were made, such as different solar models or other astrophysical explanations. However, the most promising approach was the theory of neutrino oscillation (first predicted by B. Pontecorvo 1958 [Pon58]). If neutrinos oscillate, they are created with one flavor and change it during propagation through space and time. This could explain why two third of the solar electron neutrinos are missing. A prerequisite for neutrino oscillation to occur, is a non-zero neutrino mass, unlike assumed in the SM.

SNO Results

In 2001, the Sudbury Neutrino Observatory (SNO) solved the problem of the missing neutrinos [SNO02] by proving that neutrinos indeed oscillate as predicted by B. Pontecorvo's theory. The experiment was placed in the Vale Inco's Creighthon Mine in Ontario, Canada, and consisted of a 1000 t heavy water tank (D_2O). It was provided with two different ways to detect neutrinos. One process was only sensitive for electron neutrinos, while the other allowed a detection of neutrinos of all flavors.
In the first stage of the experiment, electron neutrinos were detected via charged current decays (see figure 1.5 a). An electron neutrino interacts with a neutron of the deuteron nucleus, and generates an electron and a proton. The electrons were detected with Cherencov detectors[2].
The energy of the observed solar neutrinos were in the range of a few MeV. Muons as well as tauons have rest masses of $m_\mu = 105.7$ MeV and $m_\tau = 1.777$ GeV and could therefore

[2] Charged particles emit a specific electromagnetic radiation, if they propagate through a dielectric medium with velocities faster than the phase velocity of light in the certain medium

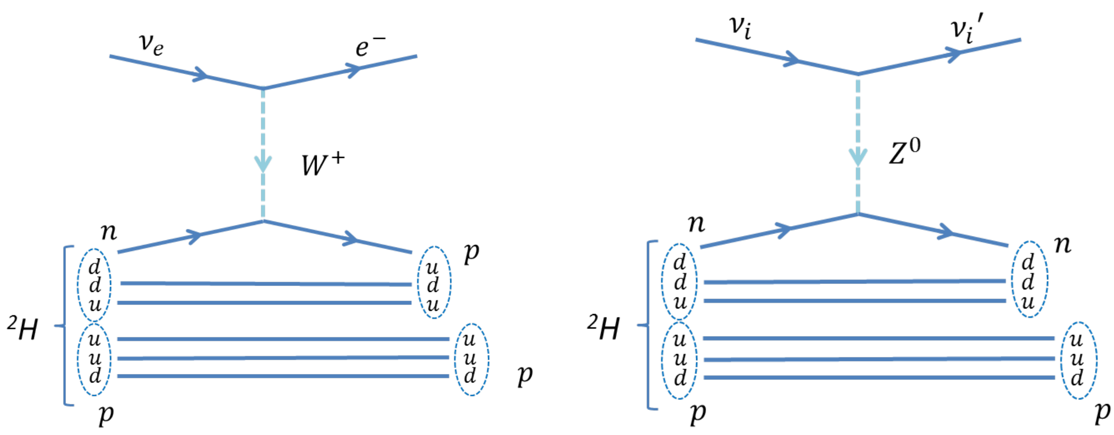

(a) (b)

Figure 1.5.: An electron neutrino splits up a deuteron nucleus into two protons, through a charged current interaction (a). While this decay was only sensitive to neutrinos with electron flavor, the neutral current interaction (b) was sensitive to all flavor. A neutral Z^0 boson exchanges energy from the neutrino to the neutron of the deuteron. As a consequence, the molecule splits up in a free neutron and proton.

not be generated via the charged current process.

In an second phase of the experiment, neutral current processes (see figure 1.5 b), where neutrinos of all flavor could be involved, were investigated. Exchanging a neutral vector boson (Z^0), neutrinos can scatter with neutrons. If they do so, and their energy is bigger than $E_\nu > 2.2$ MeV, they can break up the binding of the deuteron nucleus, which results in a free proton and neutron. The free neutron was captured with a ^{36}Cl atom which later deexcites, emitting a photon with $E_\gamma = 8.64$ MeV.

Both phases combined, let to the rates

$$\nu_e - \text{flux}: \qquad \Phi = 1.68 \pm 0.06\ (\text{stat.}) \pm 0.09\ (\text{syst.}) \tag{1.24}$$

$$\nu_{e,\mu,\tau} - \text{flux}: \qquad \Phi = 4.94 \pm 0.22\ (\text{stat.}) \pm 0.15\ (\text{syst.}). \tag{1.25}$$

$$\tag{1.26}$$

The predicted flux of (SSM)

$$\nu_{e,\mu,\tau} - \text{flux}: \qquad \Phi = 5.69 \pm 0.91\ (\text{theo.}) \tag{1.27}$$

lays within the statistical and systematical errors of the experiment. The first results were published in June 2001, bringing the first clear evidence that neutrinos oscillate in the sun and on their way to the earth.

Theoretical Description of Neutrino Oscillations

The theoretical foundation of neutrino oscillation is, that the mass eigenstates and the flavor eigenstates of neutrinos are non-identical [Pon58]. The neutrinos propagate in their mass eigenstates and interact in their flavor eigenstates.

Figure 1.6.: The mixing parameters of the three neutrino generations. Data from [Oli14]

1st & 2nd Generation	2nd & 3rdGeneration	1st & 3rd Generation
$\theta_{12} = (33.29 \pm 4.166)°$	$\theta_{23} = (45.00 \pm 3.746)°$	$\theta_{13} = (8.87 \pm 2.566)°$
$\Delta m^2_{12} = 7.5 \cdot 10^{-5}$ eV²	$\Delta m^2_{23} = 2.3 \cdot 10^{-3}$ eV²	$\Delta m^2_{13} = \Delta m^2_{12} + \Delta m^2_{23}$

The Pontecorvo-Maki-Nakagawa-Sakata (PMNK) matrix, describes the mixing probability of the three mass eigenstates

$$\begin{pmatrix} \nu_e \\ \nu_\mu \\ \nu_\tau \end{pmatrix} = \begin{pmatrix} \mathrm{U}_{11} & \mathrm{U}_{21} & \mathrm{U}_{31} \\ \mathrm{U}_{12} & \mathrm{U}_{22} & \mathrm{U}_{32} \\ \mathrm{U}_{13} & \mathrm{U}_{23} & \mathrm{U}_{33} \end{pmatrix} \cdot \begin{pmatrix} \nu_1 \\ \nu_2 \\ \nu_3 \end{pmatrix} \tag{1.28}$$

and can be uncoupled to three separate matrices describing the mixing of the three different generations of neutrinos

$$\mathrm{U} = \begin{pmatrix} 1 & 0 & 0 \\ 0 & \cos\theta_{23} & \sin\theta_{23} \\ 0 & -\sin\theta_{23} & \cos\theta_{23} \end{pmatrix} \cdot \begin{pmatrix} \cos\theta_{13} & 0 & \sin\theta_{13}\cdot \mathrm{e}^{-i\delta} \\ 0 & 1 & 0 \\ -\sin\theta_{13}\cdot \mathrm{e}^{-i\delta} & 0 & \cos\theta_{13} \end{pmatrix} \cdot \begin{pmatrix} \cos\theta_{12} & \sin\theta_{12} & 0 \\ -\sin\theta_{12} & \cos\theta_{12} & 0 \\ 0 & 0 & 1 \end{pmatrix} \tag{1.29}$$

where θ_{ij} denotes the mixing angles, and $\mathrm{e}^{-i\delta}$ a CP violating phase.
The expression for specific oscillation transition, for example from electron to muon neutrinos, is

$$P(\nu_e \to \nu_\mu) = \sin^2 2\theta_{13} \cdot \sin\theta_{23} \cdot \sin^2\left(\frac{\Delta m_{12} L}{4E}\right) \tag{1.30}$$

where Δm_{12} denotes the mass difference of the two mass eigenstates, θ_{12} and θ_{23} the mixing angles of the mass eigenstates, E the energy of the neutrino, and L its oscillation length.
Because of the separability of the mixing matrix, the mixing angles θ_{ij} and the mass differences $\mathrm{m}^2_{ij} = |\mathrm{m}^2_i - \mathrm{m}^2_j|$ can be determined for example in experiments, measuring the appearance and disappearance of neutrino fluxes from nuclear reactors or particle accelerators [Zub12]. Figure 1.6 gives the current best measurements of the oscillation parameters.

1.3. Neutrino Mass

In the SM, spin half-integer particles (fermions) get their mass via interactions with the Higgs field. These interactions involve right- and left-handed fermions. Since no right-handed neutrino has been discovered yet, the neutrino is assumed to be massless in the SM. However, neutrino oscillations require a non-vanishing neutrino mass. There are many

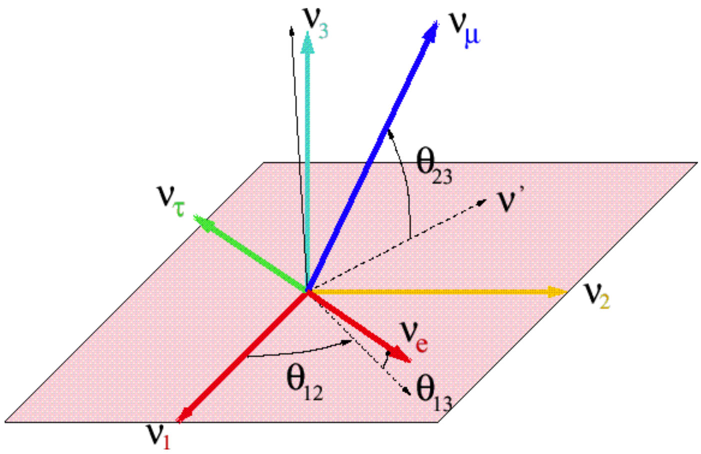

Figure 1.7.: The neutrino flavor as a superposition of the three mass eigenstates. θ_{ij} determines the angles between the mass eigenstates. Illustration from [Dre12].

ways to explain the generation of neutrino mass in theories beyond the SM. The most common is the so-called see-saw mechanism [Pet13].

The difference of the eigenvalues of the three mass eigenstates, can be measured in oscillation experiments and are known to good precision. The absolute neutrino mass however, is still unknown. The current best limit

$$\mathrm{m}_\nu < 2\mathrm{eV} \tag{1.31}$$

arises from tritium β-decay experiments (combined analyze by the particle data group [Oli14] using results by the Mainz [Bon01] and Troitsk [Lob99] neutrino mass experiments). The scale of the mass is of importance, since it determines whether the neutrino masses are degenerated or hierarchical (see figure 1.8). If the total neutrino mass is in the eV-scale, than the mass differences Δm_{ij} are so small, that they are effectively degenerated. If the mass however, would be of the same order as the Δm_{ij}, than the three mass eigenstates would have a clear hierarchy.

Furthermore, the neutrino mass is of great interest for cosmology. In their role as dark matter, neutrinos have a large impact on the structure formation in the early universe. A precise knowledge of their mass would be an important input parameter for cosmological simulations. In the following, three ways of measuring the neutrino mass will be presented.

Neutrino Mass from Cosmology

The ΛCDM-model is the state of the art model, that explains the origin of the universe in a very hot big bang with an extreme high energy density [Dre12]. After the big bang, the universe started to expand and cool down. When the temperature was low enough, the different particles of the SM decoupled. A strong evidence that supports the ΛCDM-model, is the observation of the cosmic microwave background (CMB). This isotropic and homogeneously distributed photon background (with a temperature of $T = 2.725$ K) was first predicted 1948 by A. Alpher and R. Herman [Alp48] and observed 1965 by A. Penzias and R.W. Willson [Pen65]. The photons from the CMB have decoupled in an early phase

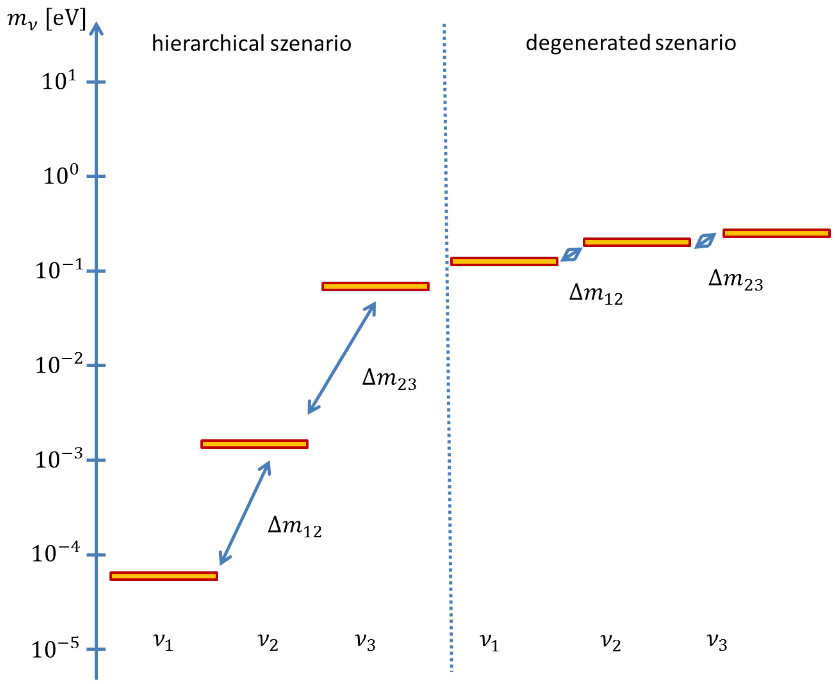

Figure 1.8.: The total neutrino mass would answer the question, whether the three neutrino mass eigenstates have a clear hierarchy (left side) or are degenerated (right side).

of the universe. With the number of the photons and their energy, the contribution of the CMB to the total energy density Ω_{tot} of the universe can be calculated [Per03].
The ΛCDM model also predicts the time, when neutrinos decoupled. Using the information of the CMB and the ΛCDM model, the relic neutrino background can be predicted. These low energy neutrinos would have a today temperature of $T = 1.95$ K and a density of $n_\mu = 336$ cm^{-3}. The contribution of the relic neutrinos Ω_ν to the total matter density can be calculated, using the sum of the mass eigenstates

$$\Omega_\nu = \frac{\sum_i m_i}{93.14 h^3 eV} \tag{1.32}$$

with h the dimensionless Hubble constant [Les12].
The neutrino mass is derived by observations of the universe structure. A high neutrino mass would have let to a wash-out of small structures in the early universe (see chapter 1.4). Recent results from the Planck experiment [Pla14] have set an upper limit to the m_{tot} of

$$m_{\text{tot}} = \sum_i m_i < 0.230 \text{ eV } (95\% \text{ C.L.}). \tag{1.33}$$

However, because of their low energy (sub-eV scale), relic neutrinos have not been detected yet.
Since the interpretation of cosmological observations strongly depends on the underlying astrophysical models, model-independent laboratory experiments are important complementary probes.

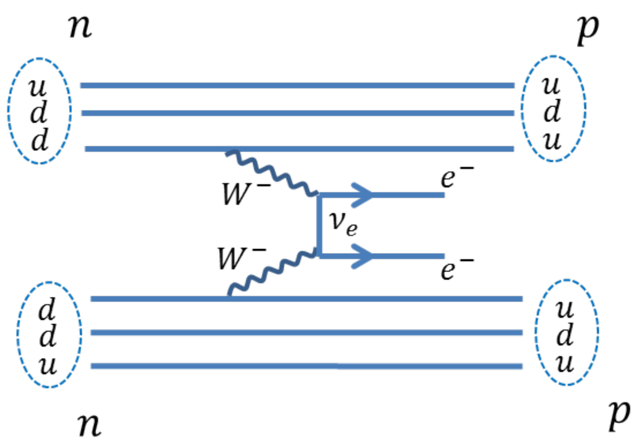

Figure 1.9.: The neutrinoless double β-decay. Two neutrons decay in a charged current process, exchanging a virtual neutrino, to two protons and two electrons.

Neutrinoless Double β-Decay

The neutrinoless double β-decay ($0\nu\beta\beta$) is a very rare nuclear decay where two simultaneous β-decays take place but no neutrino is emitted

$$(\mathrm{Z}, \mathrm{A}) \rightarrow (\mathrm{Z}+2, \mathrm{A}) + 2\mathrm{e}^{-}. \tag{1.34}$$

For this decay to be allowed, the neutrino needs to be its own antiparticle (a so-called Majorana particle). In this case, a virtual Majorana neutrino will be exchanged between the two involved nuclei (see figure 1.9). However, the $0\nu\beta\beta$ violates lepton number conservation and is hence not possible via a SM interaction. The rate of these very rare events, is proportional to the so-called Majorana-mass ($m_{\beta\beta}$)

$$\Gamma_{0\nu\beta\beta} \propto |\sum_i \mathrm{U}_{ei} m_i|^2 = m_{\beta\beta}. \tag{1.35}$$

Experiments like the MAJORANA experiment in South Dakota [MAJ14], or the GERDA experiment in Gran Sasso [GER06], search for the $0\nu\beta\beta$, both using ^{76}Ge as a source and detector.
The recent limit on the Majorana neutrino mass is

$$m_{\beta\beta} < (0.2 - 0.4)\ \mathrm{eV}. \tag{1.36}$$

given by the GERDA experiment [GER13].
The neutrino mass determination based on $0\nu\beta\beta$-experiments, relies on detailed models of the decay and the Majorana nature of the neutrino. Like astrophysical observations they cannot replace a direct kinematic measurement by single β-decay experiments.

Single β-Decay Experiments

The only model-independent method to determine the neutrino mass, are single β-decay

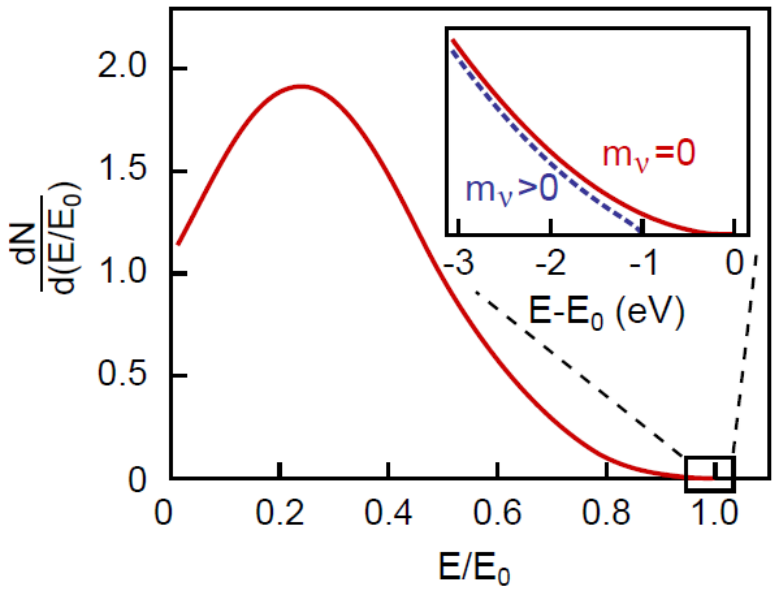

Figure 1.10.: With a non-vanishing neutrino mass, the endpoint of the β-decay electron spectrum is shifted to lower energies. The red solid line is the spectrum resulting from a massless neutrino, the blue dotted line depicts the case for an effective neutrino mass of $m_\nu = 1$ eV. Figure from [Gro15].

experiments. This direct measuring method uses simple kinematic calculations.
In the β-decay

$$\mathrm{n} \to \mathrm{p} + \mathrm{e}^- + \overline{\nu}_e, \tag{1.37}$$

the energy of the decay is shared by the daughter nucleus, the electron and the neutrino, whereas the neutrino energy is given by

$$E_\nu = \sqrt{m_\nu^2 c^4 + p_\nu^2 c^2}. \tag{1.38}$$

Since the neutrino has a non-vanishing mass, the endpoint[3] of the β-decay spectrum is reduced and the spectrum is distorted in the close vicinity to it.
Several experiments have already measured the β-decay spectrum with different sensitivity [Bon01], [Lob99]. The next-generation, large-scale **K**arlsruhe **TRI**tium **N**eutrino Experiment (KATRIN) is designed to measure the neutrino mass with an unprecedented sensitivity of 200 meV. Chapter 2 will give a more detailed introduction to the KATRIN experiment and its experimental setup.

1.4. Neutrinos and Dark Matter

Several cosmological and astrophysical observations indicate, that ordinary baryonic matter makes up only 4.6% of the energy-density of the universe. A total of 26.8% of its energy density is so called dark matter (DM). The rest of the energy is dark energy which

[3]The maximal kinetic energy the electron can have is called the endpoint energy E_0.

is responsible for the accelerated expansion of the universe [Pla14].
DM was first predicted by the Austrian physicist F. Zwicky in 1933 [Zwi33]. He observed the Coma cluster (existing of about 1000 galaxies) and measured the peculiar velocity of galaxies of the cluster. The velocities were higher than classical Newton mechanics calculations would suggest. As an explanation, he proposed the existence of non-baryonic matter which, contributes with 90% to the matter of the coma cluster. Since the matter is not visible to telescopes (not interacting via electromagnetic interaction) F. Zwicky named it dark matter [Zwi33].
In the following decades, a number of independent observations supported Zwicky's theory of dark matter (e.g. gravitational lensing [Tay98] or the multipole analysis of the CMB data [Pla14]). Different approaches, for example the theory of **mo**dified **N**ewton **d**ynamics (MOND) [Mil94], failed to disprove the dark matter theory.
There are many different candidates for the still unidentified DM. Overall, they are classified in two groups: hot and cold dark matter, depending on their temperature profile at creation and respectively their free streaming length l_{fs}.
The free streaming length of dark matter has a large influence on the structure formation of the universe. It describes the average length of a particle propagating in a certain medium, before it interacts. DM particles with long l_{fs} are called hot dark matter (HDM). In a HDM dominated universe, small structures like galaxies would have been generated later than big structures (e.g. galaxy clusters), the so-called top-down scenario [Per03]. In a cold dark matter (CDM) scenario with short l_{fs}, small structures would have been generated first and the universe would have been formed in a bottom-up scenario [Per03].

Cold Dark Matter

Cold dark matter (CDM) particles are generally in the GeV mass range. The most common CDM candidates are the so-called Weakly Interacting Massive Particles (WIMPS).
The most promising candidates for WIMPS are the lightest supersymmetric particles, coming with the sypersymmetric extension of the SM (SUSY). SUSY postulates a supersymmetric partner to every particle in the SM. It was first formulated in 1974 by J. Wess and B. Zumino [Wes74]. It implies a Q-Operator, which transforms the spin of the SM particles by $\frac{1}{2}$, and changes therefore bosons to fermions and reverse[4].
In SUSY, a new quantum number, the R-parity, is conserved in all processes including SUSY and SM particles. Due to the conservation of the R-parity, the existence of a lightest supersymmetric particle (LSP), that cannot decay in a common SM particle, is assured. The LSP is the most promising candidate for the WIMP cold dark matter.
There are several experiments that aim to detect WIMPS directly and indirectly. For example the EDELWEISS-Experiment [Ede11] that uses a Germanium detector, measuring the scattering of WIMPS. However, direct and indirect measurements of WIMPS have not yet been successful.

[4]Besides providing a compelling dark matter candidate, SUSY is motivated by the mass hierarchy problem. This problem describes the fact that divergent loop diagrams lead to large corrections of the renormalized Higgs mass. To every quadratic divergent correction term, there is a supersymmetric counterpart with the exact same quantum numbers, but a difference in the spin of $\frac{1}{2}$. Since the sign of the correction terms are opposite (for fermions and bosons), the divergent terms cancel each other.

Hot Dark Matter

Light particles in the mass range of a few eV and free streaming lengths of $l_{fs} \approx 1$ Mpc are called hot dark matter (HDM). Relic neutrinos for example act as HDM. But the limitations on the neutrinos mass and the contribution of the neutrinos to the energy density of the universe (equation 1.32) exclude, that HDM is the dominant form of DM [Per03]. Furthermore, there are astrophysical observations that showed examples of galaxies which are older as the cluster they are part of, almost ruled out a top-down scenario, and hence a HDM dominated universe.

Warm Dark Matter

Another form of dark matter, which would be in agreement with small and large scale astrophysical observations, is warm dark matter (WDM). In contrast to CDM, it might allow to reconcile tensions in small scale structure observations, such as the so-called missing satellite problem [Kly99].
An auspicious candidate for WDM, is the sterile neutrino in the keV-mass range. The upcoming chapter gives a brief introduction of the phenomenological background and the properties of the sterile neutrino, astrophysical and cosmological observations related to sterile neutrinos and its impact on the β-decay electron spectrum.

1.5. Sterile Neutrinos

In the SM, all fermions occur with left- and right-handed chirality. The sole particle which has only been observed left-handed, is the neutrino. As a consequence, neutrinos are massless in the SM. Neutrino oscillation however, requires a non-vanishing neutrino mass.
A right-handed neutrino would not interact at all within the SM interactions (not even weakly), only gravitational and is therefore called sterile neutrino. However, it can mix with the active neutrinos via the interaction with the Higgs boson. The associated mass eigenstate, would hence be a superposition of the active and sterile neutrino states. In the following we will refer to this new mass eigenstate as sterile neutrino (even though strictly speaking it can have a admixture of active neutrinos).
Sterile neutrinos are a well-motivated extension of the SM, however, there is little theoretical and experimental guidance about the mass scale of this new neutrino species. The see-saw mechanism [Pet13] for example, postulates a very heavy sterile neutrino to explain the tiny masses of the active neutrinos [Sch80]. There are also theories that introduces light sterile neutrinos in the eV-scale, to explain experimental anomalies, like the reactor anomaly of the LSND experiment [Aba12].
This thesis considers neutrinos in the keV-mass range as proposed in [San11]. KeV-scale sterile neutrinos could account for a significant fraction of the DM in the universe. With masses in the keV-range and free streaming lengths of a few kpc they could be both, warm dark matter (WDM) and cold dark matter (CDM) depending on their creation mechanism [Aba94].
Sterile neutrinos are described via their mass m_{s} and their acive-sterile mixing amplitude

$\sin^2\theta$. Both parameters are broadly limited due to astrophysical and cosmological observations (see figure 1.11). The phase-space density evolution of dwarf spheroidal satellites in the Milky Way, give a model-independent upper limit to fermionic dark matter and respectively for the sterile neutrino mass of $m_\mathrm{s} > 2$ keV. Considering the hypothetical decay of a sterile to an active neutrino

$$\nu_s \rightarrow \nu_a + \gamma, \tag{1.39}$$

an upper limit of the sterile neutrino parameter space arises. The decay is loop suppressed and therefore very rare. Since it is relativistic, the energy coming from the decaying sterile neutrino would split up by a half to the emitted active neutrino and the photon, and would be observational in an X-ray emission line at the half sterile neutrino mass. Observations from X-ray telescopes like the XMM-Newton and Chandra lead to a limit of

$$m_\mathrm{s} < 50 \text{ keV} \tag{1.40}$$

$$10^{-13} < \sin^2 2\theta < 10^{-7} \tag{1.41}$$

from [Boy12].
Recently, the XMM-Newton telescope observed a weak X-ray emission line in stacked galaxy clusters, which could be the first evidence for relic sterile neutrinos [Bul14]. The results imply a mass of $m_\mathrm{s} = 7.1$ keV and an mixing angle of $\sin^2\theta = 7 \cdot 10^{-11}$. The same emission line was also observed at the Andromeda galaxy and the Perseus galaxy cluster [Boy14]. However, these astrophysical observations are strongly model-dependent and have to be firmly supported by laboratory experiments.

One way to observe the imprint of sterile neutrinos, is the single β-decay of nuclei with decay energies in the keV-scale. The mixing of active and sterile neutrinos would be manifested in a kink-like signature and a distortion of the β-decay spectrum.
In particular, the tritium β-decay has several advantages. It is a super-allowed decay (no change of the nuclear spin $0^+ \rightarrow 0^+$, $\Delta J = 0$), the half life of 12.3 years is very short (high signal rates), and the shape of the β-spectrum is theoretically well known. With an endpoint energy of $E_0 = 18.575$ keV, the sterile neutrino parameter space favored by astrophysical and cosmological observations (figure 1.40) is most widely covered.

1.5.1. Tritium β-Decay and Sterile Neutrinos

Nuclear tritium decays into helium

$$\mathrm{T_2} \rightarrow \mathrm{THe}^+ + \mathrm{e}^- + \overline{\nu}_e, \tag{1.42}$$

and emits an electron and a neutrino. The decay rate is given by

$$\frac{d\Gamma}{dE} = C \cdot F(E, Z = 2) \cdot p \cdot (E + m_e) \cdot (E_0 - E) \sum_i |U_{ei}|^2 \sqrt{(E_0 - E)^2 - m_{\nu_i}^2} \tag{1.43}$$

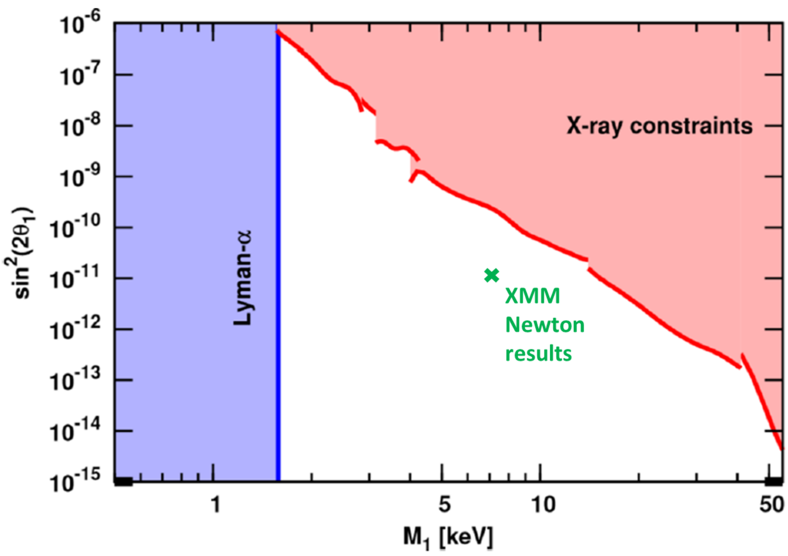

Figure 1.11.: Observing the lyman-α lines of dwarf spheroidal satellites in the Milky Way, the mass of the keV-scale sterile neutrino is limited to approximately 2 keV (blue area). X-ray constrains, coming from XMM and Chandra data, exclude the red shaded area. New results from stacked galaxy clusters X-ray observations imply an sterile neutrino with $m_\mathrm{s} = 7.1$ keV and $\sin^2\theta = 10^{-11}$ [Bul14], [Boy14] (green marker). Figure from [Bez11].

where m_{ν_i} denotes the neutrino mass eigenstates, E_0 the endpoint energy, E the kinetic energy of the emitted electron, p its momentum and m_e the electron mass. The Fermi function $F(E, Z = 2)$ represents the correction of the spectrum due to Coulomb interaction between the outgoing electron and the daughter nucleus. C is a normalization constant given by

$$C = \frac{G_F^2}{2\pi^3}\cos^2\Theta_C |M|^2, \tag{1.44}$$

with the Fermi constant G_F, the Cabbibo mixing angle Θ_C and the nuclear transition matrix M (see also section 1.5).

Because no current β-decay experiment is able to resolve the tiny mass differences of the three neutrino mass eigenstates, they are combined to one effective light neutrino mass $m^2_\mathrm{light} = \sum_{i=1}^{3} |U_{ei}|^2 m^2_{\nu_i}$.

If however, there is another neutrino mass eigenstate in the keV-mass range, the different mass eigenstates will no longer form a single effective mass term. The large mass splitting will lead to a superposition of the β-decay spectra corresponding to the light mass term m_light and the sterile neutrino mass term m_s

$$\frac{d\Gamma}{dE} = \cos^2\theta \frac{d\Gamma}{dE}(m_\mathrm{light}) + \sin^2\theta \frac{d\Gamma}{dE}(m_\mathrm{s}) \tag{1.45}$$

with the active-sterile neutrino mixing angle θ.

Figure 1.12 shows a β-decay spectrum with and without active-sterile neutrino mixing. At the energy region $E < E_0 - m_\mathrm{s}$, the decay into a sterile neutrino is energetically allowed, thus the phase space changes due to the non-relativistic sterile neutrino (low kinetic energies opposed to the high mass of the sterile neutrino).

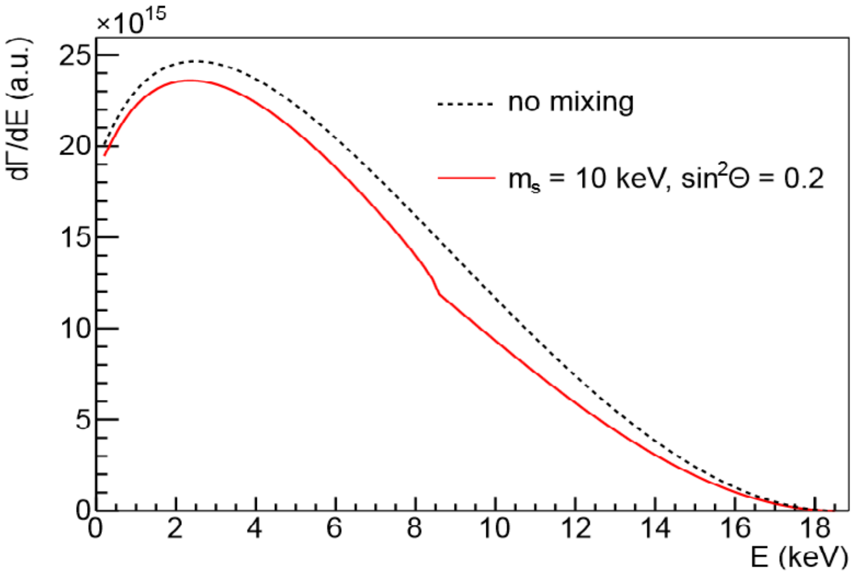

(a)

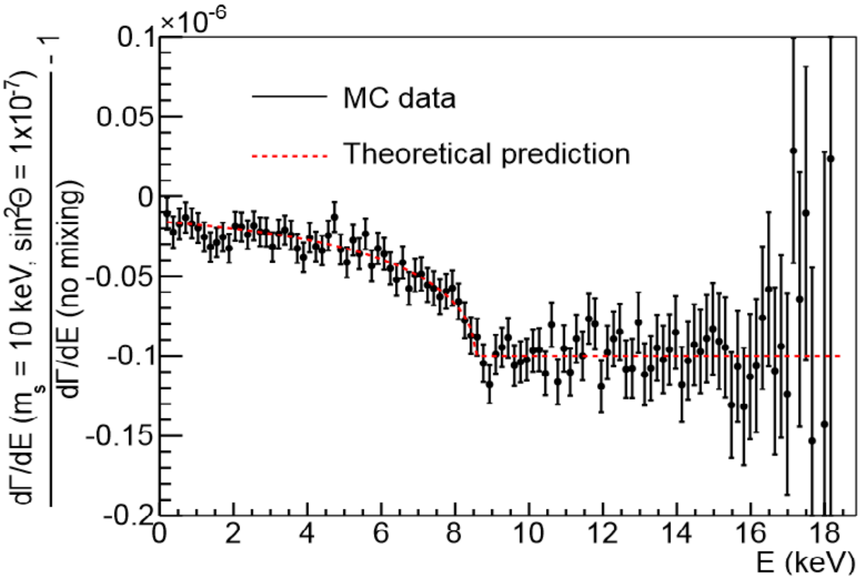

(b)

Figure 1.12.: A β-decay spectrum with active-sterile neutrino mixing (solid line) and a spectrum without (dashed line). The sterile neutrino has a mass of $m_{\mathrm{s}} = 10$ keV and an unphysically large mixing amplitude of $\sin^2\theta = 0.2$ (a). The kink-like signature at $E = E_0 - m_{\mathrm{s}}$ is clearly visible. The ratio of the β-decay spectra with mixing of a sterile neutrino with $m_{\mathrm{s}} = 10$ keV and a mixing amplitude of $\sin^2\theta = 10^{-7}$, and without mixing (b). The error bars correspondent to a number of 10^{18} electrons (3 years measuring time with the KATRIN experiment at full source strength). Figures from [Mer14].

The kink appears at an electron energy of $E = E_0 - m_{\mathrm{s}}$, the amplitude of the kink is mainly influenced by the mixing amplitude $\sin^2\theta$.

2. The KArlsruher TRItium Neutrino Experiment

The **KA**rlsruhe **TRI**tium **N**eutrino experiment (KATRIN) is a large-scale, next-generation tritium β-decay experiment, with the primary goal to directly determine the effective mass of the electron anti-neutrino in a model-independent way. After 3 years of measuring time, KATRIN will reach a sensitivity of 200 meV (90% C.L.).
This chapter will give an introduction to the working principle of the KATRIN experiment and the main components of the experimental setup. Furthermore, it will be explained how the KATRIN experiment could be used to search for keV-scale sterile neutrinos, and hence provide an opportunity to use the experiment beyond the main goal of determining the neutrino mass.

2.1. Measurement Principle and Sensitivity to the Absolute Neutrino Mass

Since a non-vanishing neutrino mass reduces the endpoint and distorts the spectral shape of the tritium β-decay spectrum in the close vicinity to it, KATRIN measures the tritium β-decay spectrum with very high precision. To obtain this challenging high-precision spectroscopy, KATRIN utilizes a high-pass electron filter, that uses the technique of **M**agnetic **A**diabatic **C**ollimation (MAC-E filter), which is described in the following section.

The MAC-E Filter

The groups of the Troitsk and Mainz neutrino experiments were the first who developed the MAC-E filter principle for β-spectroscopy. This setups reached an energy resolution of $\Delta E = 3.5$ eV [Lob99],[Bon01]. The working principle of a MAC-E filter is the following:
The kinetic energy of the electrons

$$E_{\mathrm{kin}} = E_{\mathrm{L}} + E_{\mathrm{T}}. \tag{2.1}$$

is composed of a transversal component E_{T} perpendicular to the magnetic field lines, and a longitudinal component E_{L} parallel to the magnetic field lines.

The electric field of the retarding potential at the analyzing plane of the spectrometer is parallel to the magnetic field. Therefore, only the longitudinal kinetic energy of the signal electrons is determining, whether it is transmitted through the spectrometer or not. In order to analyze the total kinetic energy of the electrons, the transversal component has to be transformed into longitudinal energy, i.e. the polar angle θ (see figure 2.1) needs to be minimal at the analyzing plane. The entire transformation needs to be an adiabatic process, which can be expressed to first order by the conservation of the orbital magnetic moment

$$\mu = \frac{E_\perp}{B} = \text{const.} \tag{2.2}$$

A small magnetic and electric field gradient

$$\frac{\Delta B}{B} << \quad \text{and} \quad \frac{\Delta E}{E} << 1 \tag{2.3}$$

are crucial, to assure an adiabatic transport.
According to equation 2.2, a reduction of the magnetic field B at the analyzing plane ($B_\mathrm{s} \to B_\mathrm{a}$), leads to a conversion of transversal into longitudinal kinetic energy of the electron ($E_\perp \to E_\parallel$). The longitudinal energy is then transformed into potential energy by the spectrometer potential.
However, the magnetic field in the analyzing plane can not be dropped to zero to assure magnetic guidance[1]. Consequently, a small fraction of transversal kinetic energy remains. This fraction determines the energy resolution

$$\Delta E = \frac{B_\mathrm{min}}{B_\mathrm{max}} \cdot E_\mathrm{kin,max} = \frac{3 \cdot 10^{-4}\ \mathrm{T}}{6\ \mathrm{T}} \cdot 18.6\ \mathrm{keV} = 0.93\ \mathrm{eV} \tag{2.4}$$

of the MAC-E filter.
In addition to the magnetic adiabatic collimation and electrostatic filtering, the MAC-E filter can be used to adjust the acceptance angle of the experiment. After the electrons pass the analyzing plane the magnetic field rises again, and hence longitudinal energy is transformed back into transversal energy ($E_\parallel \to E_\perp$), i.e. the polar angle θ increases again. By applying a higher magnetic field at the exit of the spectrometer than at the source section of KATRIN, electrons with a large starting angle, reach $\theta = 90°$ at the maximum field and will be reflected. With the magnetic field in the source of 3.6 T and the highest field of 6 T at the pinch magnet, the maximum starting angle (acceptance angle) θ_max is given by

$$\theta_\mathrm{max} = \arcsin\left(\sqrt{\frac{B_\mathrm{s}}{B_\mathrm{max}}}\right) = \arcsin\left(\sqrt{\frac{3.6\mathrm{T}}{6\mathrm{T}}}\right) = 50.77°. \tag{2.5}$$

As a consequence, more than two thirds of the electrons created in the source, are unable to reach the detector. The decrease of the number of electrons (resulting in lower statis-

[1] In the KATRIN experiment, the electrons are transported from the source to the detector via a magnetic guidance. The guidance is assured by multiple sequentially arranged superconducting solenoids.

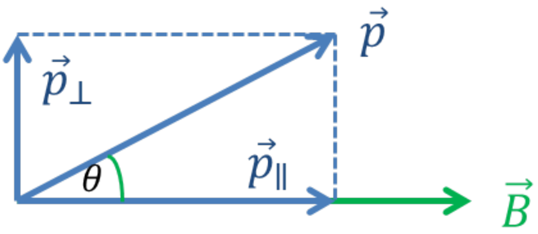

Figure 2.1.: The polar angle θ denotes the angle between the momentum vector of the electron $\vec{p}$ and the magnetic field $\vec{B}$. It is decomposed in a transversal $\vec{p}_\perp$ and a longitudinal fraction $\vec{p}_\parallel$.

tics), is justified by a decrease of the systematical error, due to the higher probability of scattering processes and energy loss due to synchrotron radiation, of electrons with high polar angles θ.

Sensitivity to the Absolute Neutrino Mass

To observe the influence of a non-vanishing neutrino mass ($m_\nu \neq 0$), KATRIN measures the integrated tritium β-decay spectrum, close to the endpoint E_0, where the influence of m_ν is maximal (see figure 2.7). At different retarding potentials U, the integrated β-spectrum is given by

$$N(qU) \propto t_{\mathrm{qU}} \int_0^{E_0} \frac{dN}{dE}(E_0, m_\nu^2) \cdot R(E, qU) dE \tag{2.6}$$

with t_{qU} the measuring time at a specific retarding potential U and $\frac{dN}{dE}(E_0, m_\nu^2)$ the rate of the β-decay. $R(E, qU)$ represents the response function.
The response function is composed of two parts. It entails both, the information about energy loss of the signal electrons due to scattering and the transmission probability through the spectrometer. The normalized energy loss function $f(\epsilon)$ describes the probability of the electron loss ϵ as a result of inelastic scattering processes (with the cross section σ_{inel}), and is given by

$$f(\epsilon) = \frac{1}{\sigma_{\mathrm{inel}}} \cdot \frac{d\sigma}{d\epsilon}. \tag{2.7}$$

The transmission probability of the signal electrons through the main spectrometer is expressed by the transmission function

$$T(E, qU) = \begin{cases} 0 & E - qU < 0 \\ \frac{1-\sqrt{1-\frac{E-qU}{E}\cdot\frac{B_{\mathrm{s}}}{B_{\mathrm{a}}}}}{1-\sqrt{1-\frac{B_{\mathrm{s}}}{B_{\mathrm{max}}}}} & 0 \leq E - qU \leq \Delta E, \\ 1 & E - qU > \Delta E \end{cases} \tag{2.8}$$

where B_{s} is the magnetic field in the source, B_{a} the magnetic field in the analyzing plane,

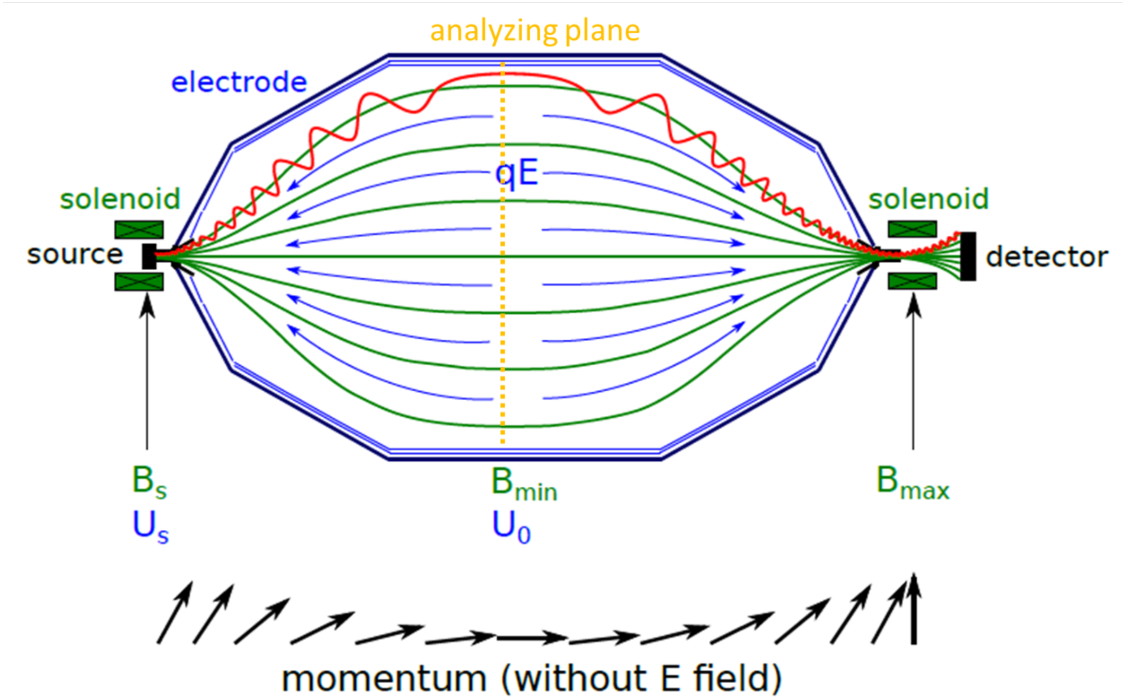

Figure 2.2.: The solenoid magnets generate a magnetic field (green lines), which guides the electrons in cyclotron paths (red lines) through the main spectrometer. The blue lines represent the electric potential (qE), that acts on the longitudinal component of the kinetic energy of the electrons. Only electrons with longitudinal energies $E_{\|} > q \cdot U_0$ pass the spectrometer. The transversal component of the momentum vector of the electrons decreases towards the analyzing plane (orange dotted line), the point of the lowest magnetic field (B_{min}). With 6 T, the maximum magnetic field is reached at the right solenoid. The maximum transversal component of the electron momentum vector is reached at this point. Figure from [Wan13]

and B_{max} the maximum magnetic field the electrons are exposed to, during their way from the source to the detector. ΔE denotes the energy width of the MAC-E filter and is the minimum surplus energy an electron needs to have, to pass the MAC-E filter and get to the detector.
The response function $R(E, qU)$ results from an i-fold convolution of the energy loss function with the probability of the scattering processes P_i (where i denotes the number of scattering processes for a single electron) multiplied with the transmission function $T(E, qU)$. Hence, the response function is

$$R(E, qU) = P_0 \cdot T(E, qU) + P_1 \cdot T(E, qU) \otimes f(\epsilon) + P_2 \cdot T(E, qU) \otimes [f(\epsilon) \otimes f(\epsilon)] + ... \tag{2.9}$$

With the MAC-E filter, KARIN measures the integrated tritium β-decay spectrum, when N_{tot} is the total number of tritium molecules in the source

$$N_{\mathrm{s}}(N_0, q, U_0, E_0, m_\nu^2) = N_{\mathrm{tot}} \cdot t_{\mathrm{qU}} \int_{qU_0}^{E_0} \frac{dN}{dE}(E_0, m_\nu^2) \cdot R(E, qU_0) dE. \tag{2.10}$$

Most of the KATRIN background comes from Poisson distributed events with the decay rate Γ. With the measuring time t_{qU} at a specific reading potential U, the number of background decays is given by

$$N_{\mathrm{b}}(qU) = \Gamma \cdot t_{\mathrm{qU}}. \tag{2.11}$$

The total rate of events, splits up in a background and a signal fraction, weighed by the parameters R_s and R_b. The total rate at the detector is

$$N_{\mathrm{theo}}(N_0, q, U_0, E_0, m_\nu^2, R_{\mathrm{s}}, R_{\mathrm{b}}) = R_{\mathrm{s}} \cdot N_{\mathrm{s}}(N_0, q, U_0, E_0, m_\nu^2) + R_{\mathrm{b}} \cdot N_{\mathrm{b}}(qU). \tag{2.12}$$

The theoretical spectrum is compared to a measured spectrum using a χ^2 function

$$\chi^2(R_{\mathrm{s}}, R_{\mathrm{b}}, E_0, m_\nu^2) = \sum_i \left(\frac{N_{\mathrm{meas}}(qU_i) - N_{\mathrm{theo}} R_{\mathrm{s}}, R_{\mathrm{b}}, E_0, m_\nu^2, qU_i)}{\sigma_{\mathrm{theo}}(U_i)} \right)^2, \tag{2.13}$$

where $\sigma_{\mathrm{theo}} = \sqrt{N_{\mathrm{s}} + N_{\mathrm{b}}}$ denotes the theoretical uncertainties of the signal and background rate.
By minimizing the difference in the measured and the calculated spectrum, the free parameters R_{b}, R_{s}, E_0 and most importantly m_ν^2, are obtained. With the design parameters of the KATRIN experiment [KAT05], the neutrino mass can be limited to

$$m_\nu < 200 \text{ meV (90\% C.L.)}, \tag{2.14}$$

or determined with a significance of 5σ to

$$m_\nu = 350 \text{ meV}. \tag{2.15}$$

2.2. The Main Components of the KATRIN Experiment

The following chapter will give an overview of the main components of the KATRIN experiment. A more detailed discussion on the components can be found in the official KATRIN design report [KAT05].
Figure 2.4 shows an overview of the experimental setup. KATRIN splits up in four major sections. The source section, where the tritium β-decay takes place, consist of the **W**indowless **G**aseous **T**ritium **S**ource (WGTS) and the rear section. This component is followed by the transport section, consisting of the **D**ifferential **P**umping **S**ection (DPS) and the **C**ryogenic **P**umping **S**ection (CPS), where the electrons and the tritium are separated. The pre- and main spectrometer represent the spectrometer section, where the electrons are filtered by the MAC-E high-pass filter. Finally, the transmitted electrons are detected with a focal plane detector.

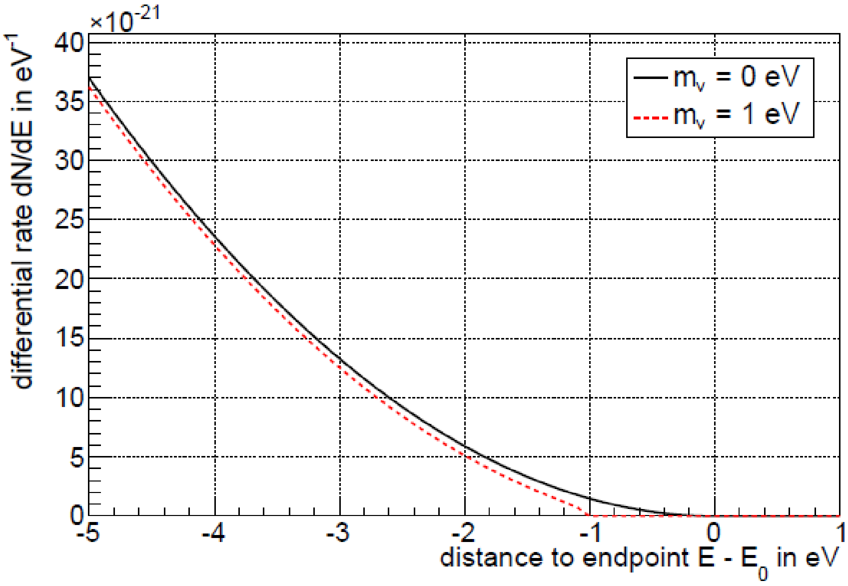

(a)

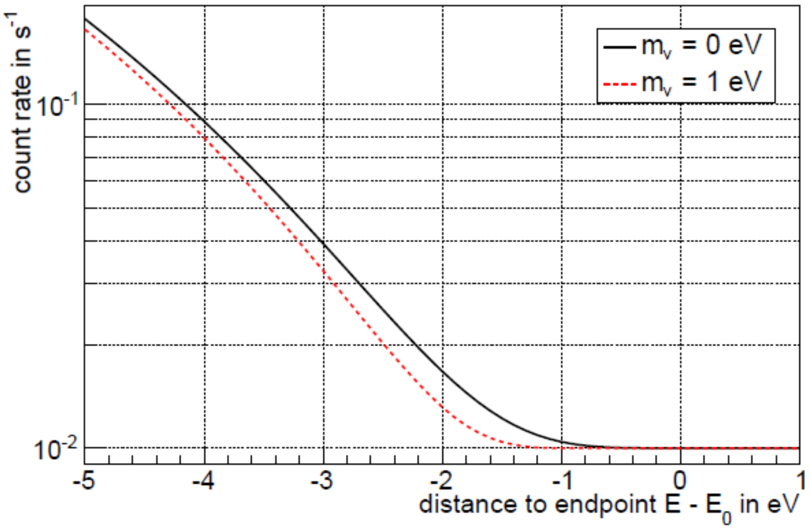

(b)

Figure 2.3.: An differential (a) and an integrated (b) β-decay spectrum. The black line is the spectrum with the neutrino mass set to zero, the dashed line with $m_\nu = 1$ eV. The endpoint of the spectrum is shifted to lower energies, depending on m_ν. Figure from [Gro15].

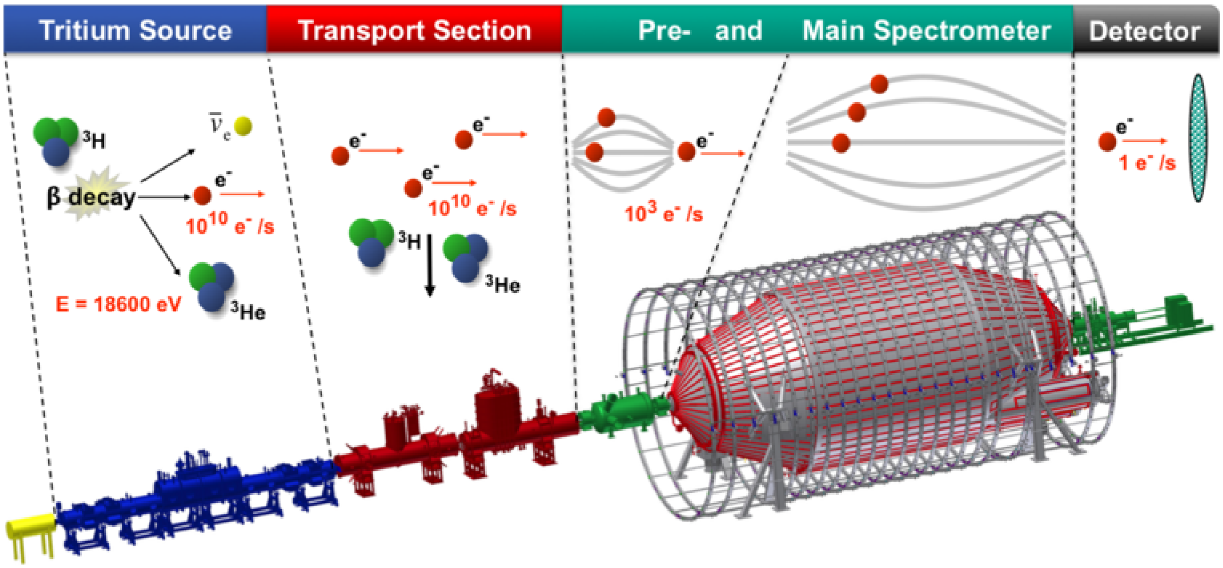

Figure 2.4.: The KATRIN experiment and its four main sections. The tritium source, where gaseous tritium decays in a β-decay to helium, the transport section, where the helium and tritium molecules are separated from the signal electrons, the pre- and main spectrometer with the high precision MAC-E filter system and finally the focal plane detector that counts the electrons, which passed the spectrometer. Figure from: http://katrin.kit.edu.

The Source Section

The source section of the KATRIN experiment consists of the WGTS and the rear section and is the component, where the tritium β-decay takes place.

The tritium gas is pumped into the WGTS at the middle of the tube. Six turbomolecular pumps at both ends of the WGTS pump out the gas, reduce the tritium gas flow by a factor of 10^2 and reinject it again. Each tritium molecule decays into a helium molecule (THe), an electron and an electron anti-neutrino. The electrons are isotropically generated with kinetic energies of $0 < E < E_0 - m_\nu^2$, and polar angles of $0 < \theta < 2\pi$.

The temperature of the source is kept at 27 K, with fluctuations of only a few mK. This assures a stable column density of the tritium gas, and minimizes the thermal Doppler broadening of the electron energies, caused by molecular motion of the tritium gas. A novel two-phase liquid neon thermosiphon cooling system, archives small temperature fluctuations of only $\Delta T = 30$ mK, which stabilizes the column densitiy by a factor of 10^{-3}. The magnetic guidance from the source to the transport section is provided by a 3.6 T solenoid.

In KATRIN, only a small fraction of electrons are created in the region-of-interest. For example, only 10^{-13} of the total electrons are created within 1 eV from the endpoint. Only those electrons are transmitted through the main spectrometer and reach the detector. The remaining electrons end at the rear section of the experiment, where they emit X-rays. The radiation is measured by the BIXS system (**B**eta **I**nduced **X**-ray **S**pectrum), and will be used to monitor the tritium activity in the source [Röl11]. Furthermore, the rear section provides an electron gun, that is used to monitor the column density in predefined intervals [Hug10].

The Transport Section

To reach the high statistical sensitivity of the KATRIN experiment, a tritium activity of $\lambda_{\mathrm{d}} \approx 10^{11}$ decays per second is crucial. Therefore, the WGTS contains of 10^{19} tritium molecules.
To reduce energy losses due to scattering processes, the spectrometer requires an ultra high vacuum of lower than 10^{-11} mbar, with a partial pressure of tritium of the order of 10^{-20} mbar [Mer12]. This is necessary to minimize tritium β-decays within the volume of the spectrometer. Hence, the tritium flow must be extensively reduced (by 12 orders of magnitude) by the transport section. To do so, two pumping sections are required: the cryogenic pumping section (CPS) and the differential pumping section (DPS).
Another challenging requirement of the transport section, is to assured an adiabatic transport of the signal electrons from the WGTS to the spectrometer, which is provided by the 12 solenoids of the transport section.

The first component of the transport section is the DPS. It consists of four turbo molecular pumps (TMPs) with a tritium pumping speed of 2000 l/s. It reduces the tritium flow of 4-5 orders of magnitude [Jan15]. The pumps are situated between five solenoids with a magnetic field of 5.5 T, which assures the transport of the signal electrons to the spectrometer section. Solenoids are arranged in a way, that the beam tube is split in five separate tubes, tilted by 20°. The ions are blocked at the junctions of the different beam tube sections, using positive potentials.

The CPS consists of seven separate beam tubes, tilted by 15°, to increase the probability for the remaining tritium molecules to hit the wall of the CPS. The inner surface of the CPS is covered with argon frost (30 K). The tritium molecules are absorbed by the argon, signal electrons are guided by the 5.6 T magnetic field of the seven solenoids. This cryo-sorption technique, will reduce the tritium flux of another 7 orders of magnitude.
Figure 2.5 shows a technical drawing of the two components, that build up the transport section. Further information of the transport section can be found at [Kos12]. A detailed discussion on the DPS can be found in [Luk12], and on the CPS in [Gil10].

The Spectrometer Section

After the signal electrons pass the transport section, they reach the spectrometer section. The system consists of two separate spectrometers, the pre- and the main spectrometer. A third, the monitor spectrometer, is a separated component and is used to monitor the high voltage stability of the main spectrometer vessel[2].

[2]The monitor spectrometer is set to the same potential as the main spectrometer and measures a K-32 conversion with the same MAC-E filter principle. The width of the conversion line reveals high voltage drifts, even at the ppm level [Erh12].

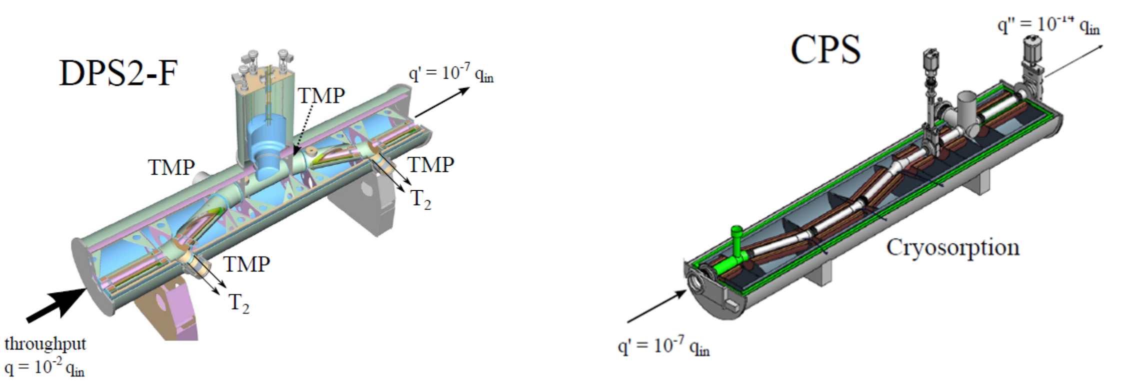

(a) (b)

Figure 2.5.: The two components from the transport section, the differential puming section (a) and the cryogenic pumping section (b). The gas flow q is reduced by a factor of 10^{12}. While the DPS pumps out the tritium molecules (TMP), the CPS uses cryosorption, to reduce the gas flow. Because of the tilted beam tubes, another part of the tritium molecules are held up by scattering with the inner layer of the components. Figure from [Höt12].

The task of the spectrometer section is to transmit the high energy electrons (near the endpoint region) and reflect the electrons with less kinetic energy.
The pre-spectrometer operates as a pre-filter system to the main spectrometer. Its potential will be set a few hundred eV below the endpoint energy, and therefore most of the electrons with kinetic energies far below the endpoint are filtered out, before they can reach the sensitive main spectrometer. With a length of 3.4 m and a diameter of 1.7 m, the pre-spectrometer was extensively used as a test experiment previous to measurements at the main spectrometer. Investigations however showed, that the main and pre-spectrometer retarding potentials U_{MS}, U_{PS}, in superposition with the magnetic field of the 4.5 T solenoid of the pre-spectrometer, cause a Penning trap[3]. One option to avoid this Penning trap is to operate the pre-spectrometer at zero filter energy qU_{PS} [Pra12]. On the one hand, lowering the filter potential eliminates the Penning trap background, but on the other hand, more signal electrons would reach the main spectrometer and could cause an increase of the spectrometer background. The optimal setting will be determined by test measurements with the two systems.

With a length of 23.3 m and a diameter of 10 m, the main spectrometer is currently the largest spectrometer vessel ever built. The length of the main spectrometer is crucial to provide a slow retarding magnetic field and respectively an adiabatic motion of the

[3] In a Penning trap charged particles can be stored by a certain superposition of an static electric and magnetic field. The magnetic field forced the particle to move in cyclotron paths and thus prevent the particles from leaving the trap radially. The electric field confines the particle axially. The cyclotron frequency is mass dependent. Most of today's high-precision mass measurements of charged particles, come from Penning trap measurements. At KATRIN however, Penning traps are a background causing effect.

Figure 2.6.: The main spectrometer vessel of the KATRIN experiment. The transport section and pre-spectrometer is not installed at the picture. The air coil system surrounds the vessel, and compensates the earth's magnetic field, and slightly increases the magnetic field at the analyzing plane. Picture from http://katrin.kit.edu.

electrons. The huge radius is a consequence of the conserved magnetic flux

$$\Phi = \int_A \vec{B} \cdot d\vec{A} = \text{const.} \tag{2.16}$$

With a design value of $\Phi = 191$ Tcm^2, the low magnetic field at the analyzing plane of $B_\text{a} = 3 \cdot 10^{-4}$ T causes a radius of $r = 4.5$ m.
The main spectrometer is the major component of the MAC-E filter system. To provide the necessary retarding field, the spectrometer vessel is set to a potential U_{MS}.
A 4.5 T solenoid at the entrance and a 6 T solenoid at the back end, provide the magnetic guidance through the spectrometer section. Furthermore, an air coil system of 15 air coils surround the vessel and compensate the non negligible earth's magnetic field ($B_\text{hor} = 20.6 \cdot 10^{-6}$ T and $B_\text{vert} = 43.6 \cdot 10^{-6}$ T). Additionally, it increases the magnetic field in the analyzing plane from $B_\text{a} = 1.79 \cdot 10^{-4}$ T, generated by the two solenoids, to the design value of $B_\text{a} = 3 \cdot 10^{-4}$ T[4].
To reduce the energy loss of signal electrons due to scattering processes, and to minimize the background signal caused by ionization of residual gas, the spectrometer section is operate in an ultra high vacuum (UHV) with a pressure of 10^{-11} mbar. This UHV is achieved by several turbomolecular (TMP) and non evaporable getter (NEG) pumps.

The Focal Plane Detector System

Electrons that passed the spectrometer, are magnetically guided by the 6 T pinch magnet and the 3.6 T detector magnet to the focal plane detector (FPD). The 148 pixel silicon

[4]Without enhancing the magnetic field at the analyzing plane, a too high flux tube radius of $r = 11$ m would be reached, according to equation 2.16.

based PIN-Diode detector is surrounded by a copper and lead shield. Additionally, an active veto system (plastic scintillators) reduces background signals, coming from cosmic rays [Har12]. The monolithic silicon wafer of 9 mm diameter and an effective thickness of 500 μm, counts the signal electrons with an energy resolution of $\Delta E = 1.637 \pm 0.004$ keV [Har12]. This resolution is sufficient for KATRIN, as the energy resolution is provided by the spectrometer section, and the detector only counts the electrons.
The multi-pixel detector is able to resolve the position (radius and azimuth angle) of the measured electron, which allows a good discrimination of background events, and a distinct analysis of the electrons passing the spectrometer at different radii.

2.3. Search for keV-Scale Sterile Neutrinos with the KATRIN Experiment

As introduced in chapter 1.5, keV-scale sterile neutrinos could be a significant fraction of dark matter. It is possible to extend the physics reach of KATRIN to measure the influence of a keV-scale sterile neutrino on the β-decay electron spectrum. The mixing of a sterile and an active neutrino spectrum

$$\frac{d\Gamma}{dE} = \cos^2\theta \frac{d\Gamma}{dE}(m_{\text{light}}) + \sin^2\theta \frac{d\Gamma}{dE}(m_{\text{s}}) \tag{2.17}$$

would be visible in a kink-like signature (see figure 2.7).
There are several significant modifications to the normal KATRIN measurement mode, which have to be taken into account, to search for keV-scale sterile neutrinos. The end-point is no longer the only region-of-interest of the β-decay spectrum. The signature of a sterile neutrino can occur anywhere in the β-spectrum. Therefore, the region-of-interest is extended to cover the entire phase space of tritium β-decay. Consequently, new challenges arise at the source, spectrometer and detector section.
First of all, source scattering plays a major role when considering the entire β-spectrum. Now, in contrast to the normal KATRIN measuring mode, electrons, which lose energy due to scattering, will still reach the detector. This means, that an extremely good understanding of the source is needed, in order to precisely model the measured spectrum.
In order to allow all β-decay electrons to reach the detector, the spectrometer section is set to very low or zero retarding potential. However, electrons with energies well above the retarding potential (i.e. high surplus energy electrons), show non-adiabatic trajectories in the main spectrometer, which in turn would cause a change of the transmission probability. This work focuses on the transmission property of the main spectrometer at low retarding potential.
Finally, the signal electron rate at the detector would be increased by 12 orders of magnitude. The FPD however, is not designed for such high rates. A new detector system needs to be developed. To optimize the detector design, detailed systematic studies concerning detector backscattering, charge sharing, pile-up, non-linearities and energy resolution are necessary. In order to characterize a new detector system with respect to high rates an adequate calibration system is needed. In this work, a high-intensity electron gun was commissioned and characterized with an Faraday cup detector.

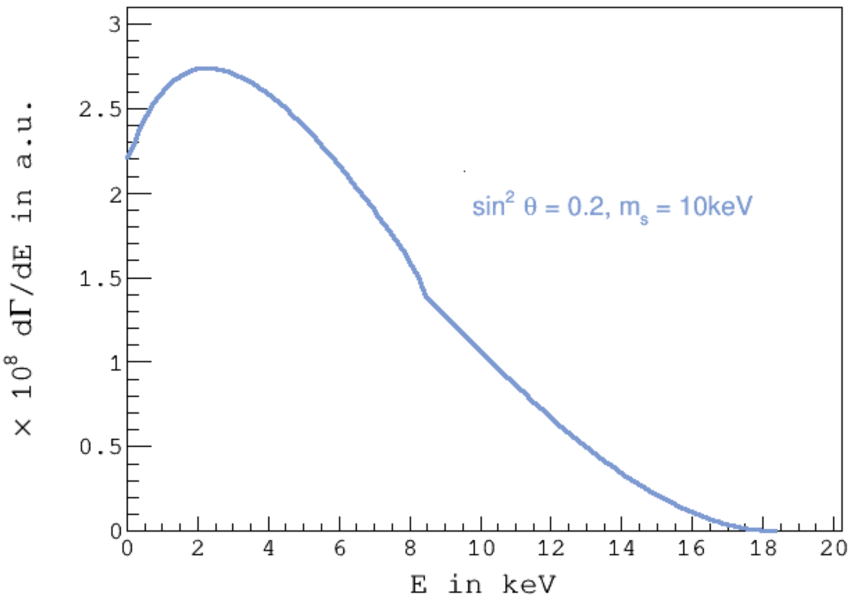

Figure 2.7.: A differential tritium β-decay electron spectrum with active-sterile neutrino mixing of $\sin^2\theta = 0.2$ with a sterile neutrino mass of $m_\mathrm{s} = 10$ keV. The imprint of the sterile neutrino is a kink-like signature, appearing at $E_\mathrm{kink} = E_0 - m_\mathrm{s}$. The rate exceeds the capability of the KATRIN focal plane detector system.

3. Sensitvity of a KATRIN-like Experiment to Sterile Neutrinos

In this chapter the sensitivity of a KATRIN-like experiment to keV-scale sterile neutrinos is investigated. Different measurement modes and systematic effects will be discussed. At the end of this chapter the new sub-project of the KATRIN collaboration TRISTAN (**TR**itium beta decay **I**nvestigation on **S**terile **T**o **A**ctive **N**eutrino mixing) will be introduced. The goal of TRISTAN is the extension of KATRIN's physics reach from measuring the neutrino mass in the sub-eV range, to searching for sterile neutrinos in the keV mass range.

Tritium β-decay is advantageous when looking for sterile neutrinos, since with an endpoint of $E_0 \approx 18.6$ keV, a mass range of 0 to E_0 is accessible. The main advantage of KATRIN with respect to a keV-scale sterile neutrino search, is its unprecedented source luminosity. The short half-life of only 12.32 years allows for high luminosity at low source densities. With a count rate of $\lambda_\mathrm{r} \approx 10^{10}$ a total statistic of $N \approx 10^{18}$ can be reached after 3 years of measuring time.

Measurement Modes

Several different measurement modes were developed and reviewed under the aspect of feasibility and the reachable sensitivity. Figure 3.2 shows an overview of the three different measuring methods.

Methode A: In an integrated measurement the count rate at different retarding potentials of the main spectrometer will be measured. When looking for keV-scale sterile neutrinos, the region-of-interest is extended to cover the entire phase space of the tritium β-decay. Accordingly, the counting rates will be 12 orders of magnitude higher than in the normal KATRIN operation mode. Two possible paths can be considered: a measurement with a novel detector system and a measurement at a reduced source strength.
For an integrated measurement, the energy resolution is given by the main spectrometer ($\Delta E = 0.93$ eV). Hence, the detector system does not have to fulfill stringent requirements with respect to energy resolution.

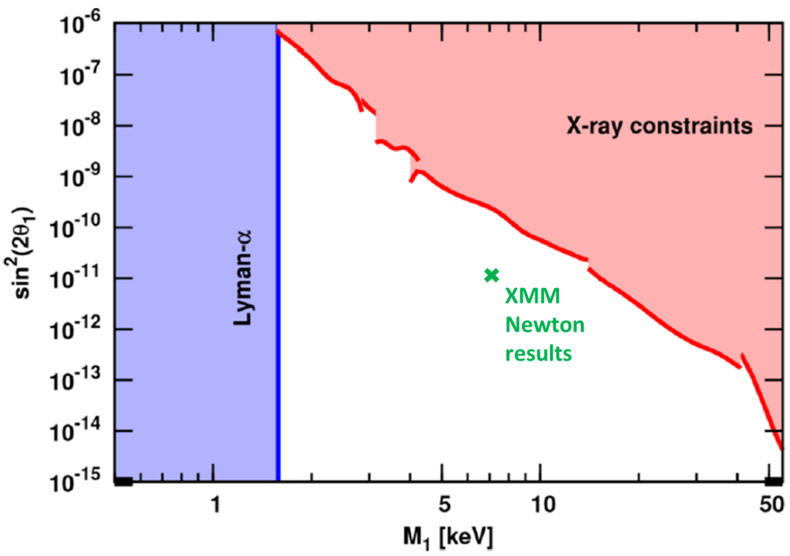

Figure 3.1.: Observing the lyman-α lines of dwarf spheroidal satellites in the Milky Way, the mass of the keV-scale sterile neutrino is limited to approximately 2 keV (blue area). X-ray constrains, coming from XMM and Chandra data, exclude the red shaded area. New results from stacked galaxy clusters X-ray observations imply an sterile neutrino with $m_s = 7.1$ keV and $\sin^2\theta = 10^{-11}$ [Bul14], [Boy14] (green marker). Figure from [Bez11].

Methode B: Another possibility is the usage of a detector system that provides energy resolution and therefore allows for a differential measurement of the tritium β-decay spectrum. To reach a high sensitivity, the new detector has to provide a sufficient energy resolution. Furthermore, it has to handle high detection rates. The requirements on such a detector system that measures the differential spectrum is much higher than on a detector system for an integrated measurement, that only counts the incoming electrons. However, due to higher rates, the sensitivity increases.
To realize a differential measurement, the retarding potential of the pre- and main spectrometer is set to zero potential, or both components are removed at all.

Methode C: In the **T**ime-**O**f-**F**light mode (TOF), the pre-spectrometer is used to sharply measure the start time of electrons entering the main spectrometer and the detector the stop time [Ste13]. Electrons with kinetic energies slightly above the retarding potential pass the detector slowly and their energy can be measured via their TOF. The TOF measurement can be a good chross-check method to a possible positive sterile neutrinos signal, as it can only measure rather small energy intervals.

3.1. Statistical Sensitivity

In this section, the statistical sensitivity on keV-scale sterile neutrinos that could be reached with a KATRIN-like experiment, is calculated. The different measuring modes of figure 3.2 are compared and the impact of theoretical uncertainties on the β-spectrum are discussed.

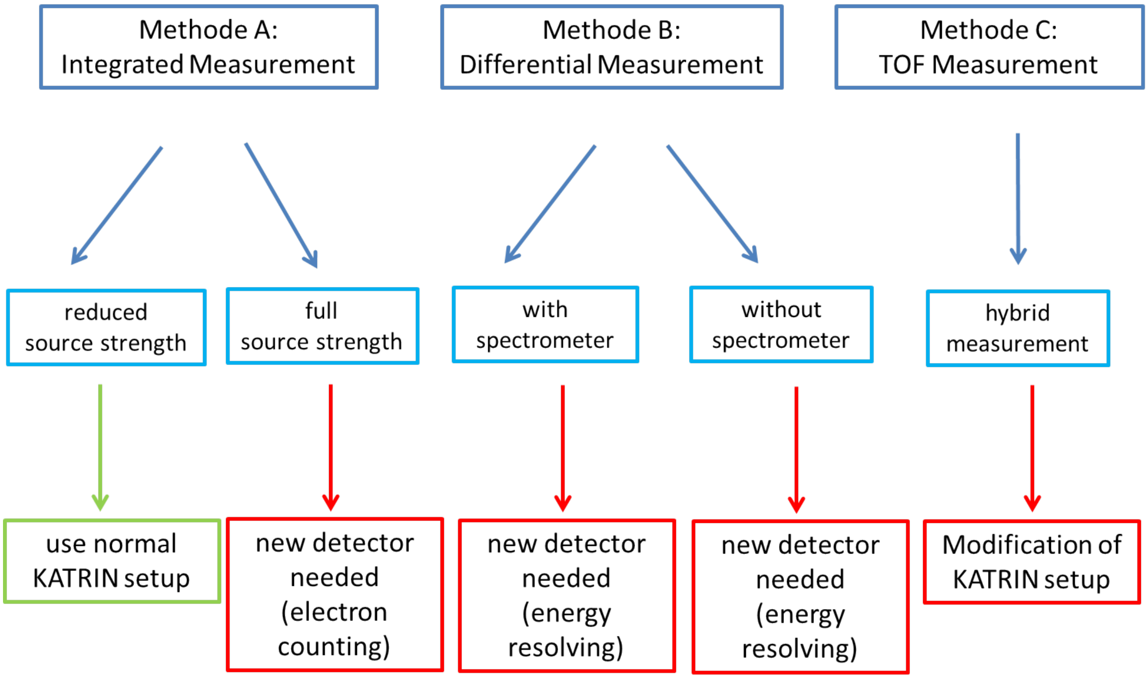

Figure 3.2.: The illustration shows the three different measuring modes. An integrated measurement with reduced source strength would be the simplest method to implement. All other measurement modes, require a new detector or at least a modification of KATRIN.

The electron detection rate D_i in an interval of E_1 and E_2 is given by

$$D_i = C_\mathrm{T} \int_{E_1}^{E_2} \frac{d\Gamma}{dE} dE, \tag{3.1}$$

with C_T a normalization constant, calculated by KATRIN related parameters (e.g. source strength and maximum acceptable angular $\theta_\mathrm{max} = 50.77°$). The exact parameters used for the β-spectrum calculations, can be found in appendix A.

Differential Spectrum

Multiplying the detection rate D_i with the measuring time of 3 years, will give the total number of counts in a given energy interval i, for a differential measurement. For the sensitivity analysis, the differential spectrum is binned in 100 bins with a bin size of 186.6 eV. Due to the high signal rate and the relatively low background rate of 0.01 electrons per second, the expected background is neglected.

Integrated Spectrum

The number of signal electrons at a specific retarding energy is calculated by integrating equation 3.1 from the energy qU_ret to the endpoint E_0 (assumed to be $E_0 = 18.575$ keV). For the analysis, 100 equally distributed retarding energies are chosen. The total measuring time of 3 years is equally divided to the 100 energy settings.

The $\Delta\chi^2$ Approach

The χ^2 function is given by

$$\chi^2 = \sum_i \left(\frac{\left(N^i_{\text{theo}} - N^i_{\text{exp}}\right)^2}{\sigma_i^2} \right), \tag{3.2}$$

with N^i_{theo} the calculated β-decay spectrum in a non-mixing scenario and N^i_{exp} the expected spectrum for an active-sterile neutrino mixing. The statistical uncertainty σ_i of each energy bin i is give by

$$\sigma_i = \sqrt{N_{\text{exp}}}. \tag{3.3}$$

The sterile neutrino parameter space ($\sin^2\theta$, m_{s}) is scanned, and the χ^2 values are calculated. The 90% exclusion limit is given by the criteria

$$\Delta\chi^2 = \chi^2 - \chi^2_{\text{min}} < 4.60. \tag{3.4}$$

Statistical Sensitivity for the different Measuring Modes

Figure 3.3 summarizes the exclusion curves for the different measuring modes. At the 90% C.L. a sensitivity of $\sin^2\theta < 10^{-7}$ can be reached at masses of $m_{\text{s}} \approx 1 - 18$ keV, and even $\sin^2\theta < 10^{-8}$ at masses of $m_{\text{s}} \approx 4 - 16$ keV, which covers an extensive part of the parameter space implied by astrophysical observations (figure 3.1.
To reduce systematic effects and to diminish the requirements for a new detector, it may be necessary to reduce the source strength. By reducing the source strength by a factor of 100, a statistical sensitivity of $\sin^2\theta < 10^{-7}$ for masses $m_{\text{s}} \approx 5 - 15$ keV, could still be reached. Considering a new approach were the source strength is increased by a factor of 100, could even lead to a sensitivity of $\sin^2\theta < 10^{-9}$ for masses $m_{\text{s}} \approx 5 - 15$ keV.
Not only from a statistical point of view, a differential mode has an advantage over an integrated measurement. As figure 3.4 shows, the active-sterile neutrino mixing leads to a sudden increase in the signal electron rate at energies of $E = E_0 - m_{\text{s}}$. An integrated measurement however, reduces this effect. It always includes all the electrons from the endpoint to the retarding potential, which reduces the effect the further m_{s} is away from the endpoint.

Conclusively the study showed, that a KATRIN-like experiment can reach a promising statistical sensitivity reaching the region of cosmological interest.

3.2. Systematic Uncertainties

A pure statistical sensitivity can just be interpreted as a potential of a KATRIN-like experiment to search for keV-scale sterile neutrinos. Systematic effects, of experimental or theoretical nature, can however decrease the sensitivity. The highest risk comes with systematic effects that would mimic a kink signature, and therefore imitate a sterile neutrino

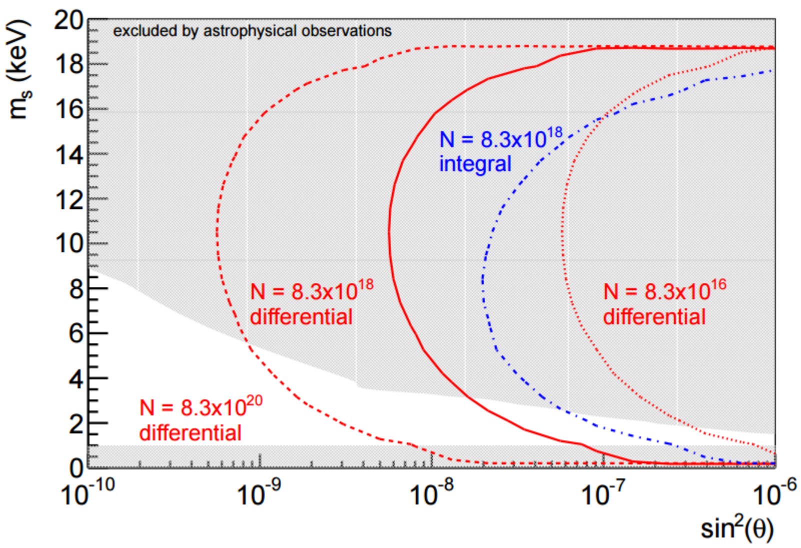

Figure 3.3.: The solid red line shows the statistical sensitivity with a differential measurement at full KATRIN source strength. At the 90% C.L. at sensitivity of $\sin^2\theta < 10^{-7}$ can be reached at masses of $m_s \approx 1 - 18$ keV and even $\sin^2\theta < 10^{-8}$ at masses of $m_s \approx 4 - 16$ keV. Reducing the source strength by a factor of 100 would lead to a slightly worse sensitivity of $\sin^2\theta < 10^{-7}$ for masses $m_s \approx 5 - 15$ keV (red dotted line). In an ideal scenario, the KATRIN source strength would be increased by a factor of 100. This would lead to an distinct increase of the statistical sensitivity up to $\sin^2\theta < 10^{-9}$ for masses $m_s \approx 5 - 16$ keV (red dashed line). The blue line shows an integrated measurement at full KARIN source strength. It can reach a sensitivity of $\sin^2\theta < 10^{-7}$ at masses of $m_s \approx 2 - 15$ keV, and has therefore a slightly disadvantage over the differential measurement. All numbers are for a generic detection efficiency of 90%. Figure from [Mer14].

signal.

This section will give a first but not complete estimation of the impact of systematic effects to the sensitivity of a KATRIN-like experiment to search for keV-scale sterile neutrinos.

3.2.1. Theoretical Uncertainties of the β-Decay Spectrum

An exact knowledge of the theoretical tritium β-decay spectrum is crucial for the sensitivity of a KATRIN-like experiment to keV-scale sterile neutrinos. The theoretical uncertainties occur at four different levels, on a molecular, atomic, nuclear and particle level. An overview of all theoretical corrections taken into account, can be found in appendix B. Most of these corrections are only calculated for energies close to the endpoint E_0 or are no relevant corrections in the normal KATRIN measurement mode.

To investigate the effect of theoretical uncertainties of the β-decay spectrum to the sensitivity of KATRIN, the correction terms are parametrized with the parameters α_j. Fitting the β-spectrum, the new parameters are left as free nuisance parameters[1]. The free parameters can now mimic a kink like signature to the shape of the spectrum and therefore alter the sensitivity.

[1] In statistics, a nuisance parameter represents a value which is not from interest for the result, but must be accounted for the analysis.

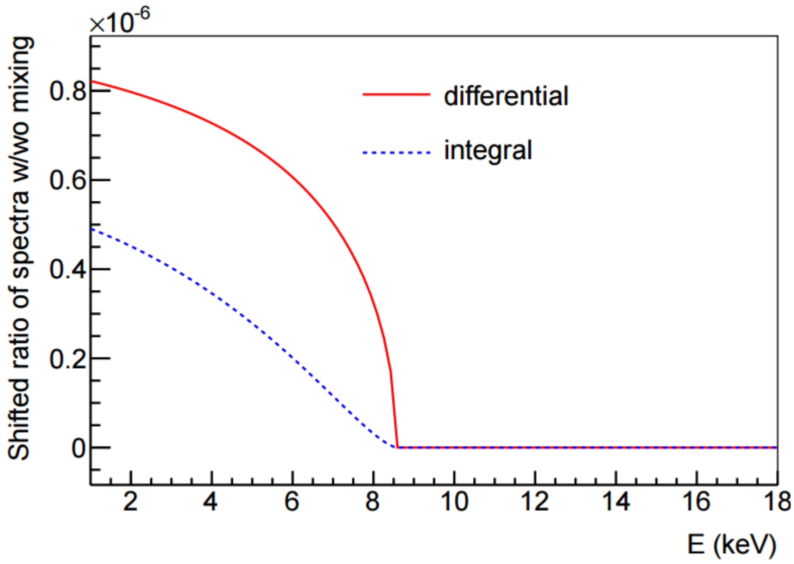

Figure 3.4.: The figure shows the ratios of the tritium β-spectra of an active-sterile neutrino mixing (with $\sin^2 = 10^{-6}$ and $m_\mathrm{s} = 10$ keV) and a non-mixing case. The blue dashed line represents an integrated, red a differential measurement. To provide an easier comparison, the ratios are shifted to zero above the kink. At an energy of $E = E_0 - m_\mathrm{s}$, a sudden increase of the ratio is visible. However, an integral measurements reduces this effect significantly. Figure from [Mer14].

To evaluate the sensitivity of a differential spectrum at a 90% C.L., the χ^2 from 3.2 changes to

$$\chi^2 = \sum_i \left(\frac{(N^i_\mathrm{theo} - N^i_\mathrm{exp}(\alpha_j))}{\sigma_i^2} \right) + \sum_j \left(\frac{\alpha_j^\mathrm{bestfit} - \alpha^\mathrm{true}}{\sigma_j} \right)^2 , \tag{3.5}$$

with $\alpha_j^\mathrm{bestfit}$ the fitted and α^true the true nuisance parameter.
The exclusion curve of figure 3.5 is obtained, by performing a χ^2-fit at each point of the sterile-neutrino parameter space of $(\sin^2\theta,\ m_\mathrm{s})$. It shows, that the final sensitivity is reduced by a factor of 5, due to theoretical uncertainties.

3.2.2. Experimental Uncertainties of the β-Decay Spectrum

Beside theoretical uncertainties, there are numerous experimental uncertainties that have to be taken into account, to predict a realistic sensitivity of KATRIN to search for keV-scale sterile neutrinos. This section introduces a number of systematic uncertainties of the KATRIN experiment and their influence to the sensitivity. They can be sorted by the section of KATRIN where they occur.

Source Section: Electron Scattering in the WGTS and Backscattering at the Rear Wall

The high tritium density implies high scattering probabilities for the signal electrons

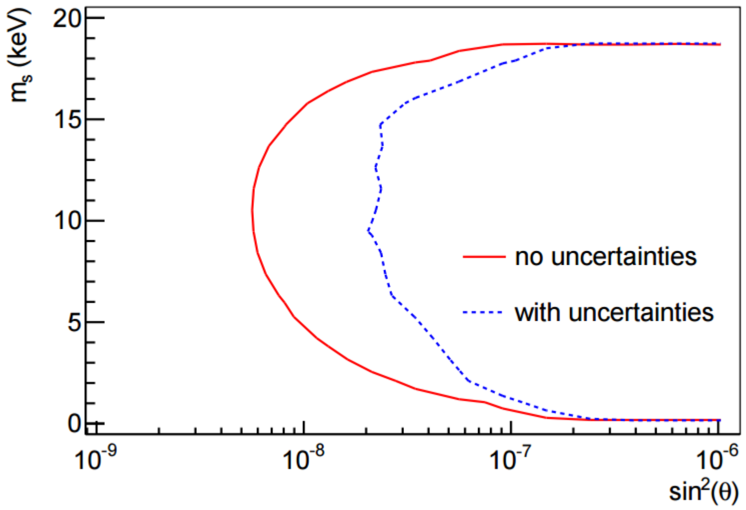

Figure 3.5.: The spectral fit approach showed, that theoretical uncertainties can reduce the total sensitivity by a factor of 5. Figure from [Mer14].

[Ase00]. The electrons lose energy due to elastic scattering, ionization or excitation with the gaseous tritium in the source. The energy loss causes a shape distortion of the β-spectrum.

A second challenge constitutes the backscattering of β-electrons, at the gold surface of the rear wall of the WGTS [Käf12]. In the normal KATRIN mode, the β-electrons induce X-rays and therefore offer a possibility to monitor the source activity of KATRIN. The energy loss due to the backscattering process is less of a problem in this case, since the retarding potential can not longer be passed by the backscattered electrons. For sterile neutrino search however, the backscattered electrons can reach the detector, since the retarding potential of the main spectrometer is set to very low or zero potential.

The reduction of the source strength would partly decrease the effects. However, as pointed out at figure 3.3, a reduction of the source strength lowers the statistical sensitivity. One way to minimize the effect of β-electrons scattering at the rear wall gold surface is, to place the rear wall in an low magnetic field. Due to magnetic reflection, the electrons are prevent from scattering back into the source. For the keV-scale sterile neutrino search, a further investigation of these energy-dependent uncertainties is of crucial importance.

Main Spectrometer: Non-Adiabatic Electron Transportation

For keV-scale sterile neutrino search, the entire β-decay spectrum is of interest. Therefore, the main spectrometer is operated at very low or zero potential and the signal electrons have a surplus energy of $E_{\mathrm{sur}} = E_0 - qU_{\mathrm{ret}}$. Due to the low magnetic field in the analyzing plane of the spectrometer the motion of the electrons in the main spectrometer is non-adiabatic, which leads to change of the transmission probability of the main spectrometer. To guarantee a fully adiabatic transport through the spectrometer, the magnetic field at

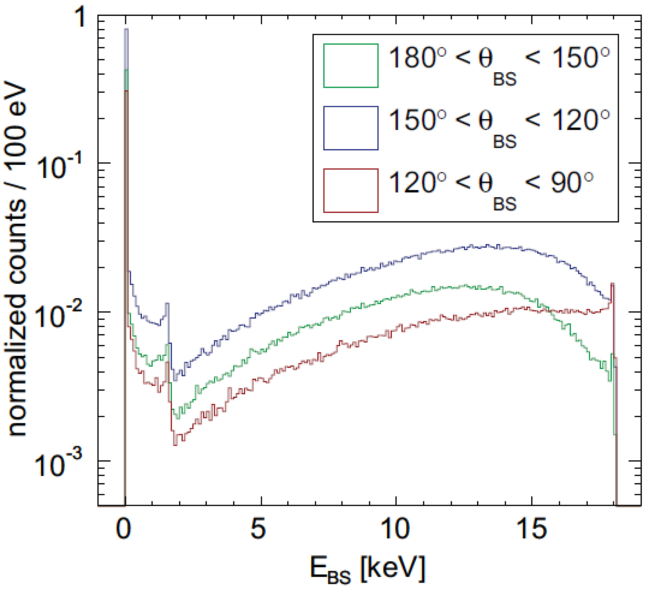

Figure 3.6.: The energy spectrum of backscattered electrons. The primary electron had an initial energy of $E_{\text{ini}} = 18$ keV and a initial polar angle of $\theta_{\text{ini}} = 0°$. The energy loss of the electron varies from 0 to 18 keV. With the retarding potential of the main spectrometer set to zero, the backscattered electrons can enter the spectrometer again. Figure from [Ren11].

the analyzing plane has to be increased. In chapter 4, the effect of non-adiabatic electron transportation is discussed in detail.

Detector: Electron Backscattering at the Detector

Electrons with an energy of $E = 18$ keV and an polar angle of $\theta = 0°$, have a 20% probability to be backscattered at the focal plane detector of KATRIN [Ren11]. The electrons deposit a part of their energy in the detector. Figure 3.6 shows an energy spectrum of backscattered electrons. At the normal KATRIN mode, the retarding potential of the main spectrometer is set close to the endpoint. Due to the energy loss at the backscattering process, the electrons are reflected at the potential of the main spectrometer or are magnetically mirrored and fly back to the detector and get detected. The traveling time of these electrons are only a few ns which is far below the μs shaping time of the detector [Ren11]. Therefore, the electron backscattering at the normal KATRIN mode is negligible.

However, electrons with high surplus energies, which backscatter with a small energy loss in the detector, might neither be reflected magnetically nor by the retarding potential. This effect again leads to a change of the shape of the β-decay spectrum and needs to be investigated in detail.

Covariance Matrix Approach

One way to study experimental systematic effects is via the covariance matrix approach as shown in [Mer14]. This method takes into account the correlation of uncertainties over

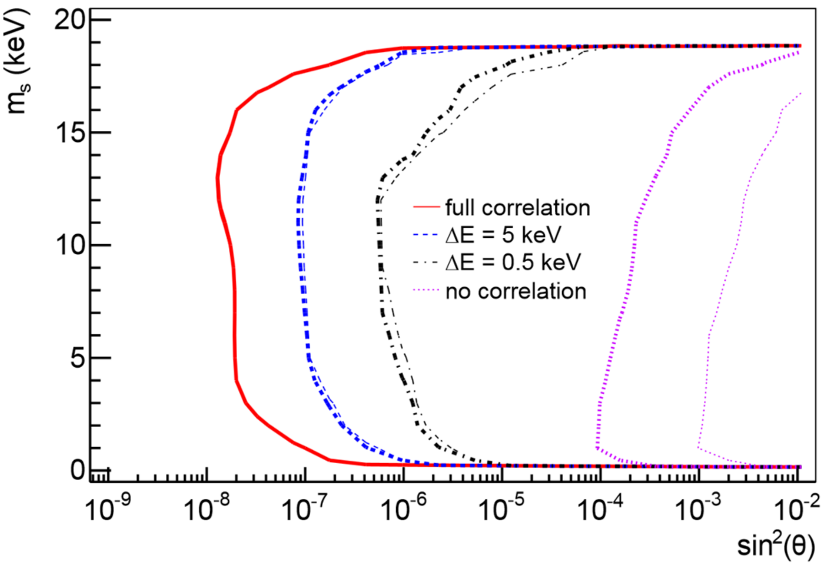

Figure 3.7.: Exclusion curves for different correlation lengths ΔE and different values of the uncertainties ρ. The thin lines are for an assumed uncertainty of $\rho = 0.5\%$, the tick lines for $\rho = 0.05\%$. Uncorrelated errors decrease the sensitivity drastically. Correlated uncertainties also reduce the statistical sensitivity, but strongly depending on their correlation length. Figure from [Mer14].

a certain energy range ΔE. The exclusion curve is obtained, by computing the modified χ^2 function

$$\chi^2 = \sum_{ij} \Upsilon_i \left(N^i_{\text{theo}} - N^i_{\text{exp}}(\alpha_k)\right) V^{-1}_{ij} \left(N^j_{\text{theo}} - N^j_{\text{exp}}(\alpha_k)\right) \Upsilon_j + \sum_k \left(\frac{\alpha_k^{\text{bestfit}} - \alpha^{\text{true}}}{\sigma_k}\right)^2 \tag{3.6}$$

at every grid point of the $(\sin^2\theta, m_\text{s})$ parameter space.

A generic study in [Mer14] showed that uncorrelated uncertainties have a strong influence on the reachable sensitivity. However, uncertainties which are correlated with correlation lengths $\Delta E > 0.5$ keV, do not reduce the sensitivity as much, since they do not allow to mimic the kink-like signature of a sterile neutrino, see figure 3.7.

3.3. The TRISTAN Sub-Project of the KATRIN Experiment

The goal of TRISTAN (**TR**itium beta decay **I**nvestigation on **S**terile **T**o **A**ctive **N**eutrino mixing) is to realize a sterile neutrino search with KATRIN. A major challenge comes with the fact, that with the full source strength, the count rate over the entire tritium spectrum will be 12 orders of magnitude higher than in normal KATRIN mode. Therefore, a staged approached, starting with a measuring at reduced source strength, followed by a measurement with an upgraded KATRIN detector system, is pursuit.

The main goals of the new detector system are the capability to handle high rates, while at the same time provide a high energy resolution. The main design features of the new detector will be very small point contacts which allow to measure high rates, while minimizing noise. In Addition, a thin entrance window is needed, that allows the detection of low energy electrons. Finally, a shared steering electrode will enable a pixel size of up to 2 mm, which allows a large surface area of the detector, while keeping the number of pixels at a technically feasible number[2].

Another main challenge will be an adequate read-out system and a control of the systematic effects at the ppm level [Mer15]. A first prototype detector, to both optimize detector and read-out system will be produced at the Halbleiter Labor in Munich (HLL), this year.

[2] As an example, with a rate of 400 kHz per pixel, a total number of 10^4 pixels are needed to measure the complete signal electron rate of the high luminous KATRIN source.

4. Adiabatic Transport of High Surplus Energy Electrons in the KATRIN Main Spectrometer

As shown in chapter 3, KATRIN provides a promising potential to search for keV-scale sterile neutrinos in an astrophysical favored parameter region. However, systematic uncertainties can decrease the sensitivity significantly. In section 3.2.2, a number of experimental systematic effects such as electron scattering in the source or non-adiabatic transportation of electrons with energies well above the retarding potential (i.e. surplus energy) through the main spectrometer, were introduced. This chapter focuses on a detailed study of the latter effect. It is ascertained, that an adiabatic transport of electrons with high surplus energies can be achieved by a change of the electromagnetic design of the main spectrometer, using the large volume air coil.
The investigations are based on a detailed study of the transmission probability of the KATRIN main spectrometer, using the simulation framework KASPER.

4.1. Motivation

For the normal KATRIN mode it is crucial to precisely know the transmission probability of electrons through the main spectrometer. Accordingly, an adiabatic guidance of the signal electrons through the main spectrometer (i.e. a completely reversible motion) is of high importance. Several studies have shown, that in normal KATRIN mode, a fully adiabatic electron transport is provided from the source to the detector [Gro15], [Wan13].

If KATRIN is used to search for keV-scale sterile neutrinos, a high precision measurement of the entire tritium β-decay spectrum is necessary and hence, the retarding potential of the main spectrometer has to be set to very low or zero potential. As a consequence, the electrons have high surplus energies with respect to the retarding potential of the main spectrometer. With the normal KATRIN electromagnetic design, these electrons show a non-adiabatic behavior, which ends up in a change of the transmission probability.

This work studies the non-adiabatic behavior and proposes an approach to eliminate the effect.

4.2. Adiabatic Electron Transport

Due to the Lorentz force

$$\vec{F} = q(\vec{E} + \vec{v} \times \vec{B}), \tag{4.1}$$

the electrons that enter the main spectrometer follow the guiding magnetic field lines in helix-like trajectories caused by the cyclotron motion. As the magnetic field decreases towards the analyzing plane, the polar angular θ of the electrons decreases and respectively the longitudinal energy increases, which is crucial for a precise measurement of the total kinetic energy of the electrons. After the electron passed the analyzing plane, the magnetic field increases towards the pinch solenoid magnet. If the initial polar angle of the electron is bigger than

$$\theta > \sin^{-1}\left(\sqrt{\frac{B_{\text{PS}}}{B_{\text{PCH}}}}\right) \tag{4.2}$$

the electron gets magnetically reflected at the pinch magnet. However, this is only valid if the change of the magnetic and electric field

$$\frac{\Delta B}{B} << \quad \text{and} \quad \frac{\Delta E}{E} << 1 \tag{4.3}$$

is small within one cyclotron length

$$l_{\text{cyc}} = 2\pi \frac{\gamma \cdot m_e}{e \cdot B} \cdot v_{\|}, \tag{4.4}$$

where m_e denotes the electron mass, γ the relativistic factor, e the electron charge and $v_{\|}$ the electrons transversal velocity [Leh64]. If this condition is fulfilled, the motion is adiabatic. To first order, the adiabatic invariant is the orbital magnetic moment

$$\gamma\mu = \frac{\gamma + 1}{2\gamma} \cdot \frac{E_{\perp}}{B} \tag{4.5}$$

(in this case $E_{\perp} = E_{\text{kin}} \cdot \sin^2\theta$ denotes the transversal kinetic energy of the electron and not the electric field in the main spectrometer as in equation 4.3), which in non-relativistic[1] approximation can be approximated with

$$\mu \approx \frac{E_{\perp}}{B}. \tag{4.6}$$

Figure 4.1 shows that the orbital magnetic moment oscillates significantly in the region of low magnetic fields inside the main spectrometer. The reason is, that the real adiabatic invariant I_{ad} is not the orbital magnetic moment, but a complex function of higher field

[1]For tritium β-decay electrons $\gamma < 1.04$

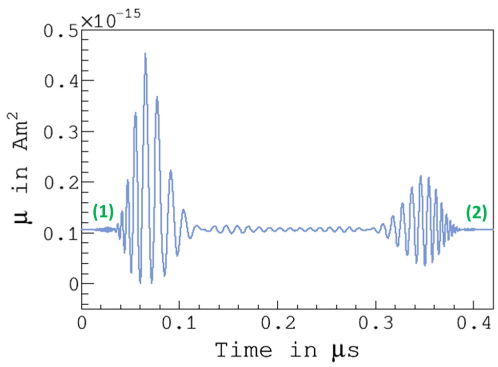

(a)

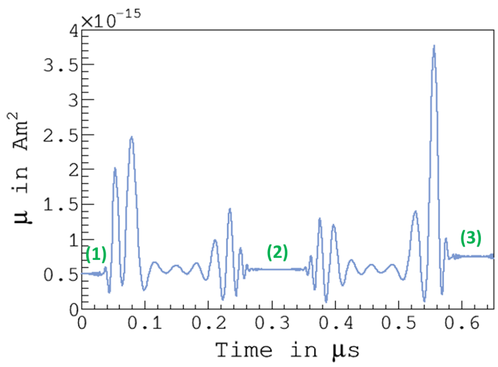

(b)

Figure 4.1.: The orbital magnetic moment μ of an electron with $E_{\text{sur}} = 1$ keV that passed the spectrometer (a) and of a trapped electron with $E_{\text{sur}} = 20$ keV (b) as a function of its time of propagation. The points (1) and (2) mark the entrance and exit of the main spectrometer. The reflected electron (b) reverses at the exit of the main spectrometer due to a magnetically refection at the pinch magnet. At (3) it gets reflected again at the pre-spectrometer magnet. The electron is trapped.

derivatives [Nor63], [Cle69]. Consequently, μ varies in the small magnetic field regions. But inside regions of homogeneous magnetic fields (close to the pre-spectrometer and pinch magnet), the field derivatives are small and the approximation

$$I_{\text{ad}} \approx \mu \tag{4.7}$$

is valid.

By considering μ only in these regions, the adiabaticity can still be tested without calculating the full adiabatic invariant I_{ad}.

An example for an adiabatic transportation can be seen at (a) of figure 4.1. The value of μ at the entrance (1) and the exit (2) of the main spectrometer is equal, even if μ shows large oscillations between the two points.

Figure 4.1 (b) shows an example of an electron with high surplus energy and non-adiabatic behavior. The value of μ is slightly higher at the exit point of the main spectrometer (2). As a consequence, the polar angle of the electron changes to a higher value, which leads to a magnetic reflection back inside the spectrometer. At the initial starting position, the orbital magnetic moment μ has again increased, which leads to another magnetic reflection. The electron is now trapped in the main spectrometer.

Chaotic Electron Transport at non-adiabatic Conditions

Non-adiabatic transport conditions at high surplus electron energies E_{sur} lead to a drastic change of the transmission property of the main spectrometer as shown in figure 4.2.

Due to a variation of the adiabatic invariant I_{ad}, the motion of the electrons become chaotic. According to the chaos theory, a system is chaotic if a small change of the starting condition, ends up in a large variation of the trajectories [Gla93].

One way to test the chaotic behavior of the electrons at non-adiabatic transport conditions,

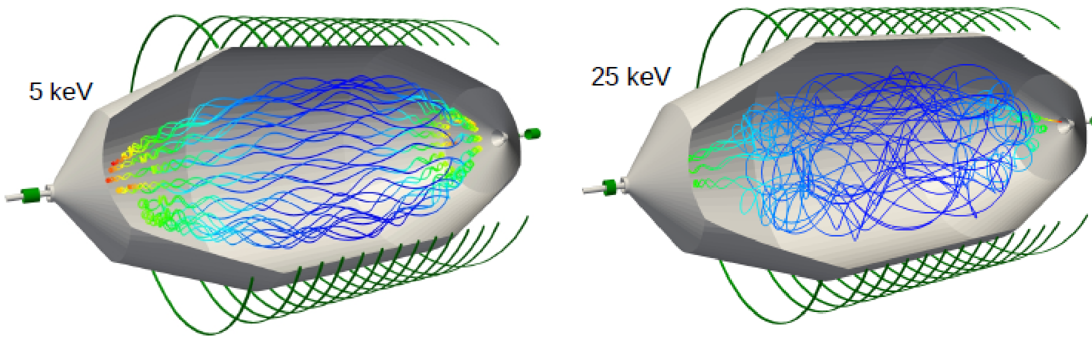

(a) (b)

Figure 4.2.: The trajectories of stored electrons. Electrons with a surplus energy of $E_{\mathrm{sur}} = 5$ keV (a) show already non-adiabatic behavior however, the turning points due to magnetic reflection are almost at the same z-position. At high surplus energies of $E_{\mathrm{sur}} = 25$ keV (b), the trajectories are chaotic with many different reflection points, caused by a chaotic change of the polar angular θ. Illustration from [Wan13].

is to change the starting condition by only 10^{-14} m and and to compare the trajectories as a function of the propagation time. In an adiabatic and respectively non-chaotic process, the distance of the two trajectories should scale linearly in time, due to numerical errors accumulated in the calculation [Wan13]. Non-adiabatic motion would cause a fast and exponentially increase of the distance.

Figure 4.3 shows an example of an adiabatic transport of an electrons with low surplus energy of $E_{\mathrm{sur}} = 100$ eV (a) and an electron with high surplus energy of $E_{\mathrm{sur}} = 15$ keV (b). The latter shows a fast exponential rise of the distance of the trajectories (10 m after a few ms) as predicted by the chaos-theory. The electrons with only 100 eV surplus energy behave ordinary with a linear rise of the distance of the trajectories in time. Furthermore it is shown, that the degree of chaotic motion and respectively non-adiabaticity, strongly depends on the strength of the magnetic field and the electron's kinetic energy inside the main spectrometer [Wan13].

If KATRIN is used to search for keV-scale sterile neutrinos, the latter effect is unpreventable. However, an increase of the magnetic field strength inside the main spectrometer has the potential to eliminate non-adiabatic transportation. In the following the hardware components responsible for the electric and magnetic fields in the KATRIN main spectrometer will be reviewed.

4.3. The electromagnetic Design of the KATRIN Main Spectrometer

To reduce spectrometer related background and ensure well known transmission properties, the electromagnetic design of the main spectrometer has to meet distinct requirements. These goals are reached by a combination of several different electric and magnetic components, which are introduced in the following section.

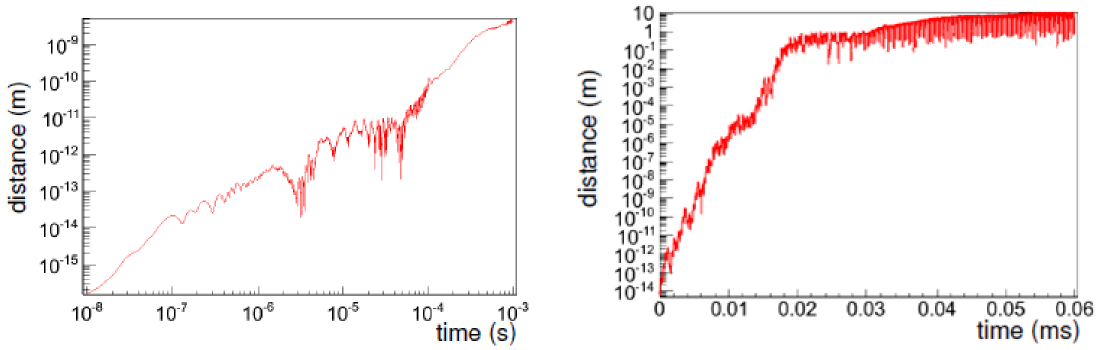

(a) (b)

Figure 4.3.: The distance between two electron trajectories, started with a small change of the starting position, is a good test to chaotic motion. Low surplus energies (a) behave normal, while electrons with high surplus energies (b) lead to a fast and exponential increase of the trajectory distance. This behavior strongly indicates a chaotic and therefore non-adiabatic transportation of high surplus energy electrons through the main spectrometer. Simulations and figure from [Wan13].

The superconducting Solenoids

To provide magnetic guidance of the signal electrons from the tritium source to the detector, numerous superconducting solenoids are operated at KATRIN. The superposition of the magnets stray fields, generate the signal electron beam tube with a magnetic flux of 191 Tcm^2. The radius of the beam at different positions is depending on the strength of the magnetic field and can be calculated due to the conservation of the magnetic flux

$$\Phi = \int_{\mathrm{A}} \vec{B} \cdot d\vec{A} = \text{const.} \tag{4.8}$$

The radius of the magnetic flux tube is given by

$$r = \sqrt{\frac{\Phi}{B \cdot \pi}} \; . \tag{4.9}$$

The Vessel Electrode and the Inner Wire Electrode System

The electrostatic potential which is necessary to analyze the longitudinal electron energy in the analyzing plane, is generated by the vessel electrode of the KATRIN main spectrometer. The electric field is not generated by segmented electrodes, but by setting the vessel itself on high voltage.

Furthermore, an inner wire electrode system is implemented in the main spectrometer which fulfills primarily two tasks. First, the fine shaping of the electric field and second, an electrostatic shielding against background from the vessel wall.

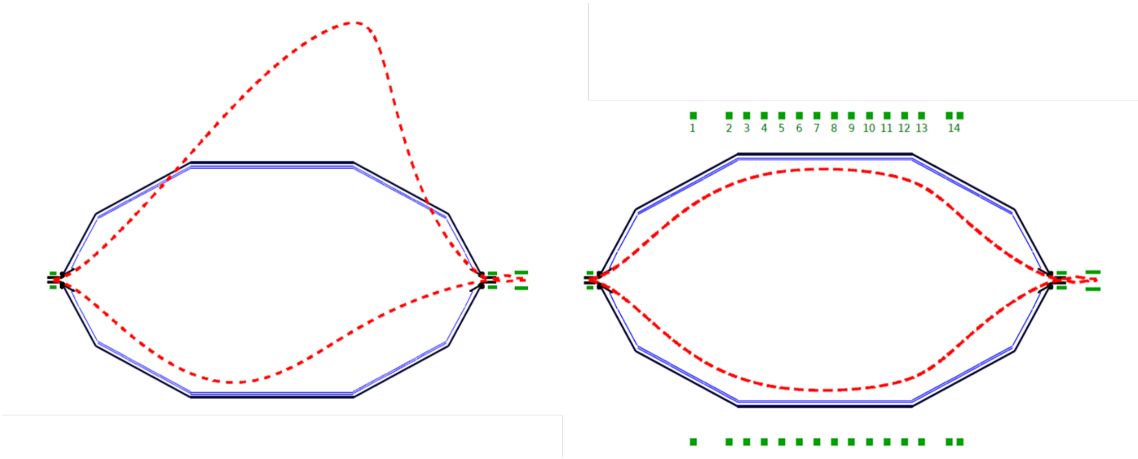

Figure 4.4.: Because of the earths magnetic field, the magnetic flux through the main spectrometer is of unsymmetrical shape (a). As a consequence, the signal electrons hit the surface of the main spectrometer vessel and cause an increase of the background and a decrease of the statistics. However, the large volume air coil system is able to compensate these effects (b). Illustration from [Wan13].

The large Volume Air Coil System

Additionally to the solenoids, the magnetic field inside the main spectrometer is generated by 15 large volume Helmholz air coils that surround the main spectrometer. It consists of two sub-components. The earth magnetic field compensation system (EMCS) and the low field correction system (LFCS). The task of the EMCS is to compensate the inhomogenities of the magnetic field inside the main spectrometer, caused by the earth's magnetic field. The LFCS enhances the magnetic field strength and thus compresses the radius of the flux tube in order to reduce the loss of statistics and suppress background electrons which originate from directly connecting the beam tube to the vessel wall. Figure 4.4 illustrates the effect of the air coil system to the magnetic flux tube.

4.4. The Simulation Framework KASPER

To study the non-adiabatic transportation of high surplus energy electrons through the main spectrometer, the simulation framework KASPER, which was developed for and by the KATRIN collaboration, was used. By combining several different simulation modules, it is able to simulate the behavior of charged particles in any component of KATRIN. The following three modules are of relevance for the simulations, performed in the scope of this thesis:

KGeoBag: This module consists of different geometric elements, which are combined to build the KATRIN components, that are of interest for the simulations. In this work, it was used to construct the geometry of the main spectrometer. It is furthermore used for field calculations and particle navigation through the geometric object.

KEMField: To calculate the complex electromagnetic fields at KATRIN, several field solving algorithms are necessary. The KEMField module contains these algorithms [Glü11].

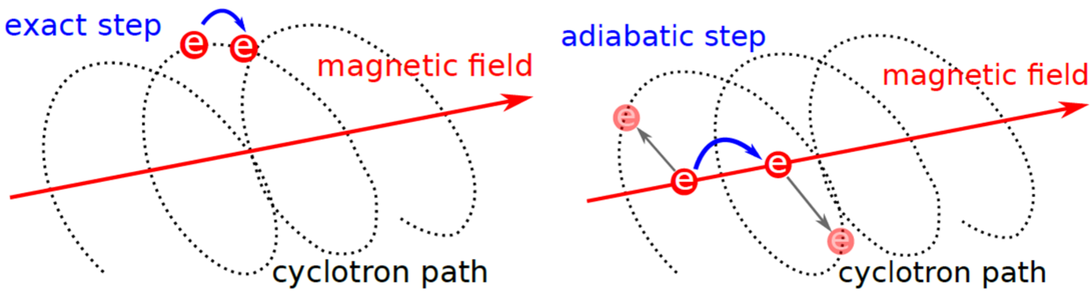

Figure 4.5.: The simulation module to track charged particles in electromagnetic fields, KASSIOPEIA, is provided with two different tracking options. The software is able to track the exact trajectory of a particle with stepsizes corresponding to different fractions of the cyclotron length. However, an exact tracking is time-consuming. If the magnetic and electric fields are almost constant, the tracking can be reduced to a so-called adiabatic tracking. In this case, only the steps along the magnetic guiding field are calculated. The different steps in the cyclotron path are reconstructed. Illustration from [Wan13].

KASSIOPEIA: The particle tracking is done by the KASSIOPEIA module. The tracking allows different degrees of accuracy as illustrated in figure 4.5. The simulation module KASSIOPEIA provides the option of different particle tracking algorithms. Depending on the task, the electron trajectory can be tracked with different accuracy. Figure 4.5 shows an overview of the two different tracking algorithms. KASSIOPEIA is able to track the exact trajectory by using stepsizes of different fractions of the cyclotron length. This is necessary for all simulations, where adiabatic transportation is not assured.
If the particle propagates in a fully adiabatic motion, than the so-called adiabatic tracking, where only the steps along the magnetic guidance line are calculated, is sufficient.
For this study, an exact tracking with a fraction of 1/16 of the cyclotron length was chosen.

Configuration: KASPER provides an user friendly XML interface, that allows a systematic setup of the simulation configuration file. Appendix D shows the configuration file of the simulations, used for this chapter. It also gives a more detailed insight of the structure of XML configuration files and the used modules.

4.5. Simulation Settings

For every simulation a total number of 10^5 electrons was generated at the entrance of the main spectrometer. The starting parameters of the electrons, the setting of the electromagnetic components and the termination conditions are described in this section.

Initial Position $\vec{r}_{\mathrm{ini}}$

The electrons were generated in the middle of the pre-spectrometer magnet (PS). According to equation 4.9, the magnetic flux tube inside the PS magnet has a radius of

$$r_{\mathrm{flux}} = \sqrt{\frac{\Phi}{B_{\mathrm{PS}} \cdot \pi}} = 3.67 \text{ cm}, \tag{4.10}$$

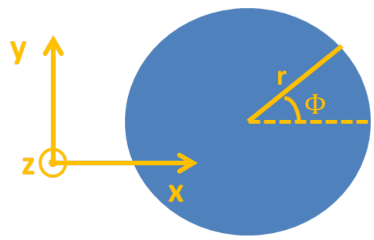

Figure 4.6.: In KASPER simulations, polar coordinates are used to describe the position of the particles, with r the radius and φ the azimuth angle.

with the magnetic flux $\Phi = 191$ Tcm^2 and a magnetic field in the pre-spectrometer solenoid of $B_{\mathrm{PS}} = 4.5$ T. The electrons x- and y-coordinates are homogeneously distributed on a disc with the radius of the flux tube $r_{\mathrm{flux}} = 3.67$ cm. In the particle tracking package KASSIOPEIA, polar coordinates are used, where r is the distance from the point in space from the symmetry axis in z-direction and φ the azimuth angle (see figure 4.6).

Initial Kinetic Energy E_{ini}

The effect of non-adiabatic electron transport strongly depends on the difference between the electron's kinetic energy E and the filter energy of the main spectrometer U_{MS}, the so-called surplus energy

$$E_{\mathrm{sur}} = E - qU_{\mathrm{MS}}. \tag{4.11}$$

Therefore, the electron's initial kinetic energies are homogeneous distributed from 0 - 20 keV to cover the full energy interval of the tritium β-decay spectrum.

Initial Polar Angle θ_{ini}

For this simulation only those electrons are relevant that would be transmitted in the case of adiabatic motion. These are electrons that start with an angle smaller then the acceptance angle θ_{max}. Since the magnetic field at the pre-spectrometer and pinch solenoids have a radial dependence, the maximal starting polar angle has a radial dependence and is given by

$$\theta_{\mathrm{max}}(r_{\mathrm{i}}, r_{\mathrm{f}}) = \sin^{-1}\left(\sqrt{\frac{B_{\mathrm{PS}}(r_{\mathrm{i}})}{B_{\mathrm{PCH}}(r_{\mathrm{f}})}}\right). \tag{4.12}$$

Because of the magnetic reflection, electrons with initial polar angles bigger than θ_{max} can not be transmitted at all (even in adiabatic case) and are not taken into account in the transmission studies. Hence, the electrons in the simulation were started with an initial polar angle of

$$\theta_{\mathrm{ini}} \leq \theta_{\mathrm{max}}(r_{\mathrm{i}}, r_{\mathrm{f}}). \tag{4.13}$$

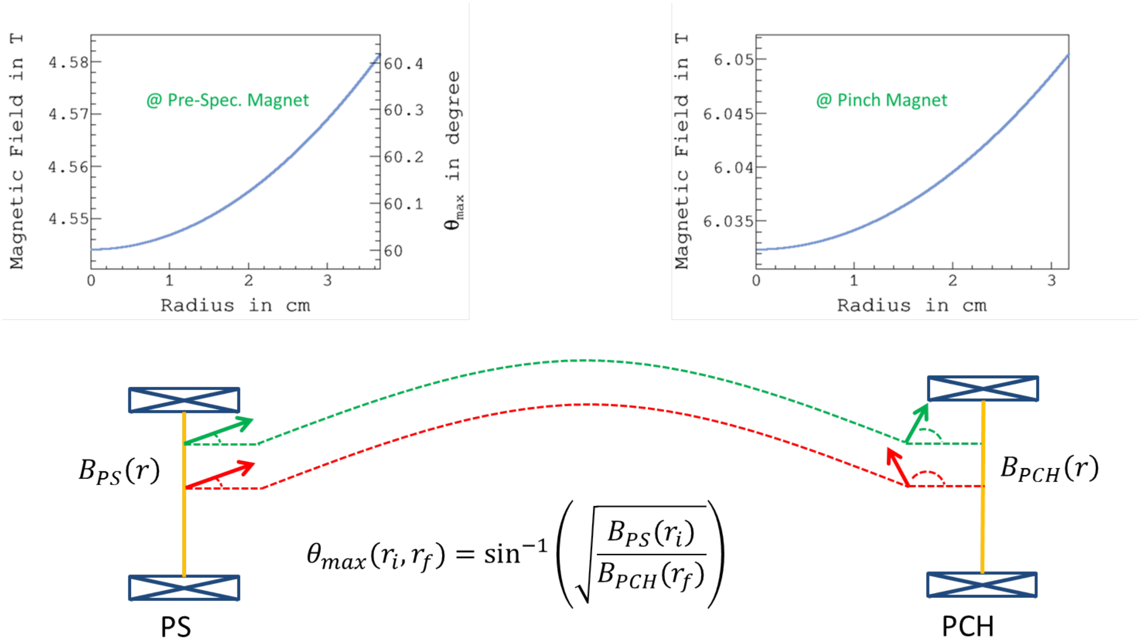

Figure 4.7.: The magnetic field in the pre-spectrometer magnet (PS) and the pinch magnet on the detector side (PCH) as a function of the radii of the electrons. As a consequence, the maximal polar angle under which an electron can enter the main spectrometer without getting magnetically reflected, varies with the starting radius. The transmission probability for two electrons with the same initial polar angle θ_{ini} can therefore differ, depending on their exact starting position. Because of the azimuthal drift of the electrons in the main spectrometer, the initial and final radius varies for the different electron initial settings. Hence, the calculation of the θ_{max} (equation 4.12) uses a variable initial magnetic field and the maximal final magnetic field as a constant.

Setting of the Main Spectrometer

In order to study the most non-adiabatic scenario, all electrodes of the main spectrometer are set to a retarding potential $U_{\text{ret}} = 0$ kV.
The influence of the large volume air coil system to the (non-)adiabaticity is the main goal of this study. Therefore, the current of the 15 coils was varied to determine the required magnetic field strength for an adiabatic transport.

The Terminators

The entire evolution process of a particle, from its generation to its termination, is pooled together to one particle track. The track consists of the initial and final properties of the particle. The point of termination is determined by several terminator conditions. In this study, three different terminator were used:

1. **Terminator transmitted:** If particles passed the spectrometer and reached a z-position of z = 12.5 m, then the particle has been transmitted through the main spectrometer and is stopped.
2. **Terminator reflected:** If the particle gets reflected at the pinch magnet due to non-adiabatic behavior, it can exit the main spectrometer at the pre-spectrometer

side. The terminator *reflected* counts these electrons, if they reach a z-position of z = -12.5 m.

3. **Terminator trapped:** If the reflections happens at both sides of the main spectrometer, the electron is trapped. If the electrons take more than ten turns, the terminator *trapped* terminates the electron.

The transmission probability is calculated for each energy bin i, by counting the electrons that passed the spectrometer (terminator *transmitted*) $t[i]$ and comparing it to the number of electrons which were generated in the energy bin $n[i]$

$$T[i] = \frac{t[i]}{n[i]}. \tag{4.14}$$

The error on the transmission probability is given by

$$\sigma[i] = \sqrt{\frac{(t[i]+1)(t[i]+2)}{(n[i]+2)(n[i]+3)} - \frac{(t[i]+1)^2}{(n[i]+2)^2}}, \tag{4.15}$$

according to [Ull08].

4.6. Results and Conclusion

Figure 4.8 shows the transmission probability as a function of the surplus energy E_{sur} of the electrons. As expected, the transmission for electrons with high surplus energy distinctly decreases for surplus energies above a few keV, as a consequence of non-adiabatic motion. More specifically, this means that the polar angle varies chaotically and the electrons are more likely to be reflected at the high magnetic field at the pinch magnet. Hence, with increasing surplus energy, the probability for an electron to leave the spectrometer at the pre-spectrometer side or to get trapped in the main spectrometer increases, which results in a deficit of the transmitted electrons.

If the magnetic field inside the main spectrometer is increased, by enhancing the turns of the surrounding air coil system by a certain factor (turnfactor), the non-adiabatic effects reduce significantly. Figure 4.9 shows the transmission probability for turnfactors of the air coil system from 1.0 to 3.0. The figure shows, that the adiabatic transport can be restored for higher magnetic fields.

Figure 4.10 and figure 4.11 show the transmission probability for electrons with $E_{\mathrm{sur}} = 20$ keV (the ones that show the most non-adiabatic motion) as a function of the turnfactor of the air coil system. It is shown, that a turnfactor of at minimum 4.0 is necessary to reach a full adiabatic transportation, and therefore a transmission probability of 100%.

Summing up, the investigation showed, that an fully adiabatic transport for electrons with high surplus energies form 0 to 20 keV can be assured, by increasing the magnetic field strength inside the main spectrometer by a factor of 4.0 with respect to a coil current of $I_{\mathrm{ac}} = 100$ A and a corresponding magnetic field strength in the center of the main spectrometer of $B_{\mathrm{center}} \approx 10 \cdot 10^{-4}$ T.

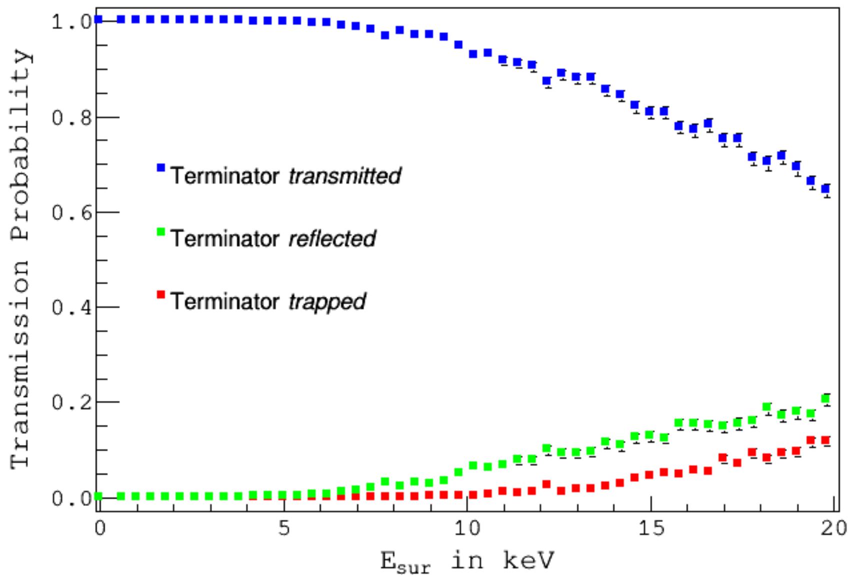

Figure 4.8.: The blue marker show the transmission probability of electrons with surplus energies E_{sur} from 0 to 20 keV. Due to non-adiabatic effects, the transmission probability decreases with an increase of E_{sur}. The green and the red marker show the terminator condition of the non-transmitted electrons. Most of the electrons get reflected at the pinch magnet and leave the spectrometer on the pre-spectrometer side (green). Others get trapped in the main spectrometer due to a chaotic change of their polar angle (red).

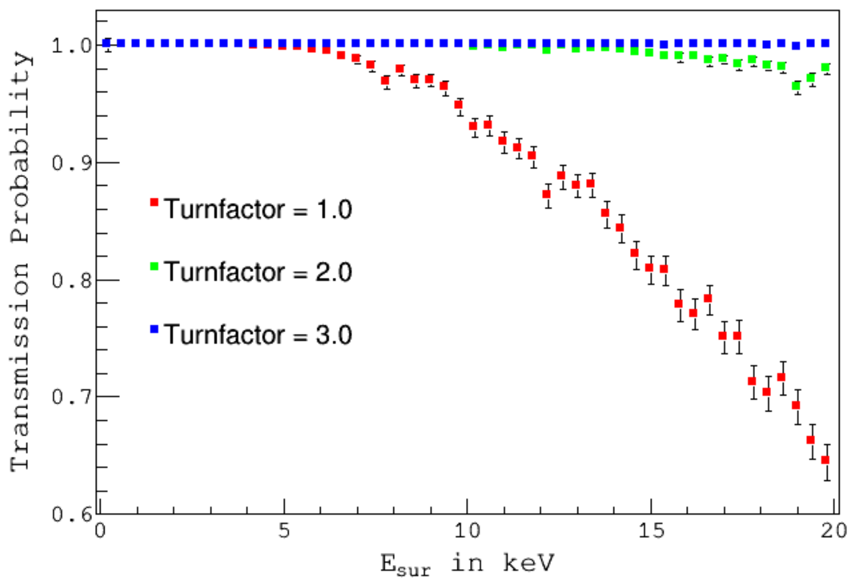

Figure 4.9.: The transmission probability as a function of the surplus energy for different turnfactors of the air coil system. With an increase of the magnetic field in the main spectrometer, the adiabaticity of the high surplus energy electrons increases and respectively their transmission probability.

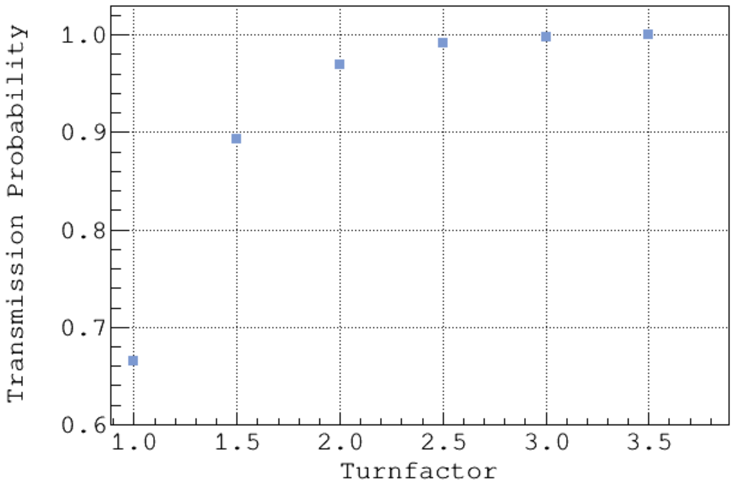

Figure 4.10.: Transmission probability of electrons with $E_{\mathrm{sur}} = 20$ keV as a function of the turnfactor of the air coil system. The transmission probability increases fast with the turnfactor. A zoom shown in figure 4.11 shows, that a turnfactor of 4.0 is needed to provide a full transmission for electrons with a surplus energy of $E_{\mathrm{sur}} = 20$ keV.

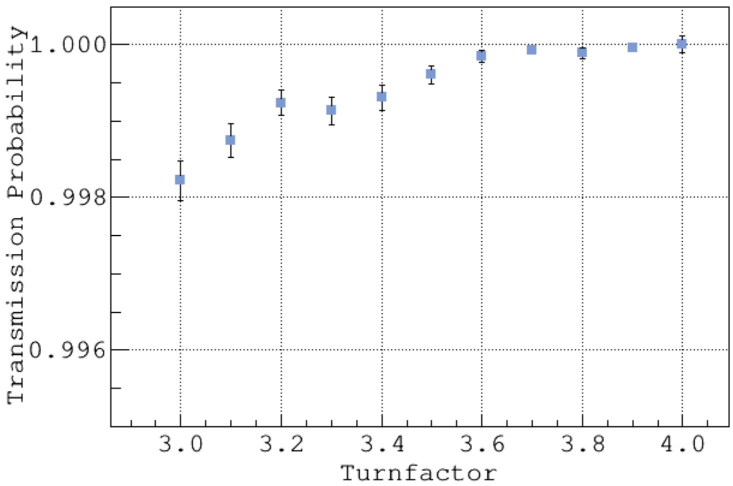

Figure 4.11.: Transmission probability of electrons with $E_{\mathrm{sur}} = 20$ keV as a function of the turnfactor on an interval from 3.0 to 4.0. The deviation is in the range of a few tenth of a percent until the full transmission is reached for a turnfactor of 4.0.

Technical Feasibility

The magnetic field strength generated by the air coil system scales linear with the coil current I_{ac} and the number of turns N_{ac}

$$B_{\mathrm{ac}} \propto I_{\mathrm{ac}}, \tag{4.16}$$

$$B_{\mathrm{ac}} \propto N_{\mathrm{ac}}. \tag{4.17}$$

To reach the intended increase of the magnetic field by a factor of 4.0, either the number

of turns or the coil current has to be increased by the same factor.
In this work, the air coil current was set to $I_{\mathrm{ac}} = 100$ A. Measurements showed, that this corresponds to an increase of the temperature of the air coils by $\Delta T_{\mathrm{ac}} = 10°$ C above room temperature [Glü15]. The temperature increases linearly with the power of the coils P_{ac}, which itself increases quadraticly with the coil current I_{ac}

$$\Delta T_{\mathrm{ac}} \propto P_{\mathrm{ac}} \propto I_{\mathrm{ac}}^2. \tag{4.18}$$

Accordingly, an increase of the air coil current by a factor of 2.0, would increase the temperature difference to approximately $\Delta T = 40°$ C, which is compatible with the present hardware. Higher temperatures would require a cooling system.

In normal KATRIN mode the four outer coils have a turn number of $N_{\mathrm{ac}} = 14$ (double layer) and the inner ten of $N_{\mathrm{ac}} = 8$ (single layer). The number of turns of the single layer coils could be increased by a factor of 2.0 without a major modification of the system [Glü15].

In a further study, it has to be investigated if the increase by a factor of 2.0 of the single layer coils and an increase of the coil current by a factor of 2.0, is sufficient to assure a fully adiabatic transport of electrons with surplus energies up to 20 keV.

5. Commissioning of a High-Intensity E-Gun

The demand for a well-calibrated electron source at KATRIN is manifold. Different test experiments at the pre-spectrometer made use of electron guns to test different phenomena and to prove the functionality of the KATRIN components [Pra12].
In context of a keV-scale sterile neutrino search with KATRIN, a new high intensity e-gun is needed, to investigate several tasks related to this topic. In this work, the EGF-3104 from Kimball Physics was commissioned, and measurements to characterize the e-gun were performed, using a Faraday cup system.

5.1. Motivation

In the following, the different calibration and test measurements that can be addressed with the e-gun will be listed. Beyond the application for sterile neutrino search, this e-gun can also be used to investigate topics related to the normal KATRIN mode.

Detector Calibration

One of the main applications for the new high-intensity e-gun, is the calibration of the novel TRISTAN detector, a prototype detector, that will be build at the Halbleiterlabor (HLL) in Munich soon. Detector parameters, for example electron backscattering, energy loss in the dead layer, pileup, dead-time, and energy nonlinearities can be determined by using the e-gun as a well-calibrated electron source.

Electron Backscattering at the Rear Wall

One of the first tasks of the new high-intensity e-gun will be the investigation of electrons, backscattering at the gold layer of the rear wall of the WGTS. In the normal KARIN mode, backscattered electrons from the rear wall are not of major concern, since due to their energy loss they can no longer pass the spectrometer and reach the detector.
For keV-scale sterile neutrino search however, the energy loss due to backscattering becomes an important experimental uncertainty. A shift of the electron spectrum to lower

energies, changes the shape of the β-spectrum and has to be investigated in detail.
A measurement with an electron source is essential to characterize the effect. In section 5.4, an experiment is introduced that aims to investigate backscattering of electrons at a thin gold surface. Electron induced X-rays are used, to monitor the intensity of the e-gun, micro channel plate detectors on the back side of the experiment will detect the rate of the backscattered electrons.

Adiabatic Electron Transport at High Surplus Electron Energies

Another main task of the new high-intensity e-gun, will be the investigation of the transmission probabilities of the main spectrometer at electron energies well above the retarding potential. Furthermore, the background at the main spectrometer at zero or low retarding potential has to be measured with a WGTS like electron rate.

WGTS Emulation

The KATRIN source has a tritium decay rate of $\lambda_\mathrm{d} \approx 10^{11}$ decays per second. The new high-intensity e-gun should be able to emulate the WGTS for future KATRIN calibration measurements, such as background behavior at full source strength at different retarding potentials or vacuum conditions at the main spectrometer.

Electron stimulated Desorption

Another interesting application for the normal KATRIN mode would be the reduction of background effects due to hydrogen atoms at the inner wall of the main spectrometer. The high-intensity e-gun could be applied to remove the background causing atoms by making use of the effect of electron stimulated desorption. A high-intensity electron beam would scan the inner wall of the main spectrometer (guided by magnetic fields). The electrons stimulate the hydrogen molecules to resolve from the inner layer of the main spectrometer. The resolved hydrogen is pumped out by the vacuum pumps and the background due to ionization of the hydrogen molecules is reduced significantly.

Plasma to emulate Tritium Ions

Important for both, the normal and sterile neutrino mode of KATRIN, is the investigation of the WGTS and the transport section. To test the tritium flow performance of the transport section, a plasma is produced in the WGTS by stimulating air ions with a high-intensity e-gun beam. The plasma propagates from the WGTS through the transport section to the main spectrometer. Using ionized air plasma instead of tritium, reduces the risk of contaminating the system with radioactive material.

5.1.1. Requirements for an E-Gun

According to the above mentioned applications, the e-gun should be able to emulate the KATRIN WGTS with respect to intensity, energy, and beam spread.

1. **Intensity:** A beam current of at least 10 nA (corresponding to approximately 10^{11} electrons per second) is required.
2. **Energy:** Electron energies should be in the tritium β-decay energy interval from 0 to 20 keV.
3. **Beam spread:** To emulate the flux tube, a wide beam divergence of the order of a few centimeters is necessary.

Based on these requirements, a decision was made for the EGF-3104 from Kimball Physics.

5.2. The Kimball EGF-3104

The Kimball EGF-3104 (**E**lectron **G**un **F**lood mode) is a compact and robust commercial electron gun, that fits all of the needed requirements. The EGF-3104 is accessed with a high stability power supply from Kimball Phyisics, which metering is assured by a flex panel digital meter on the front of the power supply and can be connected to a personal computer via a serial RS-232 interface. Figure 5.1 shows the parameters of the EGF-3104 specified by the manufacturer. A detailed data specification sheet can be found in appendix C.

The EGF-3104 produces a wide angle, non-focusable electron beam with adjustable electron energies from 0.2 - 20 keV. The e-gun consist of the following units that generate and control the electron beam.

The Ta-Cathode

The Tantalum cathode is a refractory metal thermionic emitter heated by an isolated voltage source. The free electrons are produced by the Edison-Richardson-Effect, also known as thermionic emission. By heating up metal, the thermionic energy of the electron gas increases. If the energy overcomes the work function[1] of the material, the electrons emit from the surface. The emission current density can be calculated by the Richarson-Dushmann equation

$$J(T) = A \cdot T^2 \cdot \exp\left(-\frac{W}{k_\mathrm{B} T}\right), \tag{5.1}$$

with A the Richardson constant ($A = 37\mathrm{A}/(\mathrm{cm}^2 \cdot \mathrm{K}^2)$ for Ta [Phy14]), T the temperature of the cathode, W the work function of the cathode material and k_B the Boltzmann constant [Ric05].
However, to provide high electron intensities, the temperature of the cathode reaches values of $T > 2000$ K. To reduce the risk of damage of the cathode due to high temperatures, the EGF-3104 makes use of the Schottky-Effect [Kit04]. The electron emitter is negatively biased to its surroundings. The potential difference generates an electric field F at the

[1]The work function denotes the minimal thermionic energy, which is needed to remove electrons from a solid metal, to a point outside the surface. It is given by $W = -e\varphi - E_\mathrm{F}$, with e the charge of the electron, φ the electrostatic potential and E_F the Fermi level of the material [Kit04].

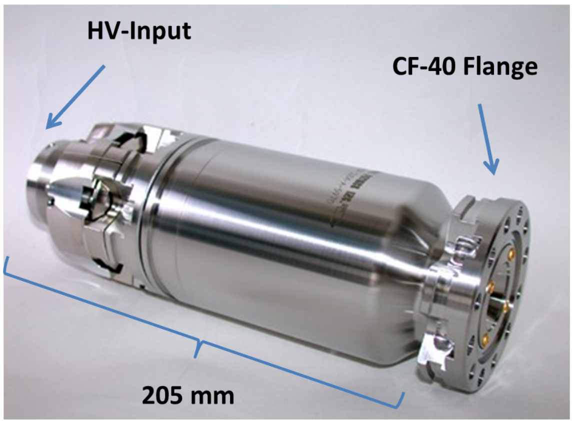

Beam Energy:	0.2 – 20 keV
Energy Stability:	±0.01% /hr, 0.02% /8 hrs
Energy Spread:	0.3 eV
Beam Current:	1 nA – 1 mA
Beam Stability:	±0.1% /hr

Figure 5.1.: The EGF-3104 from Kimball Physics, USA. It is mounted with a CF-40 flange to the vacuum system. With a total length of 205 mm and an outer diameter of 70 mm, the gun weighs approximately 12 kg. Detailed specifications by the manufacturer can be found in appendix C. Picture from http://www.kimballphysics.com.

surface of the emitter. The electric field lowers the Fermi-level of the surface and therefore decreases the work function by a value of ΔW. The emission current density is modified to

$$J(T, F) = A \cdot T^2 \cdot \exp\left(-\frac{(W - \Delta W(F))}{k_{\mathrm{B}}T}\right), \tag{5.2}$$

with

$$\Delta W(F) = \sqrt{\frac{e^3 F}{4\pi\epsilon_0}}, \tag{5.3}$$

where ϵ_0 denotes the vacuum permittivity. This allows to operate the cathode at low temperatures and therefore spares the material.

The (Wehnelt-) Control Grid

The control Grid is a cylindrical tubular, that surrounds the cathode and has an aperture at one end. The Grid potential is controlled by a voltage source. It can be set to negative values and has the function of a Wehnelt cylinder [Fle34]. As the potential of the Wehnelt is increased, the electric field F between the cylinder and the cathode increases, too. Because of the negative potential, the work function increases and the electron emission on the cathode is suppressed. If sufficient potential is applied, the Grid can completely suppress electron emission at all. Accordingly, the Grid can be used to pulse the e-gun. Furthermore, the electric field generated by the Grid, controls the beam divergence and uniformity, by influencing the electron trajectory.

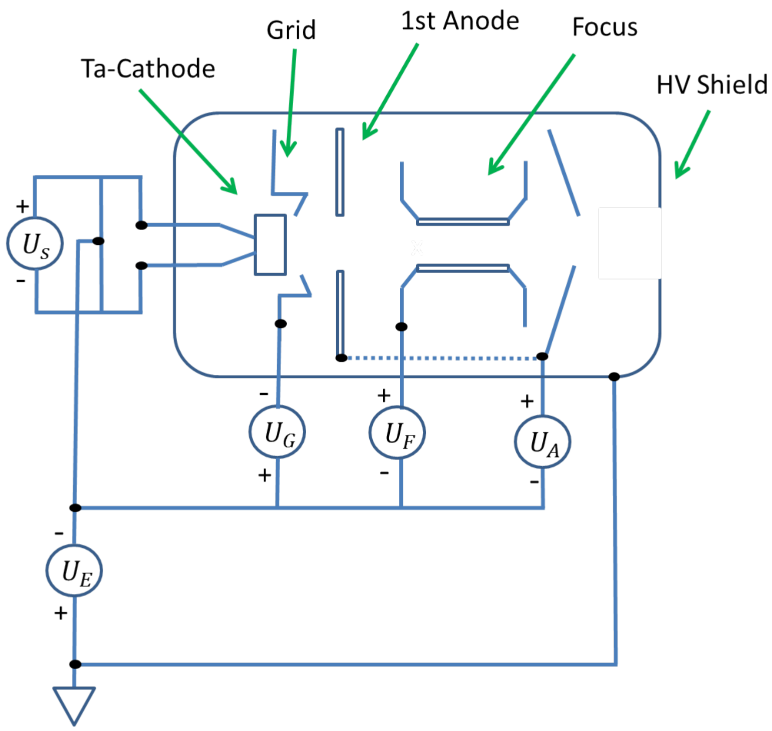

Figure 5.2.: A schematic drawing of the EGF-3104 with its main components, the Ta-Cathode, the Wehnelt Grid, the 1st Anode and the Focus. The units are surrounded by a high voltage shielding.

The Focus

The Focus is a cylindrical unit, positioned in the forward direction of the electron beam. Setting the Focus cylinder to a positive potential (referenced to the cathode), the divergence and the uniformity of the electron beam is influenced due to Coulomb forces. Hence, varying the potential of the Focus is one possibility to influence the spot size of the electron beam. However, because of the flood electron gun design of the EGF-3104, the spot size can be controlled most significantly only by varying the working distance[2] or the size of the aperture.

The 1st Anode

The 1st Anode is a spherical mesh aperture. It is set to the same potential as the high voltage pot. Increasing the 1st Anode potential makes it more positive referenced to the cathode. It can greatly influence the beam uniformity and the divergence.

Figure 5.2 shows a drawing of the inner structure of the EGF-3104 with the different voltage settings of the main components. The housing of the EGF-3104 provides a high voltage shielding of the surroundings.

[2]The working distance denotes the distance from the e-gun aperture to the detector or the target which is illuminated by the electron beam.

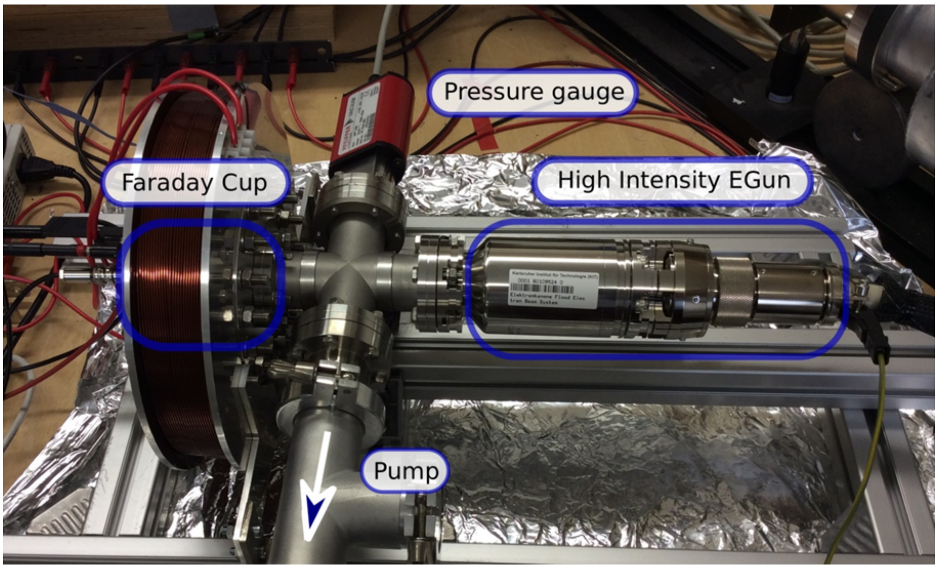

Figure 5.3.: The setup of the Faraday cup system consists of a four-way cross, connected to a pressure gauge, a turbo molecular pump, the Faraday cup detector and the high-intensity e-gun. Additionally, an air coil magnet was installed, for the purpose of investigating the influence of magnetic fields to the Faraday cup and the beam of the e-gun.

5.3. Characterization of the new High-Intensity E-gun with a Faraday Cup System

To characterize the new e-gun and to investigate the influence of the different parameters, it has been commissioned in an experimental setup (see figure 5.3) with the following components:

1. **Vacuum system:** To minimize the scattering processes of the beam electrons with residual gas, the setup is operated at a pressure of $p \approx 10^{-7}$ mbar. The vacuum is generated by a turbo molecular pump (HiCube 80 from Pfeiffer Vacuum) and monitored by a pressure gauges (HPT 200 from Pfeiffer Vacuum).
2. **Faraday cup:** Because of its simple structure and well known technology, the electrons are detected with a Faraday cup detector, which is described in detail in section 5.3.1.
3. **Read-out system:** The read-out of the detector signal is done by a picoammeter, connected to a computer via a serial interface.
4. **E-gun controller:** The EGF-3104 is controlled by its powering supply and the flex panel digital meter on the front of it.

The setup is located in an air-conditioned laboratory at a constant temperature of $T = 25°$ C.

5.3.1. The Faraday Cup Detector

A Faraday cup detector consist of a hollow stainless steal cylinder, surrounded by an outer, grounded cylinder that provides shielding. The stainless steal cylinder is electrically

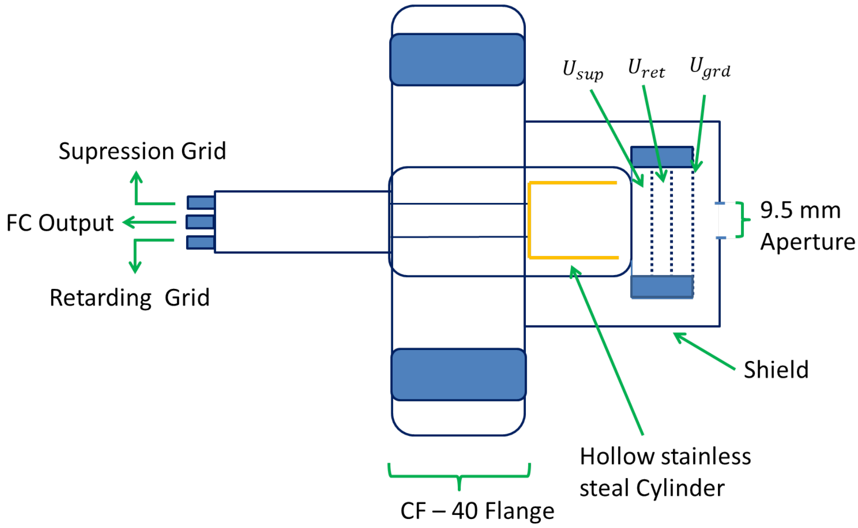

Figure 5.4.: A schematic drawing of the Faraday cup FC-37 A from Kimball Physics, with the three different grids between the Faraday cup cylinder and its aperture. On the backside, three serial outputs allow the read-out of the signal and control of the suppressing and retarding grid.

connected to a BNC-connector, which transports the collected charge through a vacuum feedthrough to an appropriate read-out electronic device.
A system of three different electrical grids, provide an energy measurement option and suppresses the secondary electron emission. The ground grid U_{grd} is attached to the aperture plate and is grounded by connecting it to the shield. The retarding grid U_{ret} can be set to a variable potential. It provides the opportunity to analyze the energy of the electrons by increasing an electric retarding field until the signal rate cuts off. The third grid is set to a potential $U_{\mathrm{sup}} = 50$ V, to reduce the effect of secondary and scattered electrons, generated by the electrons hitting the stainless steal cylinder. Furthermore, the suppression grid reduces the capaticity between the retarding grid and the Faraday cup.
In our case, the collected current is read-out with a Keithley 6487 picoammeter. According to the manufacturer, the Keithley 6487 is able to measure currents from 2 nA - 2 mA with a resolution of 10 fA. The picoammeter is connected to a personal computer via a serial RS-232 interface. The data acquisition assures a lab view macro, which writes out the time stamp and the current of the different measurements to an ASCII file.

To determine the noise signal of the Faraday cup system, a four day measurement was performed under the same conditions as the data was taken later. Figure 5.5 shows the results of the noise measurement. The measured values are Gaussian distributed around a mean value of 69.92 fA with a standard deviation of 14.19 fA. The noise of the Faraday cup system is a factor of 10^{-5} smaller than the lowest rate the EGF-3104 can produce.

5.3.2. E-Gun Parameter Tests

The following chapter will give an overview of the measurements that have been performed to characterize the Kimball EGF-3104. The influence of the different main parameters 1st

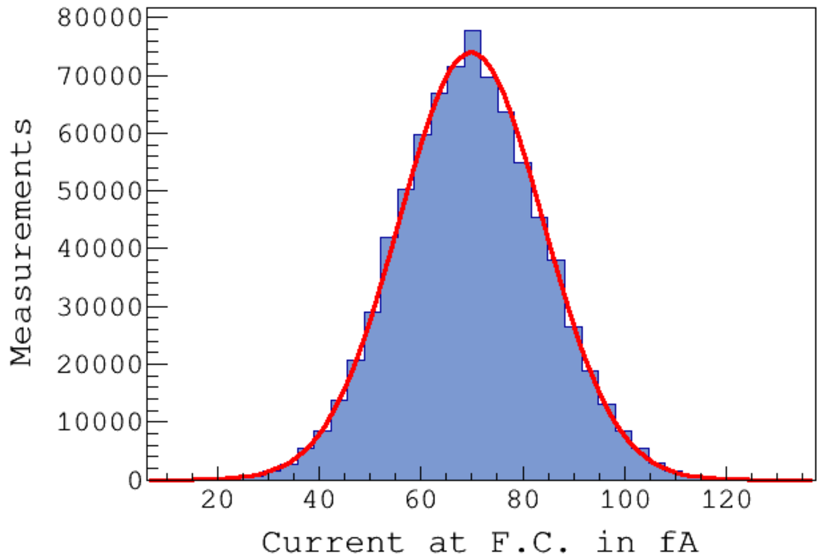

Figure 5.5.: With a noise level of 69.92 fA with a standard deviation of 14.19 fA, the Faraday cup meets the required stability.

Anode, Focus and Grid voltage have been investigated and an optimal setting for stability measurements (chapter 5.3.3) has been determined. Furthermore, the different emission modes of the gun (emission current control and pulsing) were tested. Finally, the spot size of the electron beam was controlled, based on simulated data by the manufacturer and an indirect measurement made with the Faraday cup.

Variation of the Grid, 1st Anode and Focus

To test the influence of the three major e-gun parameters, the Focus, Grid and 1st Anode voltage was varied, while keeping the other two parameters constant.

Grid: Figure 5.6 shows the effect of different Grid voltages. As expected, the emission current of the e-gun and therefore the signal current measured at the Faraday cup, cuts off at certain Grid voltages. According to equation 5.3, a high Grid potential leads to an increased electric field F and respectively a higher ΔW, which leads to a reduced emission current density $J(T, F)$ (equation 5.2).
Furthermore, it is found that the Grid voltage required for the cutoff is significantly influenced by the 1st Anode and Focus voltage. An increase of the 1st Anode and Focus voltage leads to an increased signal rate. The higher the two potentials are, the more Grid voltage is needed to prevent the electron emission at the cathode.

Focus: The Focus is a cylindrical unit, positioned in the forward direction of the beam. It can be set to a positive potential referenced to the cathode. Figure 5.7 shows the signal current at the Faraday cup at different Focus voltages. The measurements were made at different 1st Anode settings, while the Grid voltage was always kept at the lowest possible

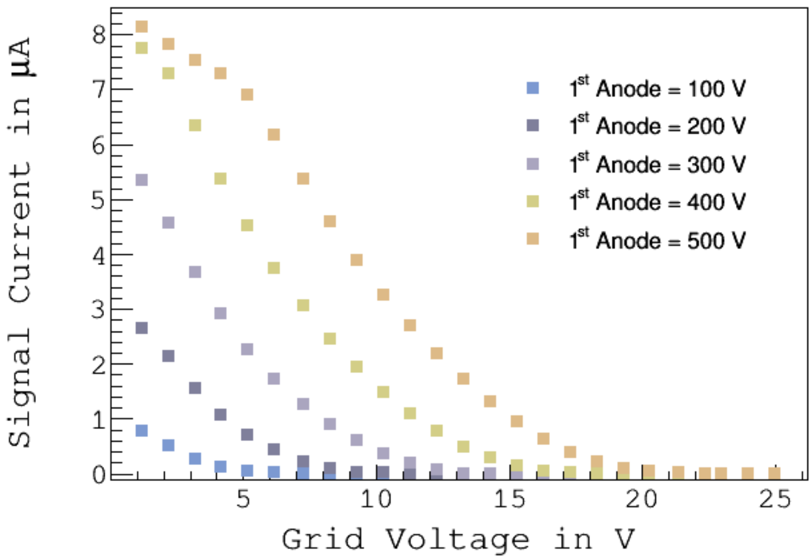

Figure 5.6.: Signal current measured at the Faraday cup. The electron energy is set to 20 keV. Increasing the Grid voltage leads to a cutoff of the signal rate. The required voltage for the cutoff is influenced by the 1st Anode and Focus voltage. The Focus voltage was always set to 22% of the 1st Anode voltage.

value of 1.6 V.

An increased Focus voltage leads to a lower rate at the detector. Because of the positive potential of the Focus, the electron beam is widened with higher potential. Hence, the rate at the detector is declined. An increase of the 1st Anode voltage further enhances this effect. However, the increase stops at a 1st Anode voltage of 400 V. Between the 1st Anode voltages of 400 and 500 V, only a slight difference in the rate can be observed.

1st Anode: The 1st Anode is a spherical mesh aperture, set to the same potential as the high voltage pot. Increasing the 1st Anode potential makes it more positive referenced to the cathode. An increase of the potential leads to a higher signal current at the detector (see figure 5.8). Until the 1st Anode voltage reaches a value of approximately 350 V, the signal current increases exponentially. After that it continues to increase slowly. For high Focus voltages, the signal current reaches a plateau.

In combination with the measurements shown in figure 5.7 it is observed that a high 1st Anode and a low Focus voltage leads to the highest signal current at the detector.

Emission Current Control Mode

The power supply of the EGF-3104 is equipped with a feedback stabilized Emission Current Control (ECC). With a constant source current and voltage driving of the Ta-cathode, the emission current varies over time. The changes are due to variations of the cathode resistance, caused by temperature instabilities, evaporation or contamination of the cathode surface. The ECC maintains a constant emission current by using feedback control to adjust the source voltage and current.

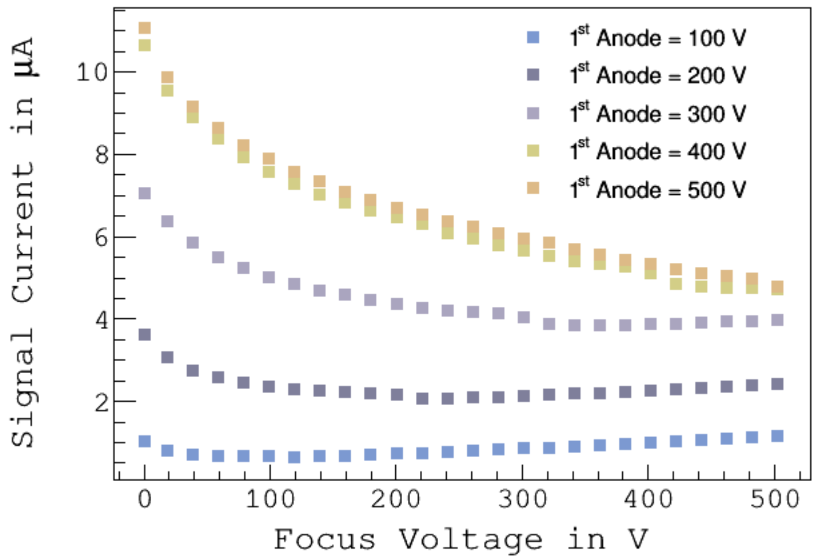

Figure 5.7.: Variation of the Focus voltage at different 1st Anode potentials. After a short drop, the rate is almost constant for different Focus voltages. The different 1st Anode settings cause an offset in the signal rate. Higher 1st Anode voltages lead to a higher signal rate due to its beam focusing effect.

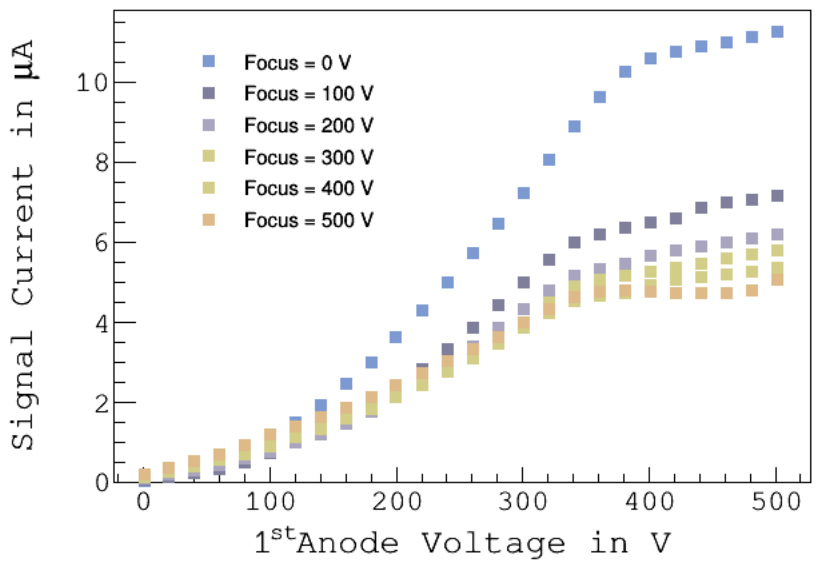

Figure 5.8.: Variation of the 1st Anode voltage at different Focus voltages. The signal rate increases with the 1st Anode voltage. Depending on the Focus setting, the signal reaches a plateau value.

To spare the cathode, it is useful to run the e-gun at the lowest possible source current and voltage. Therefore, various combinations of the Focus and 1st Anode voltage were tested. The combination that reached the highest signal rate at the Faraday cup, by straining the cathode with the lowest source current and voltage, is used in the long term stability measurements in section 5.3.3.
An optimal setting is found for the parameter

$$U_{\text{Focus}} = 0 \text{ V} \tag{5.4}$$

$$U_{\text{1stAnode}} = 500 \text{ V} \tag{5.5}$$

$$U_{\text{Grid}} = 5 \text{ V}. \tag{5.6}$$

Pulsing of the E-gun

As shown in figure 5.6, the electron emission of the e-gun can be blocked by setting the control Grid to negative potential. By alternating on-off switching of the Grid voltage, the electron signal from the EGF-3104 can be pulsed up to a frequency of 5 kHz.
To test the pulsing mode, an external TTL (transistor-transistor logic) generator was connected to the power supply of the EGF-3104. Figure 5.9 (a) shows a 0.2 Hz pulsed signal measured with the Faraday cup. The signal pulse has a length of 5 seconds and is regular and shows no abnormalities.
Frequencies higher than 2.5 Hz can not be resolved by the Faraday cup, because of the integration time[3] of 0.4 s. Instead, the integrated rate is measured at the Faraday cup. By changing the duty cycle[4] of the pulsed e-gun, the measured integrated rate changes correspondingly. This effect is shown in figure 5.9 (b) fore a frequency of 1 kHz and duty cycles from 20 - 100%.

The Spot Size

To verify the declarations of the manufacturer (15 - 50 mm spot size, depending on the working distance), it is necessary to find a way to determine, or at least estimate the spot size. However, it is difficult to directly measure the spot size of the electron beam. One way is to install a phosphorus plate and illuminate it with the complete electron beam. The beam electrons stimulate fluorescence light on the plate surface, which could be observed through a special assembly, like a window in the vacuum chamber. Nevertheless, such an elaborate installation is beyond the scope of the first commissioning.
Therefore, a simple geometrical estimation based on simulated data by the manufacturer was made and verified by a measurement with the Faraday cup system.
Figure 5.10 shows the simulated data by Kimball Physics.

[3] The charge of the electrons are collected at the metal plate of the Faraday cup for 0.4 seconds before it is read-out by the picoammeter. The integration is necessary to measure low signal rates.

[4] The duty cycle states the percentage of time where the Grid gets voltage from the TLL generator. For example if the pulse length is set to 10 seconds (0.1 Hz), a duty cycle of 20% would lead to a signal length of 2 seconds and a no-signal length of 8 seconds.

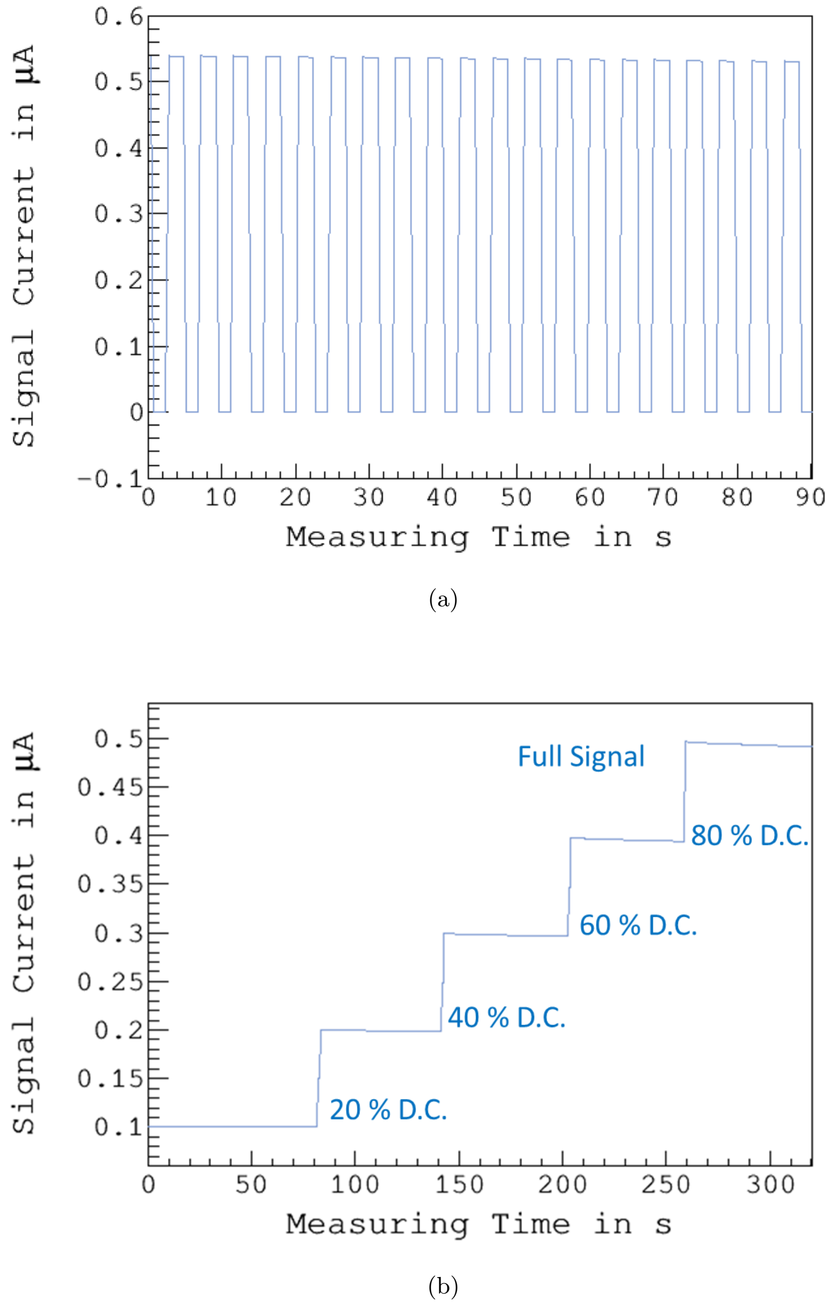

Figure 5.9.: A pulsed signal (a) from the EGF-3104, measured at the Faraday cup. The Grid voltage alters with a frequency of 0.2 Hz, which is corresponding to a pulse length of 5 seconds. The signal rate at the Faraday cup for different duty cycles of the pulse generator (b). A change of the duty cycle causes a corresponding change in the integrated rate.

The spot size at a working distance of 100 mm is quoted with 40 mm. Therefore, the opening angular is given by

$$\Theta = \tan^{-1}\left(\frac{40\text{ mm}}{100\text{ mm}}\right) = 21.8^\circ. \tag{5.7}$$

At a working distance of 322 mm (distance from e-gun to Faraday cup), the spot size

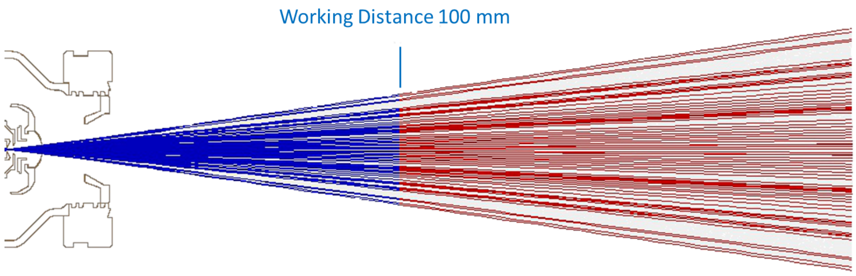

Figure 5.10.: The simulated data from Kimball physics. With the shown set of parameter, the spot size should be 40 mm at a working distance of 100 mm. Illustration from Kimball Physics, USA.

should be $s_2 = 128.8$ mm.
With a Faraday cup aperture diameter of 9.5 mm the ratio x of the spot size and aperture area is

$$x = \frac{A_{\mathrm{FC}}}{A_{\mathrm{spot}}} = \frac{\pi r_{\mathrm{FC}}^2}{\pi r_{\mathrm{spot}}^2} = \frac{(9.2\ \mathrm{mm})^2}{(128.8\ \mathrm{mm})^2} = 5,4 \cdot 10^{-3}. \tag{5.8}$$

The estimated signal rate on the Faraday cup $R_{\mathrm{FC}}^{\mathrm{est}}$ should be given by multiplying the rate adjusted at the e-gun $R_{\mathrm{EGF}} = 20$ nA with the ratio x

$$R_{\mathrm{FC}}^{\mathrm{est}} = x \cdot R_{\mathrm{EGF}} = 5.4 \cdot 10^{-3} \cdot 20\ \mathrm{nA} = 0.108\ \mathrm{nA}. \tag{5.9}$$

The measured rate at the Faraday cup

$$R_{\mathrm{FC}}^{\mathrm{meas}} = 0.588\ \mathrm{nA}, \tag{5.10}$$

is approximately higher by a factor of 5. Beam non-uniformities are a possible uncertainty that could explain the discrepancy of the measured and estimated signal.

5.3.3. Rate Stability Measurements

For testing the new TRISTAN detector, an electron source with a stable rate over time is crucial. Therefore it is necessary to test the EGF-3104 for longterm stability. As shown in figure 5.5, the noise of the Faraday cup is low enough to measure the stability of 10^{-4} specified by the manufacturer.
With the parameter setting found in the previous section, the e-gun is set to an emission current of 300 nA. The signal current at the Faraday cup is measured over a period of 40 hours. Figure 5.11 shows the measurement for 10 keV electron energy. The following observations can be made:

1. The electron emission of the e-gun varies significantly (approximately 5%) in the first 12 hours of the measurement.
2. For a runtime of 12 to 40 hours, the measured rate was stable with a variation of approximately 0.1% accuracy. Figure 5.14 (a) shows a histogram of a 10 hour interval

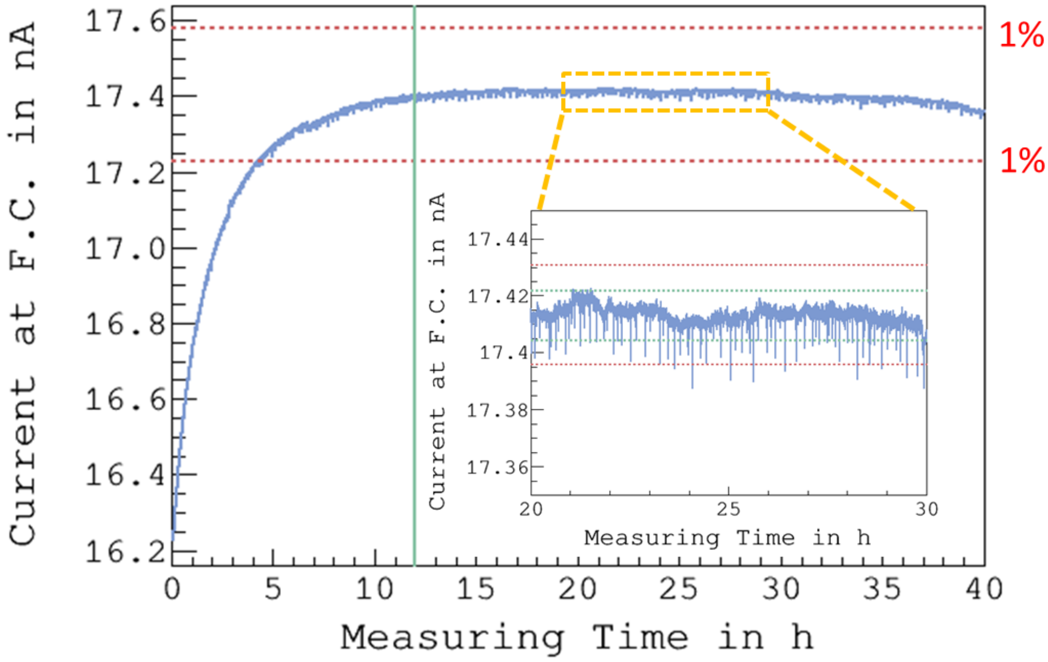

Figure 5.11.: A 40 hour measurement of a 10 keV electron beam coming from the EGF-3104. In the first 12 hours (vertical green line), the signal rate increases continuously until it reaches a plateau value. The red dotted line is the 1% error band of the mean signal value, calculated for measurements in the interval from 12 to 40 hours. The yellow dotted box shows the measurement in an interval from 20 to 30 hours. In the zoomed figure, the red dotted lines are the 0.1% error band. The signal is within the intended stability range according to the manufacturer (0.1% per hour). However, sudden decrease of the signal rate occur on a non-regular basis. Without the discharges, a even higher stability of 0.05% (green dotted line) could be reached.

of the measurement. The values are Gaussian distributed around a mean value of 17.41 nA, with a standard deviation of $\sigma = 2.43 \cdot 10^{-3}$ nA. This corresponds to a beam stability of 0.14%, which is above the declaration by the manufacturer of 0.1%.

3. Sudden negative peaks of the signal appear in irregular intervals, which are high likely attributed to discharging effects. Figure 5.14 (b) shows a close-up of such a discharging. The signal rate cuts off for a time frame of 10 seconds. The reason for the discharges are most probably caused by a charging of the Faraday cups outer shielding or another component in the beam tube. Further investigations with a different detector system, could help to understand the problems.

The 40 hour measurements where repeated at different electron beam energies. Figure 5.13 shows the energy dependence of the measured rate at the Faraday cup. The signal shows an energy dependence within a deviation of 10%, most probably caused by differences in the deflection of the beam by the e-gun's 1st Anode. Measurements with electron energies lower than 4 keV and higher than 12 keV, showed irregularities, which are described in the following.

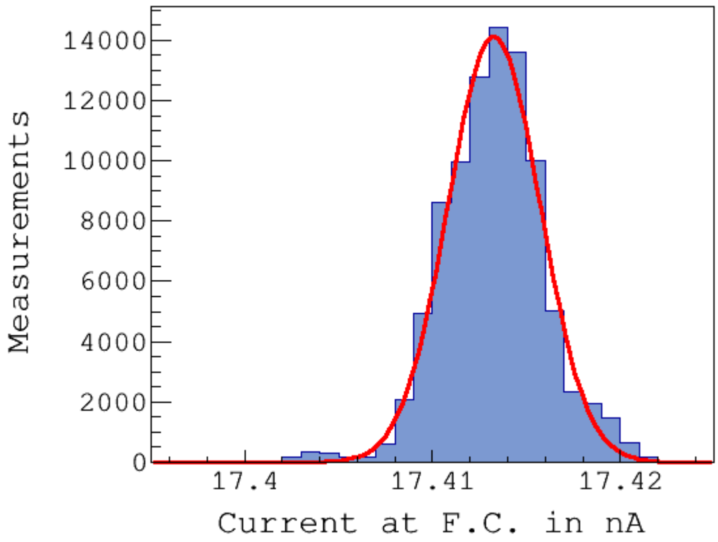

(a)

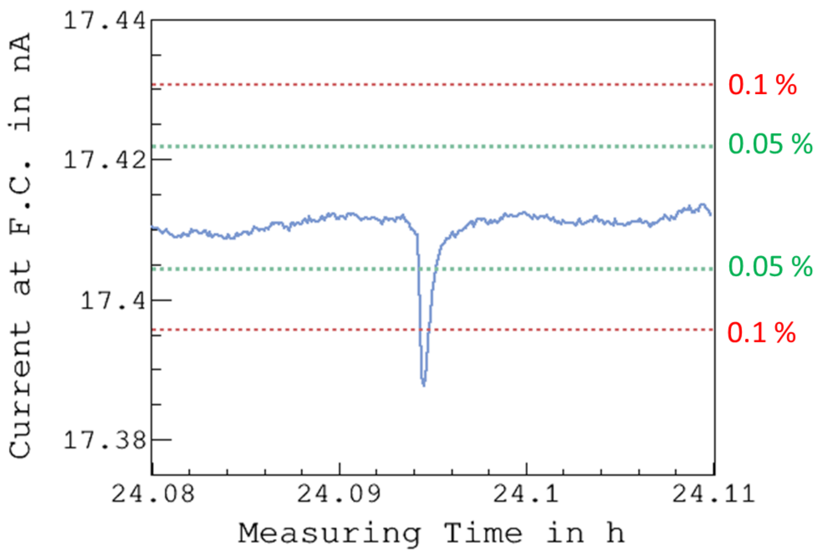

(b)

Figure 5.12.: The measurements in the 10 hour interval (a) are Gaussian distributed around a mean value of 17.41 nA with a standard deviation of $\sigma = 2.43 \cdot 10^{-3}$ nA that corresponds to 0.14%. The rate stability is slightly above the specification by the manufacturer. A detailed view on a discharge is shown in (b). The effect lasts for approximately 10 seconds. During that time, the signal gets out of the 0.1% error range (red dotted line). For the rest of the measurement, the signal has a stability better than 0.05% (green dotted line).

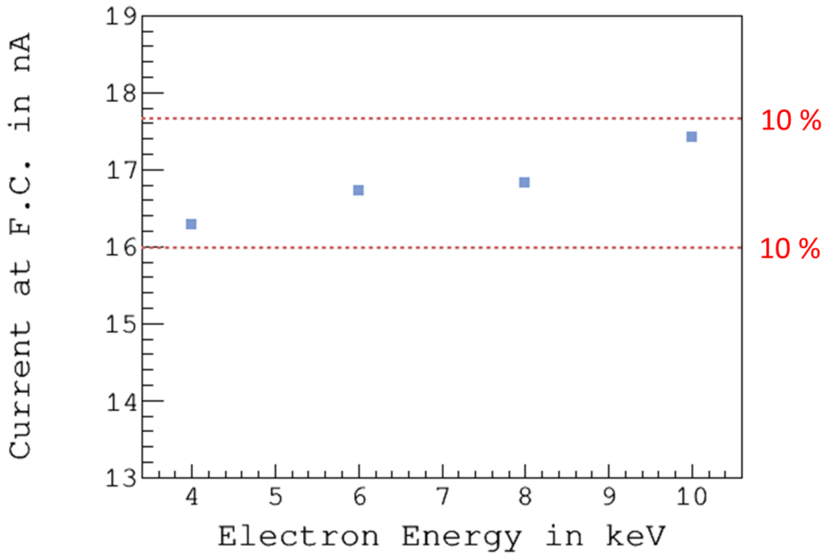

Figure 5.13.: The energy dependence of the signal rates, resulting from 40 hour measurements at different beam energy settings. The red dotted lines show the deviation area of 10% from the mean value. The energy dependence most probably arises from the electrostatic setting of the e-gun. Further investigations have to verify this assumption.

Low and High Energy Behavior

The rate stability measurements were performed for electron beam energies between 2 - 18 keV. The measurements showed, that the discharging effects strongly increase with higher electron energies. Figure 5.14 (a) shows the result from the 40 hours measurement with 16 keV electron energy.
For beam energies lower than 4 keV, a continuous rise of the signal over the entire measurement interval was observed. Figure 5.14 (b) shows the signal rate for 2 keV electrons, measured at the Faraday cup. The signal falls for approximately the first hour. After that it starts to rise, but in contrast to the other measurements, a plateau value is not reached. The difference of the lowest to the highest signal rate is with 3.51% out of the accuracy predicted by the manufacturer.

5.3.4. Conclusion of the Measurements

The initial measurements have revealed that the functionality of the e-gun is as expected and that the major part of the device parameters are as specified by the manufacturer. However, stability measurements of 40 hours did show irregular behavior. Based on the stability measurements, the following conclusions can be made:

1. The indicated stability of 0.1% per hour, can be verified by the measurements, for electron energies from 4 keV to 12 keV.
2. Sudden decreases of the signal rate at irregular distances appear mainly at higher electron energies. These are likely to be discharges, but their origin has not yet been identified. The measurements showed, that without the discharges a stability of $< 0.1\%$ could be reached.

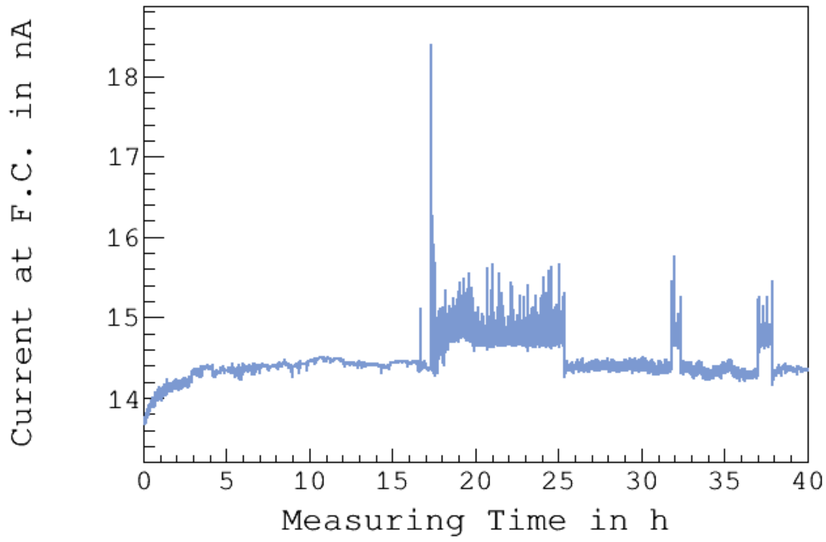

(a)

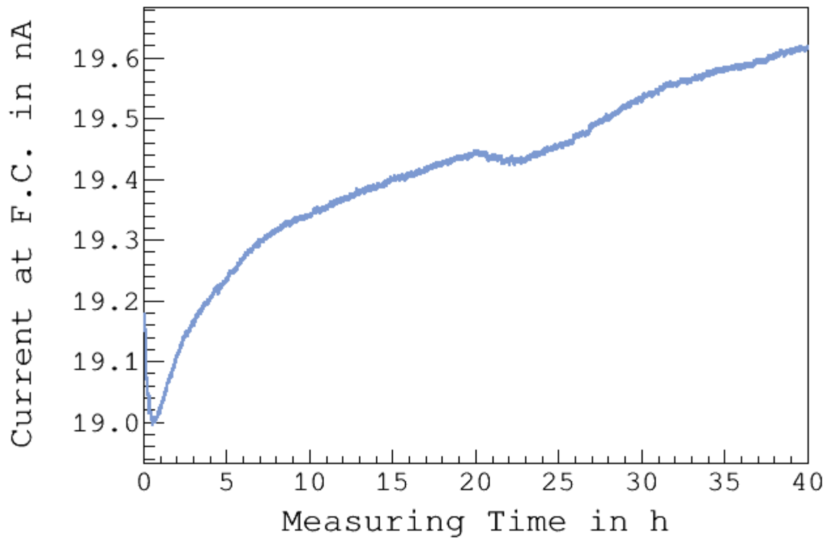

(b)

Figure 5.14.: The discharging effects strongly increase with beam energies higher than 12 keV. An example for a beam energy of 16 keV is shown in (a). At low energies, the electron signal from the EGF-3104 is continuously increasing (2 keV measurement is shown in b). Unlike the measurements between 4 - 12 keV electron energy, the signal never reaches a plateau value.

3. There is a clear energy dependence of the rate. A likely reason is the used electrostatic setting of the EGF-3104.

4. At low and high electron energies, the stability behavior changes drastically.

As a next step, the grounding of any unit in the beam tube of the test setup needs to be optimized, to reduce the risk of sudden discharges. The future measurements that are described in the following section, provide a good opportunity to cross-check the measurements performed with the Faraday cup system.

5.4. Outlook and future Measurements

The characterization of the TRISTAN prototype detector is planned to start in October 2015. Prior to that, two measurements are planned to be performed at KIT, involving the high-intensity e-gun.

Electron Backscattering on a thin Gold Surface

As mentioned in chapter 3, the sensitivity of KATRIN to keV-scale sterile neutrinos is strongly dependent on systematic uncertainties. One of those uncertainties is the backscattering of electrons on the gold surface of the rear wall of the WGTS. Energy loss due to backscattering processes will change the shape of the β-decay spectrum and could mimic a kink similar to the sterile neutrino signature.
Profound simulation studies will help to understand the influence of backscattered electrons to the sensitivity. However, an experimental validation is of great importance. For this reason, an experimental setup was designed to measure electron backscattering on the rear wall gold surface.
A vacuum vessel identical to the rear wall is the basic unit of the experiment. The high-intensity e-gun is aligned on the one end and provides electrons with energies from 1-20 keV, with rates similar to the rates in the KATRIN source. The stability of the electron rate coming from the e-gun is monitored by measuring the X-ray spectrum induced by the signal electrons hitting the thin gold surface. The measurement is performed by using the silicon drift detectors of the BIXS-unit (**B**eta **I**nduced **X**-ray **S**pectrum [Käf12]) of the KATRIN experiment. The BIXS-detector system is designed to monitor the tritium activity of the KATRIN source, by measuring the X-ray spectrum of the β-electrons that hit the rear wall gold surface.
A micro-channel plate is a detector technology that could be applicable to measure the backscattered electrons. It consists of a metal plate with a regular array of holes (micro-channels). The top and bottom side of the plate are set to different potentials. If an electron enters a channel, it gets accelerated and multiplied due to scattering processes with the wall of the channel. The cascade of secondary electrons is measured at the the end of the channel for example with a small metal anode. Figure 5.16 shows a schematic drawing of a micro-channel plate.
If the different channels are read-out separately, a spatial resolution is possible. However, micro-channel plates are also sensitive to X-rays. The BIXS detectors are covered by a beryllium window and hence only measure the X-ray signal. This information can be used to discriminate the X-ray background and subtract it from the signal at the micro-channel plate.

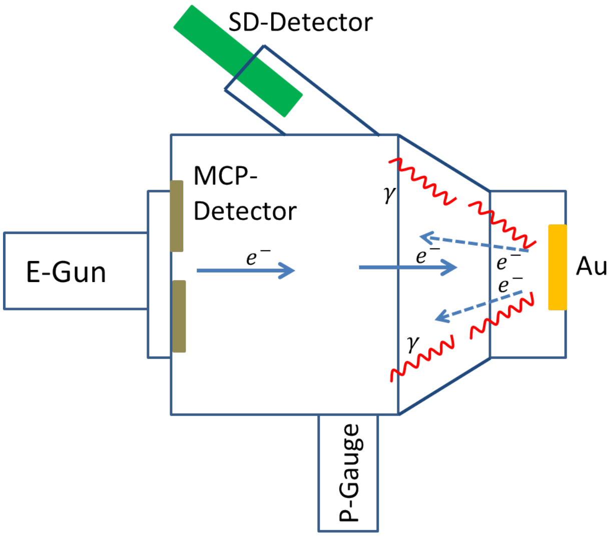

Figure 5.15.: An experimental setup to measure electron backscattering at a thin gold surface. The e-gun stability is monitored by measuring the X-ray spectrum, induced by the electrons on the gold surface, using a silicon drift detector. The backscattered electrons are measured with a micro-channel plate.

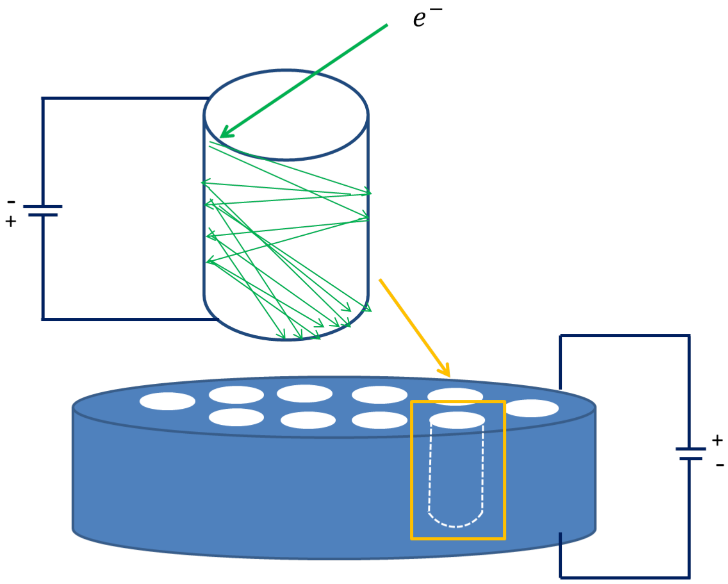

Figure 5.16.: A schematic drawing of a micro-channel plate detector. The top and bottom side of the metal plate are set to different potentials. Therefore, the electrons get accelerated once they entered the channel. By hitting the wall, they generate a cascade of secondary electrons and amplify their electric signal.

Background Studies and Transmission Probability of High Surplus Energy Electrons at the Monitor Spectrometer

As described in chapter 2.2, the pre-spectrometer of the KATRIN experiment will be most likely set to a very low retarding potential, to avoid a Penning trap between the pre- and main spectrometer. As a consequence, the scanning of the β-decay electrons has to be done by the main spectrometer only. At full source strength, the WGTS delivers a rate of approximately 10^{11} electrons per second. The background in the main spectrometer is estimated with a rate of only 10^{-4} counts per second with a pressure of 10^{-11} mbar. The new high-intensity e-gun EGF-3104 provides an evaluation of the background estimations with full WGTS strength, well before the WGTS is operational.
This measurement will be performed in the next measurement phase of KATRIN in summer 2016. In a first step, an analogue experiment using the monitor spectrometer as a main spectrometer replacement, is planned.
For this purpose, the EGF-3104 is mounted to the monitor spectrometer. The spectrometer is set to different retarding potentials and the background at the detector is measured at different electron energies. In a second step, the pressure in the spectrometer will be varied, to study the pressure dependency of the spectrometer background.

Furthermore, this experimental setup allows for an investigation of transmission probability of high surplus energy electrons, as discussed in chapter 4. Therefore, the retarding potential of the monitor spectrometer will be set to zero or very low potential. The transmission rate as a function of the electron energy, is detected at the monitor spectrometer detector.
The monitor spectrometer is surrounded by an air coil system of three air coil magnets. This provides an opportunity to prove the principle of adiabatic transportation at higher magnetic fields in the analyzing plane of the spectrometer investigated in chapter 4.

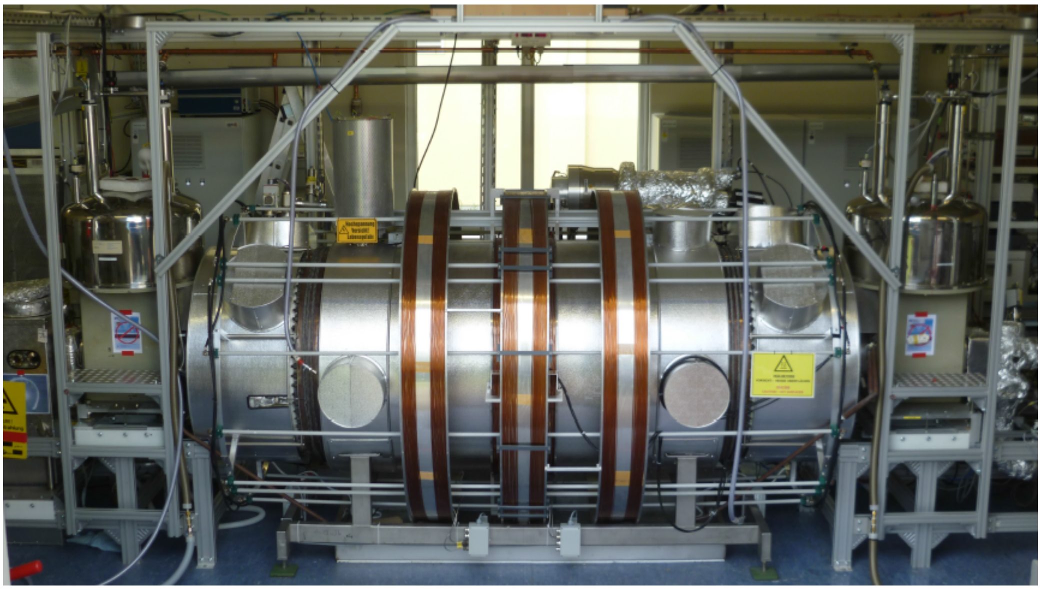

Figure 5.17.: The illustration shows the monitor spectrometer. In normal KATRIN mode it is used to monitor the high voltage stability of the main spectrometer. Before that, it will be used to study background behavior of the spectrometer at high signal electron rates. Furthermore, three air coils provide a opportunity to prove the principle of an adiabatic transportation of high surplus energy electrons, investigated in chapter 4. Illustration from [Erh12].

6. Conclusion and Outlook

The KATRIN experiment is a next-generation, large-scale β-decay experiment with the key goal to probe the effective neutrino mass with a sensitivity of 200 meV (90% C.L.) by analyzing the shape of the tritium β-spectrum close to the endpoint. Because of the rather small signal rate in the region-of-interest, KATRIN will operate a gaseous tritium source with unprecedented high luminosity of $\lambda_\mathrm{d} \approx 10^{11}$ decays per second.
These particular source properties offer the opportunity to extend the physics reach of KATRIN after having achieved its main goal. This second KATRIN phase would be focused on looking for possible sterile neutrinos in the eV to multi-keV range. This thesis focuses on the search for keV-scale sterile neutrinos, which are well motivated candidates for dark matter.

A sterile neutrino would manifest itself by a tiny kink-like signature and small spectral distortion in the β-decay spectrum. In order to look for sterile neutrinos, the signal region has to be extended to cover the entire phase space of tritium β-decay.

As a first step, this work shows that after a three year measurement of the tritium β-decay spectrum with a source strength comparable to the KATRIN source, a statistical sensitivity for the mixing angular $\sin^2\theta = 10^{-8}$ for sterile neutrino masses of $m_\mathrm{s} = 1 - 18$ keV could be reached. Furthermore it is shown, that the influence of theoretical and experimental systematic uncertainties have the potential to reduce the sensitivity significantly. Hence, an extensive investigation of all possible theoretical and of all individual experimental systematic effects needs to be performed, to assess the final sensitivity.

To search for keV-scale sterile neutrinos, the entire tritium β-decay spectrum is of interest and consequently the main spectrometer has to be operated at zero or very low retarding potential to allow all β-decay electrons to reach the detector. However, electrons with energies well above the retarding potential (i.e. high surplus energy electrons), show non-adiabatic trajectories in the main spectrometer, which in turn would cause a change of the transmission probability. This work has studied the effects of non-adiabatic electron transport and demonstrates, that an increase of the magnetic field in the center of the main spectrometer by a factor of 4.0, would allow to regain a fully adiabatic electron transport, even for very high surplus energies of up to 20 keV. This can be achieved by making use of an extension of the large volume air coil system that surrounds the main spectrometer.

As a consequence of the high rates that have to be handled to reach the aimed sensitivity, a new detector and read-out system has to be designed. Within the TRISTAN sub-project embedded into the KATRIN experiment, a prototype detector based on a small point contact multi-pixel system is currently being build at the Halbleiterlabor in Munich. To reduce systematic uncertainties caused by the detector system such as electron backscattering at the silicon surface, energy loss in the dead layer, pile up, dead-time or energy non-linearities, an accurate calibration has to be provided. To do so, a well-calibrated electron source is crucial.
Accordingly, another focus of this work has been the commissioning and characterization as well as in-depth testing of the new high-intensity electron gun EGF-3104 from Kimball Physics, using a Faraday cup system. Initial measurements have revealed that the functionality of the e-gun is as expected and that the major part of the device parameters are as specified by the manufacturer. However, stability measurements of 40 hours did show irregular behavior, especially for beam energies smaller than 4 keV and larger than 12 keV. At intermediate energies from 4 keV $< E_{\text{Beam}} <$ 12 keV the expected stability of 0.1% per hour is reached. Moreover, small discharging effects were observed, which are likely caused by the Faraday cup detector. Further investigations on the stability behavior of the high-intensity e-gun will be performed with another detector setup designed in this work.

Furthermore, two more upcoming experiments have been prepared, which will make use of the EGF-3014 to investigate experimental systematic uncertainties, in a keV-scale sterile neutrino search. First, backscattering of electrons at the rear wall of the source section will be investigated using the BIXS detector system of KATRIN in combination with a micro-channel plate detector. The second experiment will use the monitor spectrometer of KATRIN to study background, caused by high surplus energy electrons in combination with adiabaticity measurements to evaluate the experimental results discussed in chapter 4.

In conclusion, this master thesis has laid the ground work for many upcoming works and theses dedicated to searching for keV-scale sterile neutrinos in tritium β-decay over the next years. The search for sterile neutrinos with a model-independent laboratory experiment would be a significant extension of the world-wide effort in this field. KATRIN is in the unique position to provide statistical sensitivity in the cosmological allowed parameter space.

Appendix

A. Set of Parameter for the β-Decay Spectrum Calculations

The parameter used to calculate the tritium β-decay spectrum for the sensitivity study shown in chapter 3:

Tiritum Column Denstity (molecules):	$\rho d = 5 \cdot 10^{17}\ mol/cm^2$
Radius of Fluxtube in the WGTS:	$r_{flux} = 4.1\ cm$
Tritium Purity:	$\epsilon_T = 0.95$
Number of Tritium Nuclei in the WGTS:	$N_T = 2 \cdot \epsilon_T \cdot r_{flux}^2 \cdot \pi \cdot \rho d = 5.016 \cdot 10^{19}$
Tritium Atom Decay Rate:	$\Gamma = 1.783 \cdot 10^{-9}\ s^{-1}$
Maximal acceptable polar angle:	$\theta_{max} = 50.77°$
Endpoint of Tritium Decay:	$E_0 = 18575\ eV$
Detector Efficency:	$\epsilon_D = 0.90$
Integrated Fermi Function with $m_\nu = 0$:	$W_F = 9.652 \cdot 10^{22}\ eV$

Normalization Constant: $C_T = N_T \cdot \left(1 - \cos\left(\frac{\theta_{max}}{180° \cdot \pi}\right)\right) \cdot \frac{1}{2} \cdot \epsilon_D \cdot \frac{\Gamma}{W_F} = 1.532 \cdot 10^{-13}$

B. Theoretical Uncertainties on the β-Decay Spectrum used in the Sensitivity Study

The following theoretical uncertainties on the β-decay spectrum where taken into account, to calculate the sensitivity from figure 3.5 from chapter 3.2.1.
There relative difference is defined by

$$\delta\psi_i = \frac{(d\Gamma/dE)^{\text{corr}}}{(d\Gamma/dE)^{\text{uncorr}}} - 1 \tag{6.1}$$

with

$$\psi_i = \mathrm{F}, \mathrm{S}, \mathrm{Q}, \mathrm{R}, \mathrm{I}, \mathrm{C}, \mathrm{L}_0, \mathrm{G} \tag{6.2}$$

and the β-decay spectrum $(d\Gamma/dE)^{\text{corr}}$ with corrections and $(d\Gamma/dE)^{\text{uncorr}}$ without.

The corrections are:

Relativistic Fermi Function

$$F(W,Z) = 4(2pR/m_e)^{-2(1-\gamma)} \cdot |\Gamma(\gamma+iy)|^2/(\Gamma(2\gamma+1))^2 \cdot \mathrm{e}^{\pi\gamma}, \tag{6.3}$$

with $Z = 2$ for He, α_{em} the fine structure constant of the electromagnetic interaction, $y = \alpha_{\text{em}} ZW/p$, $\gamma = \sqrt{1-\alpha_{em}^2 Z^2}$ and $R = 2.8840 \cdot 10^{-3}$ the nuclear radius of He nuclei in units of m_e, given by the Elton formula [Elt58].

Screening of the Nuclear Potential by the Orbital Electron

$$S(Z,W) = \overline{W}/W(\bar{p}/p)^{2\gamma-1}\mathrm{e}^{\pi(\bar{y}-y)}\frac{|\Gamma(\gamma+i\bar{y})|^2}{|\Gamma(\gamma+iy)|^2}, \tag{6.4}$$

with $\bar{y} = \alpha_{\text{em}} Z\overline{W}/p$,$\overline{W} = W - V_0$ and $V_0 \approx 1.45\alpha_{\text{em}}^2$ the screening potential [Beh82].

Quantum Mechanical Effect of Orbital Electron Exchange

$$\delta I(Z,W) = 2.462 \cdot \alpha(\eta)^2 + 0.905 \cdot \alpha(\eta), \tag{6.5}$$

where

$$\alpha(\eta) = \eta^4 \cdot \mathrm{e}^{(2\eta \cdot \tan^{-1}(-2/\eta))/(1-0.25\eta^2)^2}, \tag{6.6}$$

with $\eta = -2\alpha_{\text{em}}/p$ [Hax85].

Recoil Effects, Weak Magnetism and V-A Interference

$$\delta R(W, W_0, M) = (a \cdot W - b/W)/c \tag{6.7}$$

with

$$a = 2\frac{(5\lambda_t^2 + 2\lambda_t \cdot \mu + 1)}{M} \tag{6.8}$$

$$b = 2\lambda_t \frac{(\lambda_t + \mu)}{M} \tag{6.9}$$

$$c = 1 + 3\lambda_t^2 - b \cdot W_0. \tag{6.10}$$

M is the mass of ^{3}He in units of m_e [Bil60]. $\lambda_t = 1.265 \pm 0.0035$ denotes the ratio of the axial-vector to the vector coupling for weak interaction in triton β-decay [Aku02]. The difference between the magnetic moment of trition and helion is given by $\mu = 5.106588$ with a negligible error (from http://nist.gov/).

Recoil Coulomb Field

$$\delta Q(Z, W, W_0) = \frac{\pi \cdot \alpha_{\text{em}} \cdot Z}{M \cdot (p/m_e)} \left(1 + \frac{1 - \lambda_t^2}{1 + 3\lambda_t^2} \frac{W_0 - W}{3W}\right), \tag{6.11}$$

from [Wil82].

Finite Extension of the Nucleus

The finite extension of the nucleus is given by

$$\delta L_0(Z, W) = \frac{13}{60}(\alpha_{\text{em}} Z)^2 - W \cdot R \cdot \alpha_{\text{em}} \cdot Z \cdot \frac{41 - 26\gamma}{15(2\gamma - 1)} - \alpha_{\text{em}} \cdot Z \cdot R \cdot \gamma \cdot \frac{17 - 2\gamma}{30 \cdot W(2\gamma - 1)}, \tag{6.12}$$

with the finite size of the weak interaction

$$\delta C(Z, W) = C_0 + C_1 \cdot W + C_2 \cdot W^2, \tag{6.13}$$

$$C_0 = -\frac{233(\alpha_{\text{em}} \cdot Z)^2}{630} - \frac{(W_0 \cdot R)^2}{5} + \frac{2(W_0 \cdot R \cdot \alpha_{em} \cdot Z)}{35}, \tag{6.14}$$

$$C_1 = -\frac{21(R \cdot \alpha_{\text{em}} \cdot Z)}{35} + \frac{4(W_0 \cdot R^2)}{9}, \tag{6.15}$$

$$C_2 = -\frac{4R^2}{9}. \tag{6.16}$$

All equations are from [Wil90].

Radiative Corrections

$$G(W, W_0) = (W_0 - W)^{(2\alpha_{\mathrm{em}}/\pi)t(\beta)}(1 + \delta G(W, W_0)), \tag{6.17}$$

with

$$\delta G(W, W_0) = \frac{2\alpha_{\mathrm{em}}}{\pi}\left(t(\beta)\left(\ln(2) - \frac{3}{2} + \frac{W_0 - W}{W}\right)\right) \tag{6.18}$$

$$+ \frac{1}{4}(t(\beta) + 1)\left(2(1 + \beta^2) - 2\ln\left(\frac{2}{1 - \beta}\right) + \frac{(W_0 - W)^2}{6W^2}\right) \tag{6.19}$$

$$+ \frac{1}{2\beta}\left(L(\beta) - L(-\beta) + L\left(\frac{2\beta}{1 + \beta}\right) + \frac{1}{2}L\left(\frac{1 - \beta}{2}\right) - \frac{1}{2}L\left(\frac{1 + \beta}{2}\right)\right), \tag{6.20}$$

with

$$t(\beta) = \frac{1}{2\beta}\ln\left(\frac{1 + \beta}{1 - \beta}\right) - 1 \tag{6.21}$$

$$L(\beta) = \int_0^\beta \frac{\ln(1 - t)}{t} dt, \tag{6.22}$$

and

$$\beta\frac{\sqrt{W^2 - 1}}{W}. \tag{6.23}$$

More information on the radiative corrections of the tritium β-decay spectrum can be found in [Rep83].

An illustration of the corrections are shown in the figure on the next page. They are displayed as a function of energy on an interval of [1 keV, 18 keV] on a parts per million scale [Mer14].

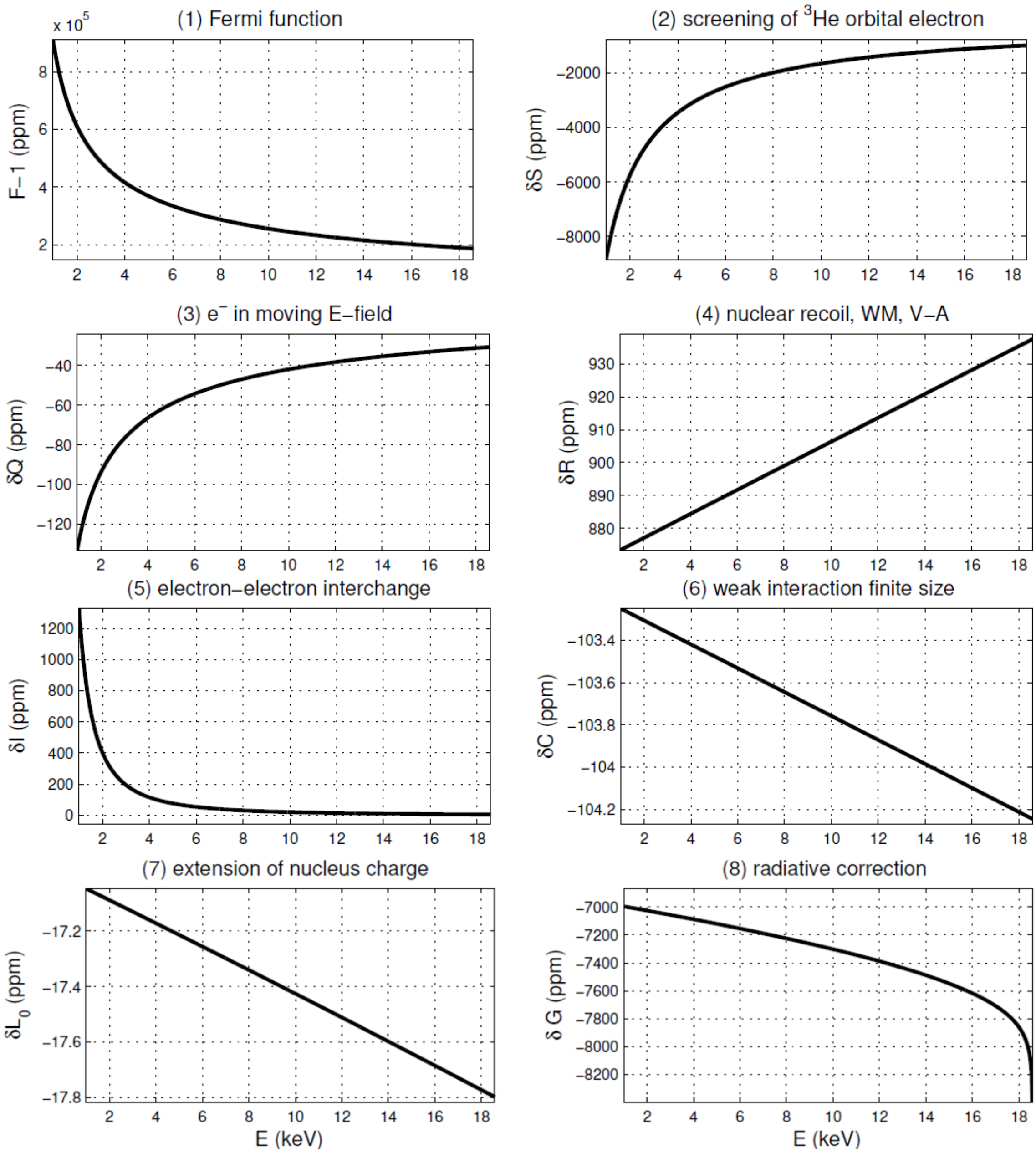

Figure B.1.: The theoretical uncertainties that have been taken into account to calculate the sensitivity in chapter 3.2.1. The relative difference is given in parts per million (ppm). (1) is the relativistic Fermi function, (2) the screening by the orbital electron, (3) the He molecule recoil an its Coulomb field, (4) the effect of the finite nuclear mass, (5) the interaction between the β-electron and the left behind orbital electron, (6) the effect of the finite size of the nucleus, to the solution of the Dirac equation for the β-electron, (7) the convolution of the lepton and nucleon wave functions through the nuclear volume, (8) radiative corrections of the first order. Figure from [Mer14].

C. Manufacturer Specifications of the Kimball EGF-3104

The EGF-3104 specifications. Parameters are taken from the data sheet of the manufacturer (Kimball Physics, USA):

EGF-3104 ELECTRON GUN SPECIFICATIONS	
BEAM ENERGY	200 eV to 20 keV (Independently adjustable)
BEAM CURRENT	Standard: 1 nA to 100 µA (Independently adjustable) High current option: 10 nA to 1 mA
ENERGY SPREAD	Approx. 0.4 eV cathode thermal spread, calculated
SPOT SIZE	15 - 50 mm at 100 mm working distance (Ind. adj.)
WORKING DISTANCE	Variable
BEAM DEFLECTION	Optional: Magnetic quadrupole (outside vacuum) for improved beam uniformity
PULSE CAPABILITY (using appropriate pulse generator, not included)	Dual Grid Power Supply: pulse width ~2 µs to DC rise/ fall ~500 ns, rep rate to 5 kHz (TTL required)
BEAM UNIFORMITY	Depends on mask aperture
FIRING UNIT	User-replaceable Firing Unit Cartridge includes cathode and Wehnelt (G-1) assembly
CATHODE TYPE	Standard: Refractory Metal Cathode Optional: Low-light Barium Oxide Yttria-coated Iridium
MOUNTING	2¾ inch rotatable CF, including both tapped and clear mounting holes
BEAM ALIGNMENT	Mechanical alignment with internal firing unit alignment. Optional mechanical alignment with a ± 2° Port Aligner.
INSERTION LENGTH	0 mm
GUN DIMENSIONS	70 mm OD x 205 mm length
FEEDTHROUGHS	Multipin brazed ceramic, threaded stainless steel shell
CABLES / CONNECTORS	Multiconductor high voltage fully ground-shielded cable with mating aluminum shell connector, to connect gun and power supply. Standard length: 3 m, Optional: 5 m
MAXIMUM BAKEOUT	350°C with cables removed

EGPS-3104 ELECTRON GUN POWER SUPPLY SPECIFICATIONS	
OUTPUTS	All necessary voltages to drive the EGF-3104 Electron Gun (in combination with H.V. Power Supply)
ENERGY STABILITY	±0.01% per hour ±0.02% per 8 hours at full output
BEAM STABILITY	±0.1% per hour with Emission Current Control (ECC) or ±10% per hour without ECC
CONTROLS	FlexPanel controls: Energy, Source, Grid (G-1), 1st Anode, Focus, Emission Current Control (ECC)
METERING	FlexPanel digital meters: Energy, Source Voltage, Source Current, Grid Voltage, Anode Voltage, Focus Voltage, Emission Current
COMPUTER/REMOTE CONTROL & METER	Power supplies: 0 to +10V (-10V to +10V, for deflection) Metering: 0 to +2V (-2V to +2V, for deflection) Toggle switches: 0 or +5V
INPUT	115 VAC switchable to 230 VAC, 50 to 60 Hz single phase, 250 VA
ENVIRONMENT	Temperature: 0 to 40°C, Relative humidity: 0 to 75% RH non condensing, Classified as a pollution degree 2, installation category
DIMENSIONS (width x height x depth)	EGPS-3104: 17 in. x 7 in. x 22 in. excluding handles (432 mm x 178 mm x 560 mm); 19 in.(495 mm) rack mountable.
WEIGHT	Appx. 35 lbs. (12 kg)

D. KASSIOPEIA Configuration File used for the Adiabaticity Simulations

This appendix chapter shows, a commented XML-configuration file for the KASPER simulation framework, which was used for the simulations done in chapter 4.

Setting of the Magnets

The current setting of the solenoid magnets on the pre-spectrometer side of the main spectrometer PS1 and PS2, and on the detector side the pinch magnet PCH and the detector magnet DET.

```
<external_define name="ps_1_current" value="157.0"/>
<external_define name="ps_2_current" value="157.0"/>
<external_define name="pinch_magnet_current" value="87.115"/>
<external_define name="detector_magnet_current" value="49.761"/>
```

Setting of the Air Coil System

The setting of the large volume air coil system that is surrounding the main spectrometer. The variable `turnfactor` defines the multiplication factor of the coil current. It was varied for the different simulations to study the influence of an increased magnetic field in the main spectrometer to the adiabatic transport of high surplus energy electrons.

```
<external_define name="turnfactor" value="1.0"/>
<external_define name="ac_setting" value="0"/>

<global_define name="ac_1_current" name="100.0*[turnfactor]"/>
<global_define name="ac_2_current" name="100.0*[turnfactor]"/>
<global_define name="ac_3_current" name="100.0*[turnfactor]"/>
<global_define name="ac_4_current" name="100.0*[turnfactor]"/>
<global_define name="ac_5_current" name="100.0*[turnfactor]"/>
<global_define name="ac_6_current" name="100.0*[turnfactor]"/>
<global_define name="ac_7_current" name="100.0*[turnfactor]"/>
<global_define name="ac_8_current" name="100.0*[turnfactor]"/>
<global_define name="ac_9_current" name="100.0*[turnfactor]"/>
<global_define name="ac_10_current" name="100.0*[turnfactor]"/>
<global_define name="ac_11_current" name="100.0*[turnfactor]"/>
<global_define name="ac_12_current" name="100.0*[turnfactor]"/>
<global_define name="ac_13_current" name="100.0*[turnfactor]"/>
<global_define name="ac_14_current" name="-100.0*[turnfactor]"/>
```

Setting of the Main Spectrometer

The main spectrometer retarding potential was set to $U_{\mathrm{ret}} = 0$ V.

```
<external_define name="use_advanced_potentials" value="0"/>

<external_define name= "ground_potential" value="0.0"/>
<external_define name="hull_potential" value="0.0"/>
<external_define name="dipole_potential" value="0.0"/>
<external_define name="wire_outer_offset" value="0.0"/>
<external_define name="wire_inner_offset" value="0.0"/>
<external_define name="steep_cone_additional_offset" value="0.0"/>
```

Particle Generators

The particles are generated at a disc with a diameter if 3.67 cm, with a homogeneous energy distribution and starting polar angles from 0° to 65.0°. As described in chapter 4, polar coordinates are used to describe the position of the particle.

```
<!- this generator makes a uniform random distribution of initial states near
the entrance of the spectrometer ->
<ksgen_generator_composite name="entrance_uniform">

<!- energy creation ->
<energy_composite>
           <energy_uniform value_min="0.0" value_max="20000.0" />
</energy_composite>

<!- position creation ->
<position_cylindrical_composite>
          <r_cylindrical radius_min="0.0" radius_max="3.67e-2"/>
          <phi_uniform value_min="0." value_max="360."/>
          <z_fix value="-12.10375"/>
</position_cylindrical_composite>

<!- direction creation ->
<direction_spherical_composite>
          <theta_spherical angle_min="0.0" angle_max="65.0"/>
          <phi_uniform value_min="0.0" value_max="360.0"/>
</direction_spherical_composite>
```

Setting of the Trajectory Calculations

For the particle tracking, the exact trajectory with 16 steps per cyclotron motion was used.

```
<kstraj_trajectory_exact name="trajectory_exact">
     <integrator_rk8 name="integrator_rk8"/>
     <term_propagation name="term_propagation"/>
     <control_cyclotron name="control_cyclotron" fraction="1./16."/>
</kstraj_trajectory_exact>
```

Particle Terminators

The particles were terminated, if they hit the inner surface of the main spectrometer vessel (`term_max_r`) or leave the spectrometer on the detector side (`term_max_z`) or the pre-spectrometer side (`term_min_z`). Due to non-adiabatic behavior, the electrons can get trapped in the spectrometer. If the electron turns more then ten times inside the main spectrometer, the particle gets terminated (`term_trapped`).

```
<ksterm_max_r name="term_max_r" r="5.0"/>
<ksterm_min_z name="term_min_z" z="-12.5"/>
<ksterm_max_z name="term_max_z" z="12.2"/>
<ksterm_trapped name="term_trapped" max_turns="10"/>
```

List of Figures

Bibliography

[Aba94] K.N. Abazajian et.al. Resonantly Produced 7 keV Sterile Neutrino Dark Matter Models and the Properties of Milky Way Satellites. *Phys. Rev. Lett., vol. 112, p. 161303*, 1994.

[Aba12] K.N. Abazajian et.al. Light Sterile Neutrinos: A White Paper. *arXiv:1204.5379*, 2012.

[Aku02] Yu.A. Akulov, B.A. Mamyrin. Determination of the Ratio of the Axial-Vector to the Vector Coupling Constant for Weak Interaction in Triton Beta Decay. *Phys. of Atomic Nuclei, vol. 65, no. 10, pp. 1795-1797*, 2002.

[Alp48] R. Alpher, R. Herman. On the Relative Abundance of the Elements. *Phys. Rev., vol. 12, pp. 1737-1742*, 1948.

[Ase00] V. N. Aseev et al. Energy Loss of 18 keV Electrons in gaseous T and quench condensed D Films. *The Europ. Phys. Journal D 10, vol. 02/2000, pp. 39-52*, 2000.

[Bah01] J.N. Bahcall, M.H. Pinsonneault, S. Basu. Solar Models: current Epoch and Time Dependences, Neutrinos and helioseismological Properties. *Astrophys. Journal, vol. 550, pp. 990-1012*, 2001.

[Bah05] J.N. Bahcall, A.M. Serenelli, S. Basu. New Solar Opacities, Abundances, Helioseismology, and Neutrino Fluxes. *Astrophys. Journal, vol. 621, pp. 85-88*, 2005.

[Beh82] H. Behrens, W. Buehring. Electron radial Wavefunctions and Nuclear beta-Decay. *Clarendon, Oxford*, 1982.

[Bez11] F. Bezrukov. Warm Dark Matter in The Galaxies: Theoretical and observational Progresses. *Highlights and Conclusions of the Chalonge CIAS Meudon Workshop 2011, Chapter 1, pp. 7-9*, 2011.

[Bil60] S.M. Bilenkii et al. *Sov. Phys. JET, vol. 37, p. 1241*, 1960.

[Bon01] J. Bonn et al. The Mainz Neutrino Mass Experiment. *Nucl. Phys. B Proc. Suppl., vol. 91, no. 1-3, pp. 273-279*, 2001.

[Boy12] A. Boyarsky, D. Iakubovskyi, O. Ruchayski. Next Decade of Sterile Neutrino Studies. *Phys. of the Dark Univ., vol. 1, no. 1, pp. 136-154*, 2012.

[Boy14] A. Boyarsky, O. Ruchayskiy, D. Iakubovskyi, J. Frans. An unidentified Line in X-Ray Spectra of the Andromeda Galaxy and Perseus Galaxy Cluster. *Phys.Rev.Lett., vol. 113, pp. 251-301*, 2014.

[Bul14] E. Bulbul et al. Detection of an Unidentified Emission Line in the Stacked X-Ray Spectrum of Galaxy Clusters. *The Astrophys. Journal, vol. 789, pp. 13-23*, 2014.

[Cha14] J. Chadwick. Intensitätsverteilung im magnetischen Spektrum der Betastrahlen von Radium B+C. *Verhandlungen der deutschen physikalsichen Gesellschaft, vol. 16, p. 383*, 1914.

[Cha32] J. Chadwick. Possible Existence of a Neutron. *Nature, vol. 129, p. 312*, 1932.

[Cle69] P. Clemmow, J. Dougherty. Eletrodynamics of Particles and Plasmas. *Addison-Wesley Publicshing Company*, 1969.

[Cle98] B. Cleveland et al. *The Astrophys. Journal, vol. 496, pp. 505-526*, 1998.

[Cow56a] C.L. Cowan, F. Reines. *Nature, vol. 178, pp. 446-523*, 1956.

[Cow56b] C.L. Cowan, F. Reines, F.B. Harrison, H.W. Kruse, A.D. McGuire. Detection of the free Neutrino: a Confirmation. *Science, vol. 124, no. 3212, pp. 103-104*, 1956.

[Dan62] G. Danby et al. Observation of high-Energy Neutrino Reactions and the Existence of two Kinds of Neutrinos. *Phys. Rev. Lett., vol. 9, no. 1, pp. 36-44*, 1962.

[Dav94] R. Davis. A Review of the Homestake Solar Neutrino Experiment. *Prog. Part. Nucl. Phys., vol. 32, pp. 13-32*, 1994.

[Dre12] G. Drexlin. Lectures on Astroparticlephysics. *KIT*, 2012.

[Ede11] Edelweiss Collaboration. Final Results of the EDELWEISS-II WIMP Search using a 4-kg Array of Cryogenic Germanium Detectors with interleaved Electrodes. *Phys. Rev. Lett. B, vol. 702, pp. 329-335*, 2011.

[Elt58] L.R.B. Elton. A semi-empirical Formula for the Nuclear Radius. *Nucl. Phys., vol. 5, pp. 173-178*, 1958.

[Erh12] M. Erhard. Untersuchung der Langzeitstabilität des nuklearen Standards für die Energieskala des KATRIN-Experiments. *Master's Thesis KIT*, 2012.

[Fer34] E. Fermi. Versuch einer Theorie der beta-Strahlen. *Zeitschrift für Physik A, vol. 88, p. 161*, 1934.

[Fle34] A. Fleming. On the History and Development of the thermionic Valve. *Journal of Scientific Instruments, vol. 11, no. 2, pp. 44-49*, 1934.

[GAL99] GALLEX Collaboration. GALLEX Solar Neutrino Observations: Results for GALLEX IV. *Phys. Rev. Lett. B, vol. 447, no. 1-2, pp. 127-133*, 1999.

[GER06] GERDA Collaboration. Status of the GERmanium Detector Array (GERDA) for the Search of neutrinoless Double beta-Decay of 76Ge at LNGS. *Prog. Part. Nucl. Phys., vol. 57, no. 1, pp. 241-250*, 2006.

[GER13] GERDA Collaboration. Results on Neutrinoless Double beta-Decay of 76Ge from GERDA Phase I. *Phys. Rev. Lett., vol. 111, p. 122503*, 2013.

[Gil10] W. Gil et al. The Cryogenic Pumping Section of the KATRIN Experiment. *Applied Superconductivity, vol. 20, no. 23, pp. 316-319*, 2010.

[Gla61] S.L. Glashow. Partial Symmetries of weak Interactions. *Phys. Rev. Lett., vol. 22, pp. 579-588*, 1961.

[Gla93] E. Glasner, B. Weiss. Sensitive Dependence on initial Conditions. *Nonlinearity, vol. 6, pp. 1067-1075*, 1993.

[Glü11] F. Glück. Axisymmetric Magnetic Field Calculation with Zonal Harmonic Expansion. *Progress In Electromagnetics Research B, vol. 32, pp. 351-388*, 2011.

[Glü15] F. Glück. Privat Communication. 2015.

[Gro15] S. Groh. *Modeling of the Response Function and Measurement of Transmission Properties of the KATRIN Experiment.* PhD thesis, Karlsruher Institiute of Technoloy, IEKP, 2015.

[Har12] F. Harms. Assembly and first Results of the KATRIN Focal-Plane Detector System at KIT. *Master's thesis, KIT*, 2012.

[Hax85] W. Haxton. Atomic Effects and Heavy-Neutrino Emission in Beta Decay. *Phys. Rev. Lett.,vol. 55, pp. 807-807*, 1985.

[Höt12] M. Hötzel. *Simulation and Analysis of source-related Effects for KATRIN.* PhD thesis, KIT, 2012.

[Hug10] K. Hugenberg. An angular resolved pulsed UV LED Photoelectron Source for KATRIN. *Progress in Particle and Nuclear Physics, vol. 64, no. 2, pp. 288-290*, 2010.

[Jan15] A. Jansen. *The Cryogenic Pumping Section of the KATRIN Experiment - Design Studies and Experiments for the Commissioning.* PhD thesis, KIT, 2015.

[Käf12] W. Käfer. Monitoring of the operating Parameters of the KATRIN Windowless Gaseous Tritium Source. *New J. Phys., vol. 14, p. 26*, 2012.

[Kam96] Kamiokande Collaboration. Solar Neutrino Data Covering Solar Cycle 22. *Phys. Rev. Lett., vol. 77, pp. 1683-1686*, 1996.

[Kam03] KamLAND Collaboration. First Results from KamLAND: Evidence for Reactor Antineutrino Disappearance. *Phys. Rev. Lett., vol. 90, p. 021802*, 2003.

[KAT05] KATRIN Collaboration. KATRIN Design Report 2004. *FZKA Scientific Report 7090*, 2005.

[Kit04] C Kittel. Introduction to Solid State Physics, 8th Edition. *Wiley*, 2004.

[Kly99] A. Klypin, A.V. Kravtsov, O. Valenzuela, F. Prada. Where Are the Missing Galactic Satellites? *Astrophys. Journal, vol. 522, p. 82*, 1999.

[Kod01] K. Kodama et al. Observation of Tau Neutrino Interactions. *Phys. Rev. Lett. B, vol. 504, no. 3, pp. 218-224*, 2001.

[Kos12] A. Kosmider. *Tritium Retention Techniques in the KATRIN Transport Section and Commissioning of its DPS2-F Cryostat.* PhD thesis, KIT, 2012.

[Leh64] B. Lehnert. Dynamics of charged Particles. *North Holland Published*, 1964.

[Les12] J. Lesgourgues, S. Pastor. Neutrino Mass from Cosmology. *Adv. in High Energy Phys., vol. 2012, no. 608515*, 2012.

[Lob99] V.M. Lobashev et al. Direct search for Mass of Neutrino and Anomaly in the Tritium beta-Spectrum. *Phys. Rev. Lett. B, vol. 460, no. 1-2, pp. 227-235*, 1999.

[Luk12] S. Lukic et al. Measurement of the Gasflow Reduction Factor of the KATRIN DPS2-F Differential Pumping Section. *Vacuum, vol. 86, no. 8, pp. 1126 -1133*, 2012.

[MAJ14] MAJORANA Collaboration. The Majorana Demonstrator neutrinoless Double beta-Decay Experiment. *Adv. in High Energy Phys., vol. 2014, pp. 1-18*, 2014.

[Mer12] S. Mertens. *Study of Background Processes in the Electrostatic Spectrometers of the KATRIN Experiment.* PhD thesis, KIT, 2012.

[Mer14] S. Mertens, T. Lassere, S. Groh, A. Huber, G. Drexlin, C. Weinheimer. Sensitivity of Next-Generation Tritium Beta-Decay Experiments for keV-Scale Sterile Neutrinos. *Journal of Cosmo. and Astropart. Phys., vol. 1502, p. 020*, 2014.

[Mer15] S. Mertens. TRISTAN: Tritium Beta Decay to Search for Sterile Neutrinos. *Presentation*, 2015.

[Mil94] M. Milgrom. Dynamics with a non-standard Inertia-Acceleration Relation: an Alternative to Dark Matter. *Ann.Phys., vol. 229, pp. 384-415*, 1994.

[Nor63] T.G. Northrop. The Adiabtic Motion of Charged Particles. *Intersience Published*, 1963.

[Oli14] K.A. Olive et al. (Particle Data Group). The Review of Particle Physics. *Chinese Physics C*, 2014.

[Pau30] W. Pauli. Sehr geehrte radioaktive Damen und Herren. *published in R.Kronig and V. Weisskopf (Eds.)*, 1930.

[Pen65] A.A. Penzias, R.W. Wilson. A Measurement of Excess Antenna Temperature at 4080 Mc/s. *Astrophys. Journal, vol. 142, no. 1, pp. 419-421*, 1965.

[Per75] M.L. Perl et al. Evidence for Anomalous Lepton Production in e+-e- Annihilation. *Phys. Rev. Lett., vol. 35, no. 22, pp. 1489-1492*, 1975.

[Per03] D. Perkins. *Particle Astrophysics.* Oxford University Press, 2003.

[Pet13] S. T. Petcov. The Nature of Massive Neutrinos. *Adv. High Energy Phys., vol. 2013, id.852987*, 2013.

[Phy14] Kimball Physics. The EGF-3104. *Manual*, 2014.

[Pla14] Planck Collaboration. Planck 2013 Results. XVI. Cosmological Parameters. *Astronomy and Astrophys., vol. 571, p. 66*, 2014.

[Pon58] B. Pontecorvo. Inverse beta-Processes and Nonconservation of Lepton Charge. *Sov.Phys.JETP, vol. 7, pp. 172-173*, 1958.

[Pra12] M. Prall et al. The KATRIN pre-Spectrometer at reduced Filter Energy. *New Journal of Phys., vol. 14, no. 7, p. 073054*, 2012.

[Ren11] P. Renschler. *KESS - A new Monte Carlo Simulation Code for low-Energy Electron Interactions in Silicon Detectors.* PhD thesis, KIT, 2011.

[Rep83] W.W. Repko, C. Wu. Radiative Corrections to the Endpoint of the Tritium beta-Decay Spectrum. *Phys. Rev. C, vol. 28, no. 6, pp. 2433-2436*, 1983.

[Ric05] O.W. Richardson. On the negative Radiation from hot Platinum. *Philosophical of the Cambridge Philosophical Society, vol. 11, pp. 286-295*, 1905.

[Röl11] M. Röllig. Studien zu einem Röntgendetektorsystem zur Überwachung der KATRIN Tritiumquelle. *Master's Thesis KIT*, 2011.

[SAG02] SAGE Collaboration. Solar Neutrino Flux Measurements by the Sovjet-American Gallium Experiment (SAGE) for half the 22-Year Solar Cycle. *Exp. Theo. Phys., vol. 95, pp. 181-193*, 2002.

[Sal68] A. Salam. *Elementary Particle Theory.* Teubner Studienbücher(Stockholm), 1968.

[San11] N. G. Sanchez, H. J. de Vega. Warm Dark Matter in the Galaxies: theoretical and observational Progresses. Highlights and Conclusions of the Chalonge Meudon Workshop 2011. *arXiv:1109.3187*, 2011.

[Sch80] J. Schlechter, J.W.F. Valle. Neutrino Masses in SU(2) x U(1) Theories. *Phys. Rev. D, vol. 22, no. 9*, 1980.

[SNO02] SNO Collaboration. Direct Evidence for Neutrino Flavor Transformation from Neutral-Current Interactions in the Sudbury Neutrino Observatory. *Phys. Rev. Lett., vol. 89, no. 011301*, 2002.

[Ste13] N. Steinbrink et al. Neutrino Mass Sensitivity by MAC-E-Filter based time-of-flight Spectroscopy with the Example of KATRIN. *New J. Phys., vol. 15, p. 113020*, 2013.

[Tay98] A. Taylor et al. Gravitational Lens Magnification and the Mass of Abell 1689. *The Astrophys. Journal*, 1998.

[Ull08] T. Ullrich, Z. Xu. Treatment of Errors in efficiency Calculations. *Report at the Brookhaven National Laboratory*, 2008.

[Wan13] N. Wandkowksy. *Study of Background and Transmission Properties of the KATRIN Spectrometers.* PhD thesis, KIT, 2013.

[Wei67] S. Weinberg. A Model of Leptons. *Phys. Rev. Lett., vol. 19, pp. 1264-1266*, 1967.

[Wes74] J. Wess, B. Zumino. Supergauge Transformations in four Dimensions. *Nuclear Phys. B., vol. 70, pp. 39-50*, 1974.

[Wil82] D.H. Wilkinson. Analysis of Neutron beta-Decay. *Nucl. Phys. A, vol. 377, pp. 474-504*, 1982.

[Wil90] D.H. Wilkinson. Evaluation of beta-Decay: II. Finite Mass and Size Effects. *Nucl. Instr. Meth. A, vol. 290, pp. 509-515*, 1990.

[Zub12] K. Zuber. *Neutrino Physics.* CRC Press, 2012.

[Zwi33] F. Zwicky. Die Rotverschiebung von extragalaktischen Nebeln. *Helvetica Acta-Physica Acta, vol. 6, pp. 110-127*, 1933.

Danksagung

Die Ergebnisse dieser Arbeit sind im direkten und indirekten Zusammenspiel mit sehr vielen Menschen entstanden. Deshalb möchte ich die Gelegenheit nutzen, um ihnen von ganzem Herzen und aufrichtig zu danken.

Der erste Dank gebührt Prof. Guido Drexlin und Susanne Mertens. Ohne ihre ständige Förderung und Forderung wäre nicht nur diese Arbeit, sondern auch der Weg dorthin, niemals so erfolgreich verlaufen. Guido Drexlin hat es geschafft mich durch seine ansteckende, leidenschaftliche und unterhaltsame Art für die Astroteilchenphysik zu begeistern. Sein Engagement und seine Förderung, haben mir sehr viele Türen geöffnet. Susanne Mertens danke ich für die vielen Dinge die ich von Ihr gelernt habe, die vielen Fragen die sie gestellt hat und den freundschaftlich vertrauensvollen Umgang.

Weiterhin bedanken möchte ich mich

- bei Prof. Ulrich Husemann der unkompliziert und sehr spontan das Korreferat für diese Arbeit übernommen hat.
- bei Stefan Groh für die spannend, lehrreiche und amüsante Zeit am LBNL in Berkeley und die gemeinsame Zeit am KIT.
- bei Florian Fränkle, Martin Babutza und Alexander Jansen für die Unterstützung im E-Gun Labor und bei den Messungen
- bei allen Technikern im Bau 601, allen voran Klaus Mehret und Bernhard Bender, die maßgeblich am Aufbau des Testexperiments und des Folgeexperiments beteiligt waren. Hervorheben möchte ich meinen Dank an Klaus Mehret, für die kleinen Handwerkslehrstunden, die politisch anspruchsvollen Diskussionen und seine aufrichtige Freundschaft.
- bei meinen Zimmerkollegen Hendrik Seitz-Moskaliuk, Moritz Machatschek sowie Johannes Antoni, stellvertretende für die gesammte KATRIN Gruppe, für das tolle Arbeitsklima am Institut.
- bei meinen Freunden Moritz Hackenjos, Jan Bondy, Isabell Arnst, Florian Heizmann, Annabel Schomburg, Léonard Gaucher, Frédérik Husser und Panagiotis Kotetes für die großartige Zeit im Studium und den Freundschaften die daraus hervorgegangen sind.
- beim Physiker Theater und meinen musikalischen Mentoren Mindaugas Piecaitis und Olga Zheltikova für den kulturellen Ausgleich und die vergnüglichen Stunden abseits des Studiums
- bei meinen Mitarbeiterinnen und Mitarbeiter der Ortsverwaltung Wolfartsweier, die mir gerade in den letzten Wochen mit viel Geschick und Eigenleistung den Rücken

frei gehalten haben. Dank gebührt auch meinem Stellvertreter Joachim Supper für die Vertretung in den letzten Wochen meiner Arbeit.

- bei der Friedrich-Ebert-Stiftung, für die finanzielle und vor allem ideelle Förderung während des Studiums und den vielen tollen Menschen die ich während meiner Zeit als Stipendiat kennen gelernt habe.

Gesondert bedanken möchte ich mich bei all meinen Freunden, allen voran den Jungs der PUI-Tour, allen Auslandskorrespondenten, Hauke Löffler und meinem Freund und Mitbewohner Paul Schumacher, für die jahrelange Wegbegleitung und den unendlichen Spaß den wir alle schon miteinander hatten.

Bei meiner Freundin Christin Scheurer möchte ich mich ebenfalls separat bedanken. Du hast wie wohl keine zweite unter den Strapazen der letzten Monaten gelitten. Ich bin froh dass es dich gibt, und das du meine Launen irgendwie ertragen hast. Ich hoffe ich kann dir irgendwann zurückgeben, was du mir gegeben hast.

Mein größter Dank jedoch gebührt meinen Eltern Matthias und Caterina Huber, meinen Geschwistern Hannes, Lisa und Lukas sowie meiner Großmutter Margarete Huber. Ihr habt mich mein ganzes Leben lang unterstützt, seid mit mir jeden Umweg gegangen und habt immer an mich geglaubt. Meine Dankbarkeit dafür lässt sich nicht in Worte fassen.

Um, wie beobachtet, einen mittleren Dopplereffekt von 1000 km/sek oder mehr zu erhalten, müsste also die mittlere Dichte im Comasystem mindestens 400 mal grösser sein als die auf Grund von Beobachtungen an leuchtender Materie abgeleitete[1]). Falls sich dies bewahrheiten sollte, würde sich also das überraschende Resultat ergeben, dass dunkle Materie in sehr viel grösserer Dichte vorhanden ist als leuchtende Materie.

-Fritz Zwicky (1898 - 1974)